PUMP-PROBE STUDY OF ATOMS AND SMALL MOLECULES WITH LASER DRIVEN HIGH ORDER HARMONICS

by

WEI CAO

B.S., Huazhong University of Science and Technology, China, 2004

AN ABSTRACT OF A DISSERTATION

submitted in partial fulfillment of the
requirements for the degree

DOCTOR OF PHILOSOPHY

Department of Physics
College of Arts and Sciences

KANSAS STATE UNIVERSITY
Manhattan, Kansas

2014

Abstract

A commercially available modern laser can emit over 10^{15} photons within a time window of a few tens of femtoseconds (10^{-15} second), which can be focused into a spot size of about 10 μm, resulting in a peak intensity above 10^{14} W/cm^2. This paves the way for table-top strong field physics studies such as above threshold ionization (ATI), non-sequential double ionization (NSDI), high order harmonic generation (HHG), *etc.*. Among these strong laser-matter interactions, high order harmonic generation, which combines many photons of the fundamental laser field into a single photon, offers a unique way to generate light sources in the vacuum ultraviolet (VUV) or extreme ultraviolet (EUV) region. High order harmonic photons are emitted within a short time window from a few tens of femtoseconds down to a few hundreds of attoseconds (10^{-18} second). This highly coherent nature of HHG allows it to be synchronized with an infrared (IR) laser pulse, and the pump-probe technique can be adopted to study ultrafast dynamic processes in a quantum system. The major work of this thesis is to develop a table-top VUV(EUV) light source based on HHG, and use it to study dynamic processes in atoms and small molecules with the VUV(EUV)-pump IR-probe method. A Cold Target Recoil Ion Momentum Spectroscopy (COLTRIMS) apparatus is used for momentum imaging of the interaction products. Two types of high harmonic pump pulses are generated and applied for pump-probe studies. The first one consists of several harmonics forming a short attosecond pulse train (APT) in the EUV regime (around 40 eV). We demonstrate that, (1) the auto-ionization process triggered by the EUV in cation carbon-monoxide and oxygen molecules can be modified by scanning the EUV-IR delay, (2) the phase information of quantum trajectories in bifurcated high

harmonics can be extracted by performing an EUV-IR cross-correlation experiment, thus disclosing the macroscopic quantum control in HHG. The second type of high harmonic source implemented in this work is a single harmonic in the VUV regime (around 15 eV) filtered out from a monochromator. Experiments on D_2 molecules have been conducted using the 9th or the 11th harmonic as the pump pulse. Novel dissociative ionization pathways via highly excited states of D_2 have been revealed, thus suggesting potential applications for time-resolved studies and control of photochemistry processes.

PUMP-PROBE STUDY OF ATOMS AND SMALL MOLECULES WITH LASER DRIVEN HIGH ORDER HARMONICS

by

WEI CAO

B.S., Huazhong University of Science and Technology, China, 2004

A DISSERTATION

submitted in partial fulfillment of the
requirements for the degree

DOCTOR OF PHILOSOPHY

Department of Physics
College of Arts and Sciences

KANSAS STATE UNIVERSITY
Manhattan, Kansas

2014

Approved by:

Major Professor
Itzik Ben-Itzhak

Co-Major Professor
Charles Lewis Cocke

Copyright

Abstract

A commercially available modern laser can emit over 10^{15} photons within a time window of a few tens of femtoseconds (10^{-15} second), which can be focused into a spot size of about 10 μm, resulting in a peak intensity above 10^{14} W/cm^2. This paves the way for table-top strong field physics studies such as above threshold ionization (ATI), non-sequential double ionization (NSDI), high order harmonic generation (HHG), *etc.*. Among these strong laser-matter interactions, high order harmonic generation, which combines many photons of the fundamental laser field into a single photon, offers a unique way to generate light sources in the vacuum ultraviolet (VUV) or extreme ultraviolet (EUV) region. High order harmonic photons are emitted within a short time window from a few tens of femtoseconds down to a few hundreds of attoseconds (10^{-18} second). This highly coherent nature of HHG allows it to be synchronized with an infrared (IR) laser pulse, and the pump-probe technique can be adopted to study ultrafast dynamic processes in a quantum system. The major work of this thesis is to develop a table-top VUV(EUV) light source based on HHG, and use it to study dynamic processes in atoms and small molecules with the VUV(EUV)-pump IR-probe method. A Cold Target Recoil Ion Momentum Spectroscopy (COLTRIMS) apparatus is used for momentum imaging of the interaction products. Two types of high harmonic pump pulses are generated and applied for pump-probe studies. The first one consists of several harmonics forming a short attosecond pulse train (APT) in the EUV regime (around 40 eV). We demonstrate that, (1) the auto-ionization process triggered by the EUV in cation carbon-monoxide and oxygen molecules can be modified by scanning the EUV-IR delay, (2) the phase information of quantum trajectories in bifurcated high

harmonics can be extracted by performing an EUV-IR cross-correlation experiment, thus disclosing the macroscopic quantum control in HHG. The second type of high harmonic source implemented in this work is a single harmonic in the VUV regime (around 15 eV) filtered out from a monochromator. Experiments on D_2 molecules have been conducted using the 9th or the 11th harmonic as the pump pulse. Novel dissociative ionization pathways via highly excited states of D_2 have been revealed, thus suggesting potential applications for time-resolved studies and control of photochemistry processes.

Table of Contents

List of Figures

List of Tables

Acknowledgments

I would like to thank Dr. C. Lewis Cocke, my co-advisor and mentor, for giving me the opportunity to work in his group from the beginning of my graduate study. His broad knowledge and deep insight in physics has inspired me constantly to build up the correct perspective on physics problems. He has taught and encouraged me patiently to become a real physicist, which is invaluable for my future career.

I would like to thank Dr. Itzik Ben-Itzhak, my major advisor, for his guidance and support on my Ph. D. thesis. His encouragement and advices are the major driving forces on my second thesis project—pump-probe experiment with single order harmonics as the pump. He has guided me through the difficulties in the experiment and taught me to become an independent experimentalist.

I would like to thank my thesis committee members, Dr. Brett Esry, Dr. Viktor Chikan, and outside chairperson, Dr. John R. Schlup for helpful discussions and corrections on this dissertation.

I would like to thank the former group members, Dr. Guillaume Laurent and Dr. Sankar De, whom I spent the most time to work with in the laboratory. They are always helpful as both colleagues and friends. I also would like to thank our visitors Dr. Ali Alnaser and Dr. Markus Schöffler. Their excellent expertise has helped improve the performance of our experimental set-up.

I would like to thank Dr. Jin Cheng for supporting theoretical simulations on high harmonic generation. I would like to thank Youliang Yu and Shuo Zeng for valuable discussions on simulations of diatomic molecule dynamics.

I would like to thank the J. R. Macdonald Laboratory staffs, Al Rankin, Mike Wells, Scott Chainey, Bob Krause, Vince Needham for their assistance of designing, modifying and testing the experimental set-up. Special thanks to Dr. Kevin Carnes for providing assistance on the data acquisition system of my set-up and proofreading my dissertation.

I would like to thank the former KLS group members, Dr. Hiroki Mashiko, Dr. He Wang, Dr. Shouyuan Chen, Dr. Baozhen Zhao, Dr. Sabih D. Khan, Dr. Michael Chini, and Dr. Kun Zhao, who have been extremely helpful for maintaining and providing the reliable laser source for the experiments. I have also learned the basic knowledge of laser technology from them.

I would like to thank Dr. Artem Rudenko, Dr. Carlos Trallero, and Dr. Matthias Kling for valuable discussions on my experiment.

I would like to acknowledge the financial support of Chemical Sciences, Geosciences, and Biosciences Division, Office of Basic Energy Sciences, Office of Science, U.S. Department of Energy, National Science Foundation and the U.S. Army Research Office.

Finally, my thanks go to my families and especially my wife, Shun Wu. This work could never be accomplished without her continuous love and support.

Chapter 1

Introduction

1.1 Overview

Electronics is probably the most important technology that we encounter on a daily basis, through the use of personal computers, television, radio, digital cameras, cellphones, *etc.*. Electronics is also widely used in information processing and telecommunications. The key components inside almost all these instruments are the semiconductor devices used to control the electron flow itself or its interaction with electromagnetic radiation inside an integrated circuit. The speed of an electronic device is limited by how fast the electron current switch can be. So far, the silicon based electronics has reached a speed limit of picoseconds, where the microwave is the standard source. In order to push the speed limit further down, i.e. to the optical regime, radiation with higher frequency will be needed as a controlling source. This will not only provide higher speeds of operation but also smaller size and weight of the equipment. Laser technology brings us a new radiation source that is extremely short in time. 40 years after the invention of the laser, people have already pushed the laser pulse duration down to its fundamental limit: a pulse containing only one optical cycle (2.67 fs at 800 nm) [1–3]. It was only a decade ago that the femtosecond barrier was overcome and the attosecond light pulse was generated using a table-top setup [4, 5].

The rapid progress of ultrafast light source development has the potential for controlling electron currents with unprecedented speeds, therefore setting up a possible new speed limit of future electronics, dubbed as lightwave electronics by Goulielmakis and coworkers [3, 6]. So, the study of the interaction between electrons and ultrafast electromagnetic radiation is not only an important branch of atomic, molecular and optical (AMO) physics but can also have a great impact on the industries that surround us.

1.2 Structure and dynamics

Structure is one of the most important aspects of matter that we want to determine. It includes the constituents that make up a certain object and how they remain firmly bound together. From a microscopic perspective, we know that everything is made of atoms, which have sizes on the scale of an angstrom (10^{-10} m). Each atom is made of negatively charged electrons and a positively charged nucleus, discovered by J. J. Thomson and Ernest Rutherford, respectively. If the electrons are shared by multiple nuclei, molecules are formed. If many nuclei are arranged in a periodic fashion a crystal is created. Each atom or molecule has a characteristic energy structure according to quantum theory.

By solving the time-independent Schrödinger equation, the allowed eigenstates of the quantum system can be obtained, which discloses the energy structure information in the quantum system. Experimentally, spectroscopic techniques have been applied to uncover the characteristic energy structure of materials [7, 8]. In this technique the electromagnetic source irradiates the material of interest and characteristic lines show up in the transmission or absorption spectrum, e.g. the Lyman series and Balmer series of hydrogen, and thus the basic elements can be determined. In order to know how the atoms are arranged spatially, electron or x-ray diffraction techniques can be applied to reveal the sub-angstrom pattern [9–13]. Both the spectroscopy and diffraction techniques generally focus on the stationary structure information of matter.

In some circumstances like chemical reactions, light induced excitation, ionization *etc.*, the system is put in a transition state that is unstable and can evolve over time. These processes bring us to another essential aspect of matter, the dynamics. Based on the Heisenberg uncertainty principle, the lifetime of a certain process is closely related to the energy uncertainty of the system. This connects the structure and the dynamics of a system together. Assuming that the electron is sitting on multiple energy eigenstates at the same time, due to the interference of different states we would expect some beat signal to show up in the density distribution of the electron cloud. Take the hydrogen atom as an example. If both the $1s$ and $2p$ states with the eigen-energies of E_{1s} and E_{2p} are populated coherently and the atom evolves under field-free conditions, we would expect an oscillatory motion in the electron density distribution with a period of $T = 1/(E_{2p} - E_{1s})$. From this expression we conclude that the period of dynamic motion is inversely proportional to the energy gap between the two states. If we define T as the characteristic time, we can get the time scales of different dynamic processes. In molecules, the typical vibrational spacing is on the order of tens to hundreds of millielectron volts, which implies that the vibrational motion of the nuclei has a time scale of a few tens of femtoseconds. For bound electrons in atoms, molecules, or even bigger complex systems, the energy spacing of electronic states can be a few electron volts. This indicates that excitation or ejection of the electron occurs on a time scale as short as a few tens of attoseconds ($1\ as = 10^{-18}\ second$). Figure 1.1 sketches out the typical evolution times of different processes.

1.3 Two pump-probe schemes

Observing the ultrafast motion inside molecules and atoms in real time has been a fascinating and challenging task. A significant breakthrough was made by Ahmed H. Zewail, who won the 1999 chemistry Nobel prize for developing rapid laser technique that enables scientists to study the action of atoms in chemical reactions, leading to the creation of fem-

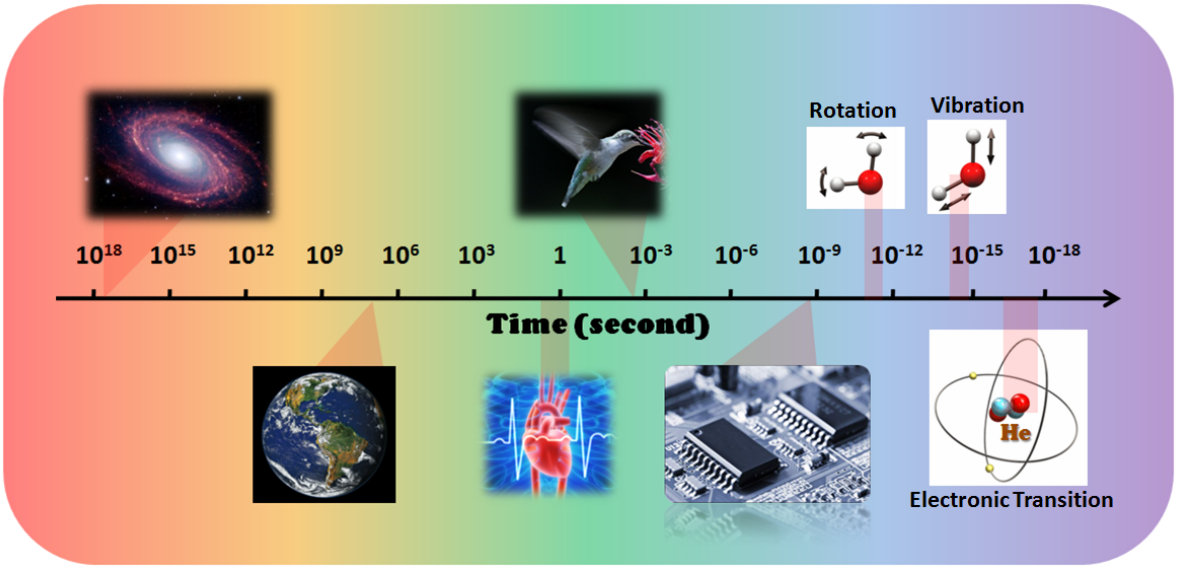

Figure 1.1: Typical timescale of different processes

tochemistry [14,15]. This technique, or the so called pump-probe technique, is the analog of conventional snapshot photography. An ultrafast femtosecond laser pulse is splitted into two beams. Since a chemical reaction can last from a few tens to a few hundreds of femtosecond, one beam, called the "pump", is used to create the reaction nearly instantaneously, then the second beam, called the "probe", provides the shutter speed to "snapshot" the ongoing action at a particular delay time so that the whole process can be observed in "slow motion". How fast the process to be observed can be depends on how short the pump and probes pulses are, i.e. how fast the "shutter" speed is.

Although femtochemistry allows us to gain insight into the dynamics of atoms in molecular systems, femtosecond lasers have fundamental limits on pulse duration that prevents us from getting access to dynamics information on the time scale of the electrons inside atoms. A light source as short as a few hundreds of attoseconds is needed to follow the evolution of electrons inside atoms and molecules, which indicates that the wavelength of the source needs to be extended to the extreme ultraviolet regime. In 2001, P. M. Paul and colleagues produced a train of 250-as light pulses [5]. Later in the same year, M. Hentschel and his colleagues made the first measurement of a single attosecond light burst [4]. In both

experiments, the sub-femtosecond light source was generated via high order harmonic generation (HHG), which indicates that HHG can be a promising tool for time-resolved studies in the attosecond regime. Following these experiments, time-resolved measurement of atomic electrons progressed rapidly and signaled the creation of attophysics as a discipline [6,16,17].

High order harmonic generation is a highly nonlinear non-perturbative phenomenon, in which a high intensity laser is frequency up-converted to the extreme ultraviolet (EUV) regime by interacting with atoms or molecules [18–21]. The whole process is highly coherent in time and occurs repeatedly within a small fraction of each half laser cycle. Depending on the temporal duration and detailed structure of the carrier wave of the driving laser field, an isolated attosecond pulse or attosecond pulse trains with constant period will be generated [22, 23]. Either one would provide an excellent ultrafast timing tool that can possibly "freeze" the fast dynamic process. In general, the pump-probe technique needs a fast trigger to prepare the evolving system at a well-defined initial time. After the pump pulse (either infrared(IR) or HHG), the coherent wave-packet will evolve until a probe arrives to break up or ionize the system so that the time-resolved information can be decoded. In order to reach the desired time resolution, both pump and probe have to be shorter than this time scale. In this way, we describe the pump-probe technique as a sequential process in which pump and probe pulses can be well separated in time and interact with the target independently. Many time-resolved studies have been done by groups worldwide using this sequential scheme [24–31].

In order to reach sub-femtosecond resolution, attosecond sources in both pump and probe beams are prerequisites for this scheme. However the HHG attosecond source has a low flux due to the very low conversion efficiency of radiation from the long wavelength driving field to the short wavelength harmonic field (on the order of 10^{-6}). Therefore, the rate of useful events that are generated by both the attosecond pump and the attosecond probe pulses in a sequential manner will be too low to be detected. An alternate way to overcome the resolution limit set by the pulse duration of the pump and probe is to use

the carrier instead of the envelope of the electromagnetic field to interact with the system of interest, examples being attosecond streaking [32–34] and RABBITT (reconstruction of attosecond beating by interference of two-photon transitions) experiments [5, 35]. In the RABBITT technique, the attosecond pulse train with a period of half an optical cycle of the driving field is synchronized precisely to a replica of the driving field. Each burst of the attosecond pulse train is thus phase locked to the carrier of the IR field. Each odd harmonic with enough photon energy will generate photoelectrons with energy equal to the HHG photon energy minus the binding energy via a single photon process. Photoelectrons with energy sitting between two consecutive odd harmonics will show up due to the EUV-IR two photon process, and their yield oscillates with the delay between the HHG and IR fields. In the attosecond streaking camera method, a single attosecond pulse instead of an attosecond pulse train is sychronized to the IR probe pulse. The attosecond pulse ionizes an electron with an initial momentum $\vec{P}_i$, and the canonical momentum $\vec{P}$ of the freed electron in the IR field is: $\vec{P} = \vec{P}_i + e\vec{A}$, where e is the electron charge and $\vec{A}$ is the vector potential of the IR field. Since $\vec{P}$ is conserved, the electron's final momentum $\vec{P}_f$ after the IR pulse ends will be shifted by the vector potential of the IR field at the time when the electron is born. Therefore $\vec{P}_f = \vec{P}_i + e\vec{A}(t_0)$ is dependent on the phase of the IR field, or time at which the electron is ionized. The phase dependent photoelectron pattern in both techniques (RABBITT and attosecond streaking) can be interpreted using the multi-path inteference picture [36], where the final energy of the photoelectron can be reached via different quantum paths, i.e. by absorbing a single harmonic photon, by absorbing a harmonic photon and a single or multiple IR photons, or by absorbing a relatively higher energy harmonic photon and emitting a single or multiple IR photons. The number of IR photons that are involved is related to the intensity of the IR field. The phase information of the multi-photon paths is encoded in the EUV-IR delay. When the different quantum paths are summed coherently, a delay-dependent oscillation in the yield of the photoelectron spectra emerges. The quantum paths involving two-photon or multiphoton processes are

selectively triggered when the IR and HHG field overlap with each other, and therefore the duration of the HHG pulse determines the resolution of the measurement. In these methods, both the pump and probe are participating in the interaction simultaneously, so it can be termed as a cross-correlation pump-probe technique. To date, the only scheme that has successfully decoded the attosecond information is the cross-correlation scheme in which the pump and probe overlap in time [2, 34, 37–40].

1.4 IR vs. high harmonic pulse as a pump

So far, the light-induced triggering in a pump-probe experiment has mainly been accomplished with two different pump sources: (1) femtosecond IR laser pulses and (2) high harmonic pulses. In the first case, a strong IR beam with electric field strength comparable to the coulomb interaction can excite or ionize the electron via a multiphoton or tunneling process. This is categorized as strong-field physics. In case of high harmonic light sources, the intensity is orders of magnitude lower than that of the IR laser pulses, since the harmonic photon energy is comparable to or greater than the electronic binding energy of a quantum system, the initial wave-packet can still be launched via a single photon process, which can be categorized as the perturbative regime with the harmonic pulse as the perturbation.

In the strong field case, i.e. with IR as the pump, the electron can access the sub-cycle information of the field. When the oscillating IR field reaches the peak of its carrier (zero phase of a cosine wave), a potential barrier will be formed due to the combination of the electric field and the Coulomb interaction (Fig. 1.2(b)). The electron can tunnel through the barrier within a small fraction of an optical cycle, which is on the order of a few hundred attoseconds for an 800 nm IR laser. The frequency of the IR field determines how frequently this tunneling event occurs. Due to the interference of these repeating processes in the time domain, structure will show up in the energy domain, such as in ATI spectra and HHG spectra. If the electric field is so strong that the bound electron cannot survive for more than

one period of the electric field, the electron cloud will be expelled out of the potential well instantly—a process called over barrier ionization (Fig. 1.2(c)). It will then result in a rather broad photoelectron distribution according to the time-energy uncertainty relationship. On

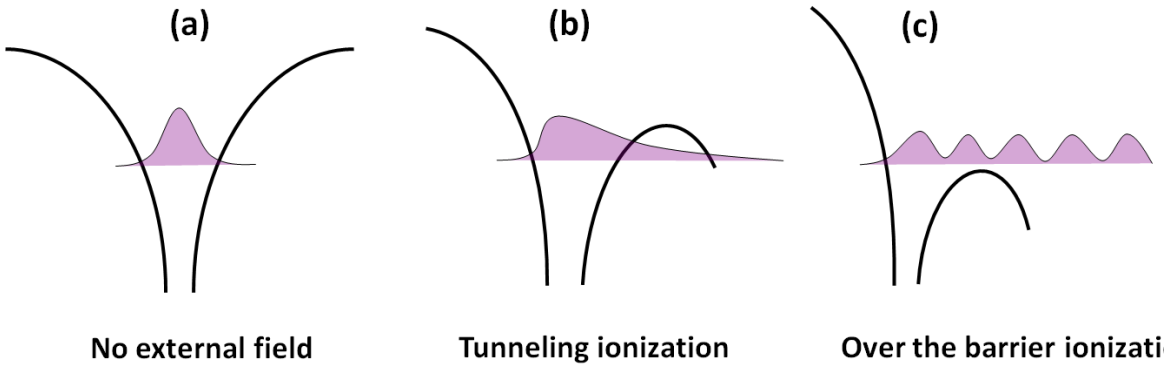

Figure 1.2: (a) the coulomb potential (black solid line) with no external field and the bound state wavefunction (purple area), (b) the coulomb potential is distorted by the external laser field, and electron can tunnel through the barrier, (c) the barrier formed by the coulomb potential and laser field is suppressed below the electron energy and the electron is now in the continuum.

the other hand, if a perturbative high harmonic light source is serving as a pump, the electron can excited or ionized via a single photon process. The whole time evolution of the light field is required to get the frequency distribution of the light (a Fourier transform of the signal in the time domain) so that the promoted electron energy distribution can be determined. If the frequency distribution of the harmonic light source is broad enough to support the formation of attosecond pulses, triggering still occurs on a subfemtosecond time scale. Therefore, both the IR and high harmonic pumps are efficient triggers that possess a time uncertainty from femtoseconds time scale to subfemtoseconds time scale. However, compared with the high harmonic induced triggering case, the theoretical treatment of the IR triggering, which involves many photons, will encounter more difficulties and usually requires far more approximations.

Another major difference between the weak high harmonic pulses and the strong IR laser pulse is that the short wavelength high harmonic pulse can produce single-photon electronic excitations in atoms and molecules, which single photons of IR cannot [41–49]. By absorbing

a single EUV harmonic photon an inner shell electron (instead of a valence electron) can be removed, leaving its ion counterpart excited. Accompanying this process are other quantum effects such as the shake-up of a valence electron [47], the Auger relaxation process [46] and even others that remain unknown. Thus the high harmonic light source provides an effective way for studying re-arrangement of the electron configuration in molecules, where the electron correlation becomes significant. The EUV-pump IR-probe technique has already been used to study electron rearrangement processes in a time-resolved manner. Specifically, the excited time-evolving system is prepared by an EUV pulse via a single photon process and later a strong IR pulse steers the system at different delays [47–49]. Although the IR probe has femtosecond pulse duration, the attosecond dynamic information is still accessible if the EUV attosecond pulses are synchronized to the carrier of the probe. The measurement and control of the re-arrangement process is expected to have an essential impact on chemical reaction control, and it will help us understand electron correlation from a physics point of view. Furthermore, the single photon absorption process in the first step mainly populates specific state(s) within a known bandwidth. This may rule out a mixture of multiple channels in the multi-photon case, thus providing cleaner and simpler results to compare with theoretical calculations.

1.5 Single harmonic as a pump

From a time-resolved point of view, HHG with broad spectrum is usually favored to achieve sub-femtosecond resolution with the loss of energy information as a trade off. However, VUV(EUV) light source with well-defined photon energy (i.e. narrow bandwidth) is preferred to perform spectroscopic studies. Thus a compromise between the temporal duration and frequency bandwidth of the pump source is generally optimized for different purposes of an experiment. Recently, efforts have been devoted to development of monochromatic light source based on HHG [50–53]. A single high harmonic from VUV or EUV regime can

be selected using different techniques (i.e. grating based monocrhomator [50,51], multilayer mirrors [52] or metallic filters [53]). Within the limitations of the uncertainty principle, this type of source preserves both temporal coherence (a few tens of femtoseconds) and narrow bandwidth (∼100 meV), allowing time-resolved studies or control of processes involving specific transition(s). The pioneering time-resolved experiment using fs single harmonic was performed by Sorensen and co-workers in 2000 [54]. The sixth harmonic radiation (9.4e eV) selected by a filter is used to prepare a wavepacket on certain Rydberg states of C_2H_2. These highly lying excited states can predissociate into C_2H^*+H. The time-resolve photoelectron measurement indicates that the predissociation has a lifetime of ∼150 fs. In 2001, Nugent-Glandorf and co-workers [50] used a grating-based monochromator to select the 17th harmonic (26.4 eV) for time-resolved study on Br_2 molecules. The fast dissociation process of the excited $C^1\Pi$ state is probed and determined to be about 40 fs with the time-resolved photoelectron measurement, although the temporal duration of the 17th harmonic is 250 fs. A rather similar experiment on Br_2 is performed in 2009 by Wernet *et al.* [55] using the 15th harmonic with a better temporal resolution (120 fs). More detailed information of the evolution of the valence electron during the bond breaking process is accessible. These studies provide dynamic information that is missing in the spectroscopic measurements with synchrotron radiation and CW lasers, thus offer complementary methodology for high precision spectroscopic experiment to help us get deeper insight of fundamental chemical processes.

1.6 Contents of this thesis

The major work of this thesis is to develop a table-top VUV (EUV) light source based on HHG and use it to study dynamic processes in atoms and small molecules with the VUV (EUV)-pump IR-probe method. A Cold Target Recoil Ion Momentum Spectroscopy (COLTRIMS) apparatus is used for momentum imaging of the interaction products. Chapter 2 reviews the generation mechanism of the coherent light source: high order harmonics.

Both the theoretical treatments and experimental conditions are mentioned in detail. Chapter 3 is devoted to the experimental setup with several high order harmonics as a pump. It includes a brief introduction to the laser system, and detailed descriptions of the Mach-Zehnder interferometer, the electron and ion detection system (COLTRIMS), and the data analysis methods we employed. Chapters 4 and 5 demonstrate the experimental studies of molecules and atoms using the setup introduced in Chapter 3. Chapter 4 covers the results and discussions related to light molecules. The modification of the auto-ionization process in carbon-monoxide and oxygen molecules is demonstrated via a sequential EUV-pump IR-probe scheme. Chapter 5 gives results and discussions related to noble-gas targets. The phase information of quantum trajectories in bifurcated HHG is extracted by performing an EUV-IR cross-correlation experiment demonstrating the macroscopic quantum control in HHG. Chapter 6 describes the experimental method for the pump-probe technique with a single high order harmonic as the pump. A single order harmonic in the VUV regime (72 $\sim$ 90 nm) is filtered out with a monochromator and synchronized with a delayed IR-probe pulse. Properties of the VUV source such as the pulse duration, bandwidth, spatial chirp, dispersion *etc.* are discussed. Chapter 7 demonstrates two experiments applying the setup introduced in chapter 6. The simplest molecular system D_2 is the target of interest. Both the 9th and the 11th harmonic are used as the pump to study the dissociative ionization process of D_2 molecules. Possible mechanisms are invoked to interpret the experimental observations. A summary of the thesis is covered in chapter 8.

Chapter 2

High Harmonic Generation

High order harmonic generation (HHG) is a strong field phenomenon. When atoms and molecules are exposed to laser pulses with intensity above 10^{13} W/cm^2, the frequency of the fundamental laser field is up-converted. Photons with energies of integer multiples of the fundamental photon energy will be emitted. The photon energy can extend to the VUV or even EUV regime, which may make it possible to produce a table-top soft x-ray source. Another great advantadge of HHG is its highly coherent nature in both the time and spatial domains [56–60], which leads to its second application as a tool for studying physics processes at extreme scales such as attosecond science and nano-science.

2.1 Theoretical description

The most well-known theory used to interpret the HHG process is the three-step model [61, 62]. From a semi-classical point of view, when an intense laser field interacts with an atom, the light-dressed coulomb potential will form a barrier on one side and bound electrons can tunnel through this barrier rapidly. The freed electron will then move classically in the presence of the electric field and accumulate kinetic energy. As the last step, electrons will follow the classical trajectory and recollide with the parent ion. Upon re-collision, the

"continuum" electron can couple back to the bound state with a certain probability and emit photons to conserve energy (the inverse process of photoionization). Assuming that the electron is "born" at a specific time t_i and undergoes acceleration by the monochromatic electric field, $E(t) = E_0 \cos \omega t$, with E_0 and ω representing the amplitude and angular frequency, respectively, its motion $x(t)$ will obey Newton's law of motion:

$$eE(t) = m_e \frac{d^2x(t)}{dt^2}, \tag{2.1}$$

where e and m_e represent the electron charge and mass, respectively. With the initial conditions $x(t_i) = 0$, $\dot{x}(t_i) = 0$, the equation can be solved analytically:

$$x(t) = \frac{eE_0}{m_e\omega}[\sin \omega t_i \times (t_i - t) - \frac{1}{\omega}(\cos \omega t - \cos \omega t_i)], \tag{2.2}$$

$$\dot{x}(t) = \frac{eE_0}{m_e\omega}(\sin \omega t - \sin \omega t_i), \tag{2.3}$$

Now we can define the re-collision, i.e. high harmonic generation, that occurs at a later time t_r when $x(t_r) = 0$, and the kinetic energy of the electron upon re-collision, $E_{kin} = \frac{1}{2} m_e \dot{x}(t_r)^2$, is converted to the HHG photon energy under the relationship $\hbar\omega_{HHG} = E_{kin} + I_p$, where ω_{HHG} stands for the angular frequecy of HHG and I_p is the ionization potential of the gas target. Note that multiple re-collisions from the same electron may contribute to the high harmonic generation process. Since the electron wave-packet spreads with time, only the first re-collision is considered to give a significant contribution and later re-collisions are neglected.

Figure 2.1 is the calculated electron trajectory map. It shows the electron kinetic energy upon re-collision as a function of ionization and re-collision time. Each trajectory is defined by an ionization-recollison time pair. The trajectory map indicates that two trajectories support a particular high harmonic photon energy. The one with a travel time less than half an optical cycle corresponds to the "short" trajectory, and the other with a travel time

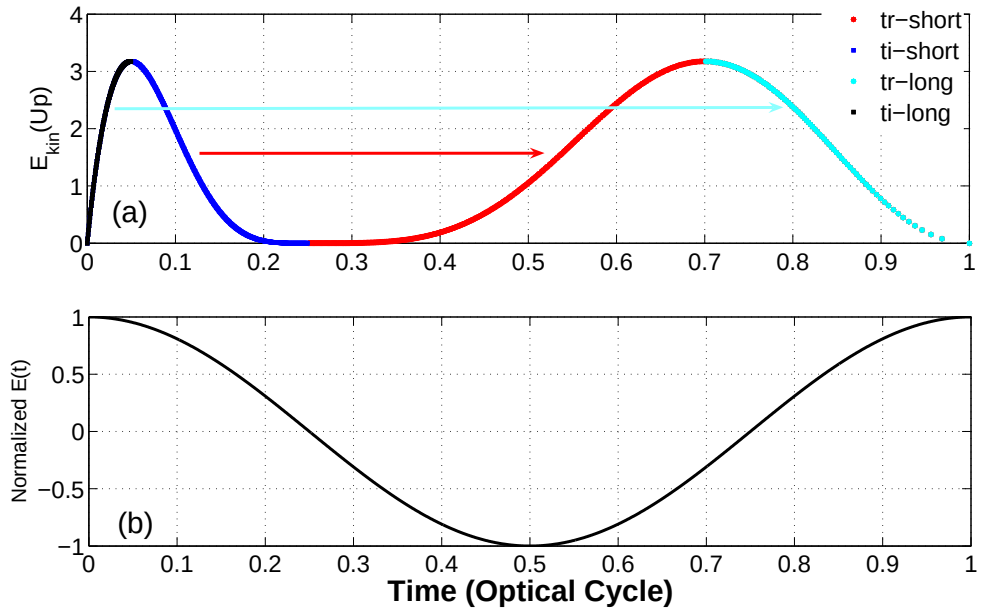

Figure 2.1: (a) Re-collision time (t_r) and ionization time (t_i) as a function of the electron kinetic energy (E_{kin}) upon re-collision. The red arrow indicates the short trajectory and the cyan arrow indicate the long trajectory. (b) The electric field $E(t) = E_0 \cos \omega t$ that accelerates the freed electron.

longer than half an optical cycle corresponds to the "long" trajectory. Both trajectories tend to become degenerate at the cut-off kinetic energy, $E_{cutoff} = 3.17U_p$, where U_p is the cycle averaged kinetic energy that the electron gains from the electric field—the so called the ponderomotive energy. From the time axis the whole process is occuring repeatedly every half optical cycle of the laser field, therefore providing an EUV pulse train with a period of $T_0/2$ (T_0 corresponds to the optical cycle of the laser field). The regular temporal structure of the pulse train results in a comb structure in the frequency domain with a repetition frequency of $2\omega_0$ (ω_0 stands for the angular laser frequency) based on the time-frequency relationship $\Delta T \times \Delta\omega = 2\pi$. Due to the inversion symmetry of the atoms, only induced polarization that is an odd function of the electric field can exist. Thus, the typical high order harmonic spectrum consists of frequency components with odd integer multiples of the fundamental frequency (see Fig. 2.2).

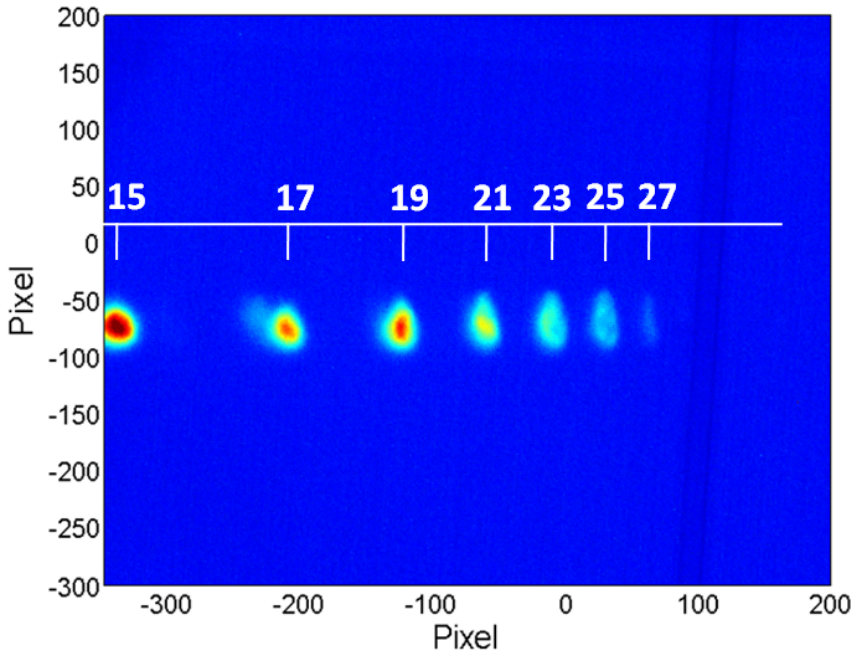

Figure 2.2: Typical high harmonic spectrum from a semi-infinite gas cell generated in our Laboratory. The HHG is diffracted by the grating of an EUV spectrometer and then captured by a beam viewer, which consists of an MCP set and a phosphor screen. The image on the beam viewer is monitored by a CCD camera.

The semi-classical three step model provides an intuitive physical picture of HHG. It predicts qualitatively the cut-off energy, the dominating quantum trajectories and the electric field polarization dependence of HHG spectrum. However, it is not adequate to gain essential quantitative information such as the conversion efficiency and the spectral amplitude and phase. Therefore, a quantum mechanical treatment needs to be used to get a deeper and more accurate insight of this process. A successful quantum model that was developed after the classical three-step model is the Lewenstein model [63,64]. It is a quantum mechanical model within the strong field approximation. The assumptions used within this model are: (a) only the ground state is considered (transitions involving the excited states are neglected). (b) the Coulomb interaction between the freed electron and parent ion is neglected. (c) ground state depletion is neglected. (d) the single active electron approximation is employed. This model starts from the time-dependent Schrödinger equation

(TDSE) in the length gauge, within the approximations listed above. The time-dependent dipole moment along an arbitrary unit vector $\mathbf{n}$ can be written analytically,

$$\vec{r}_{\mathbf{n}}(t) = i\int_0^t dt' \int \mathbf{n}\cdot\mathbf{d}^*(\mathbf{p}-\mathbf{A}(\mathbf{t}))\mathbf{E}(t')\cdot\mathbf{d}(\mathbf{p}-\mathbf{A}(t'))\exp[-iS(\mathbf{p},t,t')]d^3\mathbf{p} + c.c. \quad (2.4)$$

here $\mathbf{d}(\mathbf{v}) =< \mathbf{v}|\vec{r}|0 >$ is the dipole moment matrix element for the bound-free transition, $\mathbf{E}(t)$ and $\mathbf{A}(t)$ denote the electric field and its vector potential, $\mathbf{p}$ stands for the canonical momentum of the freed electron in the laser field, and $S(\mathbf{p},t,t') = \int_t^{t'} dt''(\frac{[\mathbf{p}-\mathbf{A}(t'')]^2}{2} + I_p)$ corresponds to the quasiclassical action.

In case of a linearly polarized electric field with the polarization direction along x, by applying a mathematical treatment, i.e. saddle point method, the x component dipole momentum can be simplified:

$$\begin{aligned} x(t) = i\int_0^{\tau} (\frac{\pi}{\epsilon + i\tau/2})^{3/2} d_x^*(p_{st}(t,t') - A_x(t)) d_x(p_{st}(t,t') - A_x(t')) \\ \times E(t')\exp[-iS_{st}(t,t')]dt' + c.c. \end{aligned} \quad (2.5)$$

t' and t denote the ionization and recombination time respectively, $\tau = t - t'$ is the excursion time of the freed electron, and S_{st} is the quasiclassical action calculated at the stationary point $p = p_{st}$. The Fourier transform of the dipole moment gives the high order harmonic spectrum with both amplitude and phase information. The terms in the integral of equation 2.5 are quite meaningful. The first term $(\frac{\pi}{\epsilon + i\tau/2})^{3/2}$ describes the speading of the wave-packet of the freed electron. The dipole matrix elements in the second and third terms represent the photoionization and recombination processes, respectively. The quasiclassical action $S_{st}(t,t')$ in the last term describes the motion of the freed electron in the laser field during its excursion time window $\tau = t - t'$. This equation captures the essence of the actual process of high order harmonic generation from a quantum mechanical point of view and is consistent with the semi-classical description in the three step model. The approximate analytical solution is very handy and speeds up the TDSE calculation process significantly.

At the same time, it predicts the characteristics of the HHG spetrum fairly well.

Although the Lewenstein model describes the general properties of HHG, it has its own limitations and will break down at a point beyond the approximations made in the model. (1) Due to the neglect of excited states in the medium, the harmonic orders below the ionization threshold are meaningless and therefore not reliable from this model. (2) With the Coulomb interaction being ignored, the freed electron wave-function is actually a plane wave (the so called Volkov state), thus upon ionization or recombination the differential cross section is considered to be identical for all atoms and molecules, which is not valid if we want to search for the structural information of the target of interest. (3) Since the depletion of the ground state is ignored, the HHG spectrum is not realistic in the case of a high intensity driving field where the ionization level could be very high and the ground state population is decreasing with time. (4) The single electron approximation obviously ignores electron correlation.

To circumvent all of these problems addressed above, an alternative approach is to solve the time-dependent Schrödinger equation (TDSE) numerically. Due to the very high dimensionality of multi-electron systems it is almost impossible to execute a TDSE calculation in full dimensionality. Therefore, a more sophisticated model is needed in order to reach a higher accuracy of the HHG description. The ground state depletion issue can be solved by including the ADK tunneling rate [65] term in equation 2.5. The single-electron approximation can be improved by using a model potential [66], in which the electron screening effect has been taken into account. The plane wave approximation (by ignoring the Coulomb interaction) can be improved with the Quantitative Rescattering (QRS) model developed recently by C.D. Lin's group at KSU [67, 68]. In this model, the induced dipole moment in the frequency domain $D(\omega)$ can be expressed as the product of a returning electron wave packet $W(\omega)$ and the photo-emission transition dipole $d(\omega)$ of the atom from the stationary scattering calculation: $D(\omega) = W(\omega)d(\omega)$. The electron wave-packet, $W(\omega)$, is a property of the driving laser field only and can be deduced from the standard SFA expression. There-

fore, the calculated spectrum using the QRS model will be target dependent. More details about QRS calculations can be found in references [69–71].

2.2 Propagation of HHG

So far, we have mainly discussed high order harmonics generation from a microscopic perspective, i.e. the single atom response. In reality, high harmonics are generated from medium which contains many atoms or molecules. If an 800 nm laser is focused on a gas target by a 0.5 meter lens, the typical focal spot has a diameter of about $d = 50$ μm, and the Rayleigh length can be estimated to be $z_R = 2.5$ mm. The effective focal volume is therefore $V = 2z_R \times \pi(d/2)^2 = 10^{-5}$ cm^3. Under typical operating conditions, the gas cell has a constant pressure on the order of 10 Torr, which corresponds to a rough atom density of 3×10^{17} cm^{-3}. Thus the high order hamonic photons are generated inside the effective volume containing a huge number of atoms on the order of 10^{12}. In such a macroscopic environment, several effects are important:

Phase matching: based on the quantum mechanical picture for single atom response, the phase of harmonic photons is related to the quasiclassical action which is intensity dependent. That means electrons experiencing different laser intensities will accumulate different phases in the laser field, and this phase information can be transferred to the resulting harmonic photons. In general, the driving field is cylindrically symmetric about the propagation vector and the intensity has a Gaussian distribution along the propagation and radial directions. Atoms located at different sites will emit harmonic photons with different phases. In addition, the driving field itself has a spatial phase distribution due to its divergence and the Gouy phase involved. This phase information will be transferred to harmonic photons as well [72]. The total harmonic yield is the coherent summation of all photons, thus we would expect constructive interference, which corresponds to the gain of harmonic yield, and destructive interference, which gives rise to the loss of harmonic yield. Harmonic

photon flux will not be enhanced by simply increasing the medium length due to this effect.

Nonlinear effect of the driving field: the intensity of the driving field for high harmonic generation is well beyond the linear optics regime. The dielectric polarization density $\mathbf{P}$ in the medium responds nonlinearly to the electric field $\mathbf{E}$ of the laser pulse, and can be described as a Taylor expansion: $\mathbf{P} = \varepsilon_0\chi^{(1)}\mathbf{E} + \varepsilon_0\chi^{(2)}\mathbf{E}^2 + \varepsilon_0\chi^{(3)}\mathbf{E}^3 + ...$, where ε_0 is the electric permittivity of free space, and $\chi^{(n)}$ is the n-th order susceptibility of the medium. The nonlinear high order polarizations will cause noticeable effects. For instance, the third order term indicates an intensity-dependent nonlinear refractive index of the neutral gas at the fundamental driving field wavelength. This will cause self-focusing of the driving field inside the medium. Another third order effect, self-phase modulation, broadens the frequency component of the fundamental field resulting in the modification of harmonic photon energies. Other than that, the medium can be partially ionized by the strong electric field and plasma will be created. Apparently the plasma density is laser intensity dependent, and therefore its refractive index shows a spatial distribution similar to the non-linear refractive index of the neutral gas. However, the plasma has a negative refractive index leading to the defocusing of the driving field while it propagates. These effects are competing with the self-focusing effect mentioned earlier, and can extend the focusing region dramatically—a phenomenon called laser filamentation. During the high harmonic generation process, the atom will generally undergo tunneling ionization which occurs every half optical cycle. This means that macroscopically the created plasma density (or refractive index) will be time dependent. Thus a time dependent phase will be transferred to the fundamental driving field while it is propagating, leading to a change of the instantaneous frequency of the electric field (i.e. a chirped pulse).

Dispersion: A pulsed laser field has a certain frequency bandwidth. The electrons inside the atom respond differently to different frequency components, which gives rise to a frequency dependent refractive index or the chromatic dispersion. In the highly ionized gas medium, the dispersion induced by the freed electron and neutral atoms will spread the

frequency components of the driving field temporally. Thus the pulse duration will become longer and the peak intensity will be reduced. Since chromatic dispersion also exists in high order harmonic fields, we expect that the phase velocity of the fundamental field is different from that of the high order harmonic field. This leads to a phase mismatch during high harmonic generation in a medium that will limit the conversion efficiency due to the finite coherence length.

Absorption: This effect is mainly referring to the absorption of harmonic photons by the gas medium. After the high order harmonic photons are generated, they can interact with the gas medium along the propagation path. The harmonic photons can be absorbed during the process of excitation or ionization of the target medium. The absorption length can be defined as $L_{abs} = \frac{1}{\rho\sigma}$ (ρ is the gas density and σ is the ionization cross-section) to describe the distance over which the photon may be significantly absorbed. This is another limiting factor of HHG conversion efficiency [73, 74].

In order to take into account the propagation effects mentioned above, the time-dependent Schrödinger equation (TDSE) or its equivalent SFA counterpart is coupled with Maxwell's equations. The wave equation deduced from Maxwell's equations is formulated as:

$$\nabla^2 E(r,z,t) - \frac{1}{c^2}\frac{\partial^2 E(r,z,t)}{\partial^2 t} = \mu_0 \frac{\partial J_{abs}(r,z,t)}{\partial t} + \frac{\omega_0^2}{c^2}(1-\eta_{eff}^2)E(r,z,t) \tag{2.6}$$

The terms on the left hand side are the Laplacian of the electric field $E(r,z,t)$ in Minkowski space. The terms on the right hand side indicate the medium environment that the field experiences. The dipole moment solution from the TDSE serves as a source for the wave equation 2.6. Technically, in order to solve the equation efficiently several approximations must be applied. Details can be found in references [75, 76].

2.3 HHG in time domain

As we mentioned earlier, HHG is a source of highly coherent soft x-rays. From the quasiclassical picture, high order harmonics are emitted upon the re-collision between the oscillating freed electron and its parent ion. From Fig. 2.2 the characteristic features of HHG can be summarized as follows:

(1) high harmonics are generated every half optical cycle of the driving field.

(2) for each high harmonic photon energy, the contributing electron trajectory is not unique except for the very highest photon energy. Two pathways with different excursion times contribute to the same photon energy.

(3) the re-collision occurs at different times for different energies indicating that the high harmonic field is chirped. The two pathways, i.e. short and long trajectories, possess different signs of chirp.

(4) the re-collision time window is of the order of sub-femtosecond. Thus, high harmonics are emitted in term of attosecond bursts.

The simple quasiclassical picture is easily understood and captures the main features of HHG, that have been confirmed by both theory and experiment [4, 5, 61, 63]. Based on this trajectory plot, the temporal structure of HHG can be classified into three categories depending on the driving field used. Figure 2.3 shows the simplified mechanisms of the generation of three types of attosecond pulses.

Attosecond pulse train with a period of a half optical cycle of the driving field

As is shown in Fig. 2.3, if a monochromatic field interacts with atoms, the electron will experience exactly the same trajectories no matter the electric field is pointing upwards or downwards along the polarization direction. Thus, the high harmonic radiation, which is created upon re-collision, will be emitted repeatedly whenever the electric field flips its

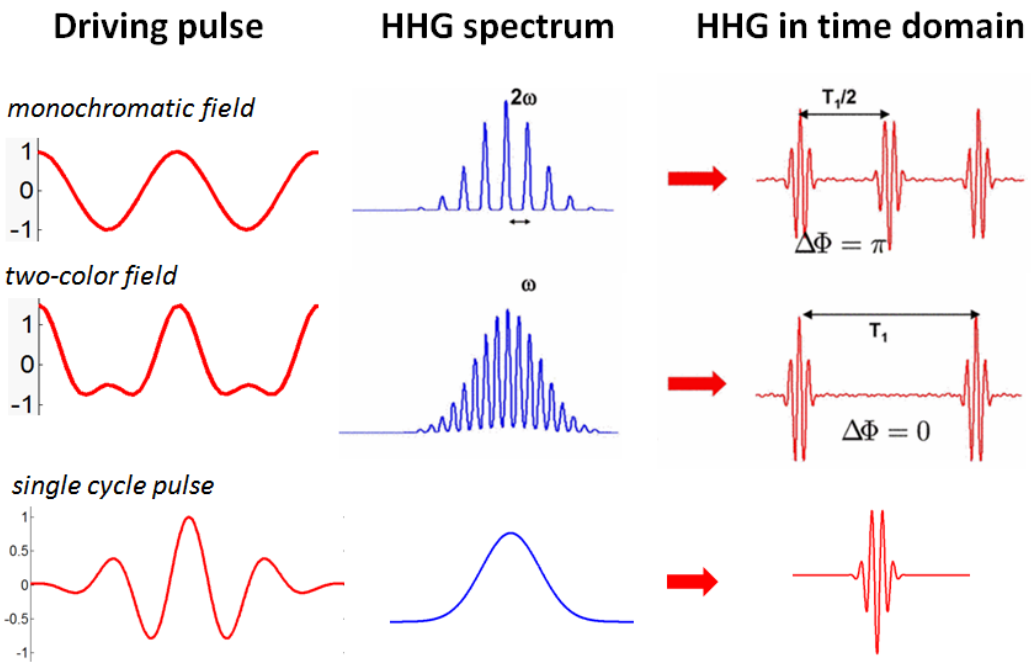

Figure 2.3: Three types of attosecond pulses and the associated HHG spectrum and driving pulses. See the text for details.

direction and gives a series of attosecond bursts with a period of $T_0/2$ (T_0 is the optical cycle of the driving field) [5].

Attosecond pulse train with a period of a full optical cycle of the driving field

The first type of attosecond pulse is basically determined by the temporal symmetry of the driving field. If we add a different frequency component to the monochromatic driving field, e.g by adding a second harmonic field, the temporal symmetry is broken. The middle row in Fig. 2.3 shows the electric field of a two-color driving field. The asymmetry of the combined electric field will ionize and accelerate the freed electron slightly differently for consecutive half fundamental cycles. The two attosecond bursts generated within one fundamental cycle are not identical, thus the period of this type of attosecond pulse train is a full optical cycle of the fundamental field. In the frequency domain this corresponds to harmonics with both

even and odd orders [77]. In general, a high harmonic spectrum consisting of both even and odd harmonics does not necessarily provide attosecond bursts separated by T_0 (unless the phase of the harmonic spectrum is flat) [78]. The relative phase of the two-color driving field has to be carefully chosen such that one attosecond burst is much weaker than its nearby companions, then we can say approximately that only one attosecond pulse is generated every full optical cycle T_0 of the driving field.

Isolated attosecond pulse

The third type of an attosecond pulse corresponds to the very extreme case of attosecond pulse train where all the pulses except one are significantly suppressed. Then the high order harmonic photons are emitted almost simultaneously within a sub-femtosecond time window. This can be realized either by manipulating the driving field or by tailoring the generated harmonic pulses. The spirit of all these techniques is isolating a single attosecond burst out of a train of attosecond bursts, so they are termed "gating" techniques.

A few gating techniques have been developed so far. In intensity gating, the driving field is an ultrafast few cycle laser pulse. The cut-off harmonics can only be generated near the peak of the intensity envelope within a fraction of a laser cycle, thus single attosecond pulse can be produced by spectral filtering near the cut-off region [1, 4, 22, 79]. In the polarization gating method, a left-handed circularly polarized laser pulse is synchronized to a right-handed circularly polarized laser pulse. The ellipticity of the combined laser field is time-dependent. The linear polarization portion of the light is a small fraction of an optical cycle that can support attosecond pulse generation (HHG is terminated in elliptically polarized driving field due to the suppression of re-collisions from a classical point of view) [80, 81]. Another gating technique is ionization gating [82–84], in which the driving field intensity is over-saturated for the medium gas. The neutral atoms/molecules can be ionized completely in the leading edge of the laser field. The rapid depletion of the ground state of the neutrals destroys the repetition of the re-collision process, and therefore isolated attosecond pulse

generation can be expected under proper spectral filtering. Because of the regular temporal structure of an HHG light source, extensive research has been conducted worldwide by using the HHG to study ultrafast dynamics of atoms and molecules in the past decade.

2.4 HHG in spatial domain

The spatial property of HHG mainly refers to the divergence of the electromagnetic field of the harmonics, or specifically how the wave vector of HHG is distributed spatially. This property will be discussed briefly, and the qualitative conclusions can be used to guide experiments.

Mathematically, the wave-vector distribution $F(\vec{k_h})$ can be evaluated by performing the Fourier transform of the HHG electromagnetic field:

$$F(\vec{k_h}) = \int |E_h| \exp(i\phi(\vec{r})) \exp(-i\vec{k_h} \cdot \vec{r}) d^3\vec{r}, \tag{2.7}$$

where $\vec{E_h}(\vec{r}) = |E_h(\vec{r})| \exp(i\phi(\vec{r}))$ is the harmonics field and possesses cylindrical symmetry about the propagation direction z. The radial direction distribution of the wave vector $F(k_h(r))$ indicates the divergence of $\vec{E_h}(r, z)$. The amplitude $|E_h(r, z)|$ governs the lower limit of divergence. For simplicity, let's assume that both the fundamental driving field and the high order harmonics field have the same radial amplitude distribution $|E_h(r, z)|$, which has a full width at half maximum Δr along the radial direction. According to the position-momentum uncertainty principal $\Delta r \Delta k_h(r) \geq \frac{\hbar}{2}$, the divergence is

$$\Delta\theta_h \approx \frac{\Delta k_h(r)}{|k_h|} = \frac{\Delta\theta_0}{N} \geq \frac{\hbar}{2N\Delta r|k_0|}, \tag{2.8}$$

where N is the harmonic order, and k_0 is the fundamental wave vector. Therefore, the divergence of high order harmonics is much smaller than that of the fundamental driving field, and in general it is inversely proportional to the harmonic order. A further detailed

evaluation of the divergence needs to consider the phase $\phi(\vec{r})$. A constant phase corresponds to the Fourier transform limited case, and thus represents the smallest divergence that can be achieved. Any non-linear terms in the phase will cause an increase of the divergence.

As we mentioned earlier, the phase of HHG is contributed by the atomic dipole phase and the phase of the driving field. The phase of the driving field is related to the Gouy phase of a Gaussian beam and any plasmas-induced distortion of the field. It mainly affects the efficiency and wavelength of HHG. The atomic dipole mainly determines the divergence of the HHG. According to the three step model, the atomic dipole phase equals the classical action of the electron with excursion time τ. The quantum-mechanical calculations suggest that this phase is approximately proportional to the peak intensity of the driving laser field. Thus it can be expressed as [85]:

$$\Phi(I)_{S,L} = \alpha_{S,L} I, \tag{2.9}$$

where I is the peak intensity of the driving field, and S, L stand for the short and long trajectories contributing to the high harmonic generation, respectively.

Since the excursion time of a long trajectory is larger than that of a short trajectory, the atomic dipole phase associated with long trajectory varies much faster with the laser peak intensity, i.e. $\alpha_L \gg \alpha_S$. The intensity distribution of the fundamental driving field can be written as $I(r, z, t)$. Thus, the dipole phase will be a function of r, z, and t. Although, the r dependence of the phase contributes to the divergence, note that both the z dependence and t dependence of the phase do have physical meanings: the z dependence of the phase influences the coherence length and thus determines the efficiency of HHG, and the t dependence of the phase introduces non-linear effects leading to frequency change of the HHG photons. The laser intensity along the radial direction r is a Gaussain distribution: $I(r) \propto \exp(-\frac{r^2}{W^2})$ with beam width W. Considering that high harmonic generation is a strong field process, only the peak region where r is very small contributes significantly to the HHG in general. The Taylor expansion of $I(r)$ yields a parabolic function around this region, $I(r) \propto I_0(1 - r^2)$, with $r \to 0$, I_0 is the peak intensity at $r = 0$. Therefore, the phase of HHG, $\Phi(I)_{S,L} \propto \alpha_{S,L}(1-r^2)$

leads to broadening of HHG divergence compared with the Fourier transform limited case. The long trajectory has a bigger divergence due to the larger coefficient α_L. In a real experiment a pinhole can be inserted along the optical path of the high harmonics, in which case the much less divergent short trajectory will dominate the HHG yield leading to a regular structure in both the spectral and temporal domains.

Chapter 3

Experimental method: pump-probe scheme with several harmonics

In this chapter the experimental method for conducting a pump-probe experiment using an HHG-based EUV source will be described in detail. In a general sense, a laser system is needed to provide both the intense driving field for HHG and the synchronized probe pulse. An optical interferometer is required to synchronize the pump and probe pulses. Finally, a detection system is used to record the products of the reaction (see Fig. 3.1).

3.1 Laser system

This section mainly describes the laser system that was used for conducting the experiment. The Coherent Ti:Sapphire ultrafast laser system consists of two sub-systems: the oscillator and a Legend Elite series amplifier. The oscillator is pumped by a Verdi-V series pump laser. The Kerr-lens passive mode locking technique is applied to generate a pulsed laser inside the cavity. A typical mode locked output from the oscillator has the following parameters: full width at half maximum pulse duration, 7 femtosecond; power, 300 mW; central wavelength, 790 nm; bandwidth, 50 nm; rep-rate, 80 MHz. The output of the oscillator serves as a

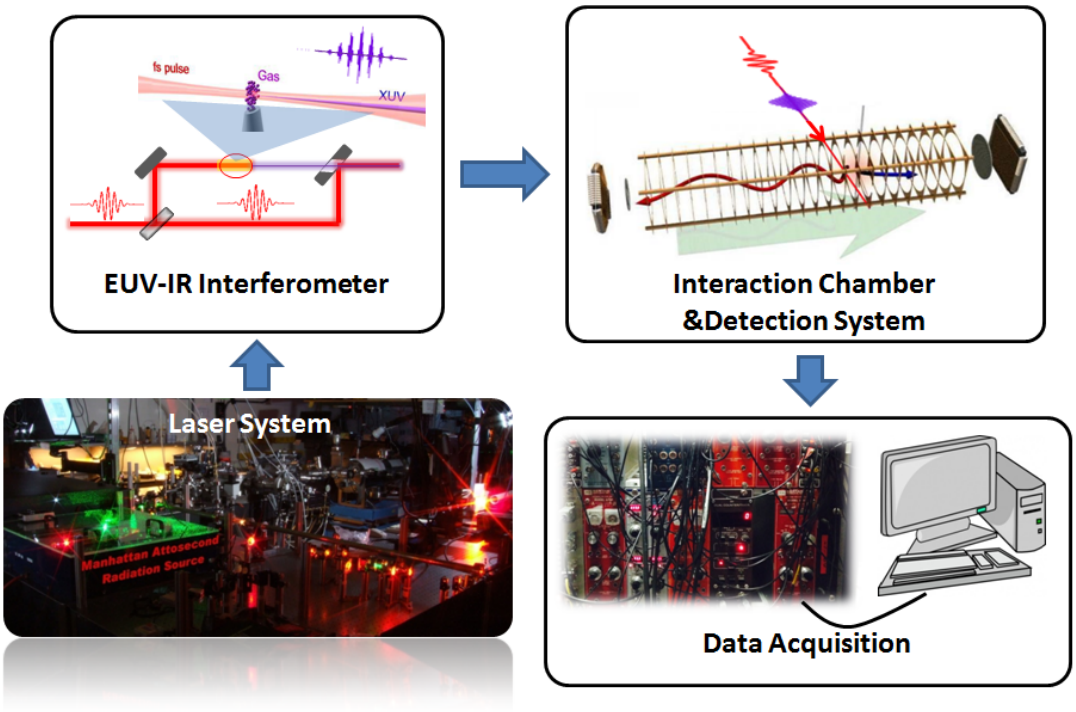

Figure 3.1: Block diagram of the overall system for the pump-probe experiment

seed pulse for the Legend amplifier. The chirped pulse amplification (CPA) technique [86] is employed to amplify the pulse energy from nJ to mJ. The schematic illustration of the amplifier is shown in Fig. 3.2. The seed from the oscillator is stretched from femtosecond(fs) to picosecond(ps) by a grating-based stretcher as a first step so that the pulse energy can get amplified without damaging the gain medium. Then the stretched pulse is amplified by a regenerative amplifier (10 round trips) followed by a single pass amplifier. The Pockels cells integrated in the regenerative cavity can change the polarization of the laser pulse. By controlling the timing of the Pockels cells, only one seed pulse per millisecond can be selected to pass through the Brewster window that seals the gain medium, and get amplified by the gain medium. Therefore the final output from the amplifier has a repetition rate of 1 kHz. As a last step, the amplified pulse is sent to a grating-based compressor to compress the pulse to ∼50 fs with pulse energy up to 6 mJ.

The 50 fs laser pulse from the amplifier can be further compressed down to sub-10

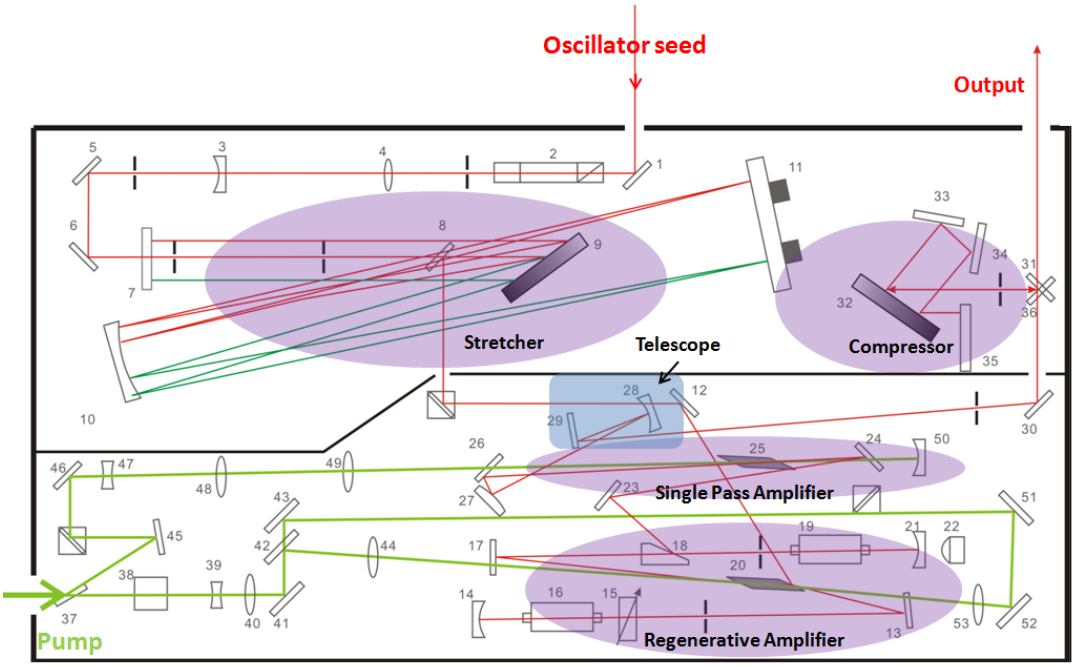

Figure 3.2: Layout of the amplifier of the Ti:Sapphire laser system

femtoseconds by using a gas-filled hollow core fiber. While the laser pulse is focused into the hollow core fiber with a core size of a few hundred microns, the interaction between the gas and the laser field leads to highly nonlinear effect such as self-phase modulation. The spectrum will therefore get broadened to support ultrashort pulse generation. A set of chirped mirrors after the hollow-core fiber is used to compensate the group delay dispersion in the broadband spectrum and generate sub-10 fs laser pulses.

The laser beam is then delivered to the experimental setup through a stainless transport tube. The purpose of this transport tube is:

(1) to block out any possible air flow that could induce fast fluctuations of the beam profile. The pump-probe experimental apparatus and the laser system are located in two different rooms (about 20 meters optical path length between the laser and the experimental setup). The slight temperature difference (less than 1 celsius degree) creates air flow along the path that connects the two rooms. This causes the air density fluctuations, and thus changes the instant distribution of the refractive index of the air along the beam path. Consequently

the beam profile of the laser changes while it passes from one room to the other.
(2) to provide a vacuum environment when necessary. When the high power laser beam is delivered in air, the intensity dependent nonlinear index of refraction could be noticeable and gives rise to effects such as self-focusing and self-phase modulation. Self-focusing can create hotspots in the beam profile after long-distance propagation which is harmful to optical elements. Self-phase modulation can lead to a spectrum change of the laser pulse and alter the pulse duration, especially in the short-pulse application.

3.2 Laser pulse characterization

Before conducting a strong field experiment it is important to get a rough estimate of the peak intensity of the laser pulse. The laser peak intensity for a Gaussian beam can be defined as:

$$I_0 = \frac{2P_0}{\tau(\pi r_0^2)} \tag{3.1}$$

where P_0 is the pulse energy, τ is the pulse duration and r_0 is the radius of the beam at the focal spot. The pulse energy can be obtained by measuring the power with a standard powermeter. In order to know the laser pulse intensity, we have to know the other two aspects of the laser pulse: the pulse duration τ and the beam size at the focus r_0.

3.2.1 Pulse duration

The pulse duration of the laser out of the amplifier can be measured using two methods in the lab: autocorrelation and Frequency Resolved Optical Gating (FROG).

Autocorrelator:

For an electromagnetic field with a pulse duration in the sub-picosecond region, there is no electronic device that is fast enough to record the temporal evolution of the field. The optical autocorrelation technique is then applied to measure the pulse duration. In an autocorrelator, the laser pulse itself is used to measure its duration. The principle can be

summarized as follows. The pulse to be measured is split into two copies by a beam splitter. The relative optical path length difference of the two copies is controllable with a mechanical delay stage. For a specific delay, both copies will be focused onto a nonlinear crystal to generate second harmonic signals. The autocorrelation trace is the second harmonic intensity as a function of delay between the two copies of the fundamental pulse. It is possible to deduce the pulse duration of the original pulse if we know the mathematical formula of the autocorrelation trace. The autocorrelation trace can be different depending on the optical arrangement of the setup. There are generally two types of autocorrelators: intensity autocorrelators and interferometric autocorrelators.

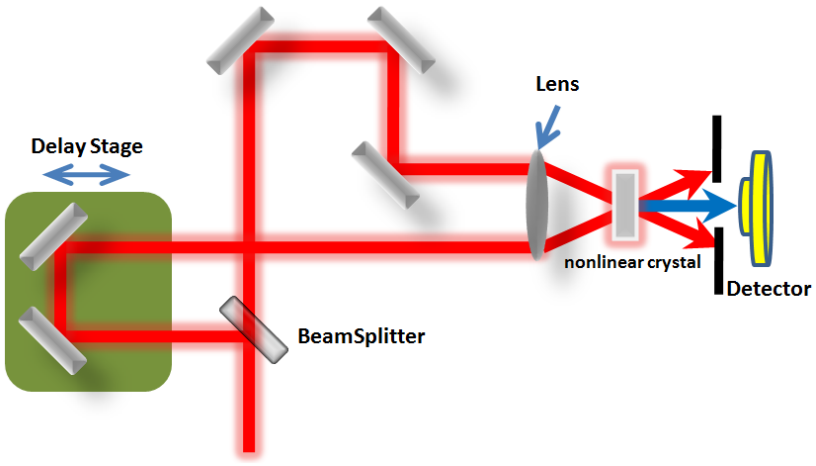

Figure 3.3: Layout of the intensity autocorrelator

In the intensity autocorrelator, the two copies of the original pulse are focused onto the nonlinear crystal with different angles (shown in Fig. 3.3). The phasematching condition ($K_1^{\omega_0} + K_2^{\omega_0} - K^{2\omega_0} = 0$, where K^{ω} is the propagation vector of light with frequency ω) corresponds to momentum conservation, and thus the second harmonic signal propagates along the optical axis. Its amplitude is the convolution of the two copies of the fundamental:

$$A(\tau) = \int I(t)I(t-\tau)\mathrm{d}t. \tag{3.2}$$

A (τ) is the autocorrelation trace. The width of the autocorrelation trace τ_A is directly related to the original pulse duration τ_o by a constant factor (the conversion faction) F: $\tau_A = F\tau_o$. In general we assume the original pulse is a Gaussian pulse, and the conversion factor $F = \sqrt{2}$. If the pulse energy is high enough, it is possible to set up a simplified intensity autocorrelator where the spherical focusing lens before the nonlinear crystal is replaced by a cylindrical lens. In this case, the laser pulses will be focused onto a line instead of a point. Different locations on the focusing line correspond to different delays between the two identical pulses. Thus by measuring the intensity distribution of the second harmonic along the focusing line the autocorrelation trace is recorded. Since only a single laser pulse is needed for the construction of an autocorrelation trace this is called a single-shot autocorrelator.

In the interferometric autocorrelator, both copies of the original pulse are focused onto the nonlinear crystal in a collinear configuration. The autocorrelation trace is written as:

$$A(\tau) = \int |E(t) + E(t-\tau)|^4 \mathrm{d}t \tag{3.3}$$

The interference between the two identical pulses will give rise to a periodic oscillation in the autocorrelation trace. The periodicity is half an optical cycle of the original pulse to be measured. The pulse duration can be retrieved by simply counting the number of oscillations in the autocorrelation trace.

Although the optical autocorrelator technique provides a simple method for short pulse measurement not achievable with traditional electronic devices, there are limitations to this technique. For pulses with duration less than 10 femtoseconds, this method is not reliable mainly due to the severe chromatic dispersion caused by the beamsplitter and nonlinear crystal, *etc.*. The autocorrelator also does not provide detailed spectral phase information of the laser pulse, which is rather essential for conducting an experiment involving a lager bandwidth short-pulsed laser. New techniques will be called to extend the intensity profile measurement to characterization of electric fields down to the sub-10 femtosecond region.

Frequency Resolved Optical Gating (FROG)

One of the popular techniques used for characterizing sub-10 femtosecond pulses is the Frequency Resolved Optical Gating (FROG) method [87, 88]. The schematic of the FROG setup is very similar to the intensity autocorrelator except that a spectrometer is used to record the second harmonic signal instead of a photo detector. There are different versions of FROG depending on the nonlinear crystals that are used. Here we only introduce the basic idea of the second-harmonic FROG used in our laboratory. The spectrometer can resolve the second harmonic signals in the frequency domain, and by recording autocorrelation traces for different frequency components a two-dimensional FROG trace is recorded.

An iterative algorithm starting from some random guess of the pulse is applied to reconstruct the FROG trace until a satisfactory agreement between the reconstructed and measured FROG trace is achieved. The intensity profile and spectral phase information can then be read off from the retrieved FROG trace. The FROG trace is symmetric about zero delay, so changing the direction of time will not change the FROG trace. This ambiguity introduces problems like undetermined sign of the chirp of the pulse. This problem can be solved by conducting further experiments. For example, a piece of fused silica can be added in the optical path. If the fused silica results in an increasing of the total chirp then the original 800 nm pulse possesses a positive chirp because the fused silica has a positive second order dispersion at 800 nm.

The single shot intensity autocorrelator is used to measure the pulse duration (50 fs) right after the amplifier of the MARS (Manhattan Attosecond Radiation Source) laser. The FROG is generally used to characterize the ultrashort sub-10 femtosecond pulse after the hollow-core fiber before delivering the pulse to the experimental setup.

3.2.2 Beam size

Conventionally a Gaussian beam, which is the approximate spatial solution to the wave equation, is used to represent the spatial profile of the laser beam. It has the expression in

cylindrical coordinates:

$$E(r,z) = E_0 \frac{w_0}{w(z)} \exp\left(\frac{-r^2}{w(z)^2} - ikz - ik\frac{r^2}{2R(z)} + i\eta(z)\right) \tag{3.4}$$

$$w(z) = w_0\sqrt{1+(\frac{z}{z_R})^2} \tag{3.5}$$

where w_0 stands for the beam waist, $z_R = \frac{\pi w_0^2}{\lambda}$ is the Rayleigh length, k is the wavenumber, $R(z)$ is the radius of curvature of the wavefront and $\eta(z)$ is the Gouy phase. After the focusing element, the beam radius at the focal point can be calculated from equation 3.5:

$$w_0(\lambda) \approx \frac{f\lambda}{\pi w}. \tag{3.6}$$

where f indicates the focal length of the focusing element, λ is the wavelength of the laser beam and w is the beam radius before focusing. Thus the spot size at the focus is proportional to the wavelength and the f number of the focusing element.

The Gaussian beam solution holds for a monochromatic field in general. For a pulsed laser with a finite bandwidth it is reasonable to use a superposition of Gaussian beams with different carrier frequencies to represent the beam profile. The laser beam coming out of the amplifier will be well-collimated up to the experimental setup. Let's assume that different frequency components have an identical beam radius w before focusing. Then different wavelengths will experience different degrees of spatial confinement after passing through a focusing lens or mirror according to equation 3.6. In case of a 50 fs 800 nm Fourier transform limited laser pulse, the bandwidth is about 25 nm. This wavelength bandwidth gives a 2% variation on the beam size at focus. It is thus a good approximation to use the beam size of a monochromatic 800 nm source to represent the beam profile for lasers with long pulse duration. However, the wavelength-dependent focusing effect will be noticeable for an ultrashort laser pulse spanning from 500 nm to 1000 nm. The longer wavelength possesses a beam size almost twice as big as that of the shorter wavelength. During the

interaction between the atoms and the laser beam, the atoms experience a higher degree of spatial confinement for short wavelengths and therefore effectively see a smaller bandwidth. Consequently the atoms experience a longer pulse duration than what is provided before focusing.

3.2.3 Intensity calibration

The calculated intensity of the laser pulse based on the measured beamsize and pulse duration is always an approximation. The intensity is in general overestimated for sub-10 femtosecond ultrashort pulses due to the wavelength-dependent focusing geometry mentioned above. Additionally, a fraction of the measured laser power is coming from incoherent amplified spontaneous emission (ASE), which will eventually cause an error in the estimation of laser intensity. More sophisticated methods will be needed to determine the laser properties accurately.

One way is to measure physical quantities that are sensitive to the electric field amplitude. For example, in a strong field ionization process, the ionized electron of an atom can have kinetic energy up to $E_{max} = 10U_p$ due to the back-scattering [89], where $U_p = \frac{E_0^2}{4\omega^2}$ is the ponderomotive energy with E_0 and ω representing the amplitude and angular frequency of the laser electric field, respectively. Thus by measuring the cut-off energy of the photoelectrons the electric field intensity can be determined. Also, we can measure the singly charged ion yield as a function of the laser power for a particular gas target, by fitting the theoretical prediction based on the ADK model to the experimental data, the intensity of the electric field can be retrieved. Alternatively A. S. Alnaser *el al*. demonstrated that the peak intensity of intense laser pulses can be precisely calibrated by measuring the momentum transferred to the ion in single ionization by circularly polarized light [90].

Another example of laser intensity calibration is the well-known attosecond streaking experiment. In this technique the isolated attosecond pulse is crossed with an IR pulse. The vector potential of the IR field can be directly mapped onto the delay-dependent pho-

toelectron spectra (the so called streaking spectrogram) according to momentum conservation [91]. However, the generation of single attosecond pulse is technically non-trivial. To ease the technical difficulty, an EUV-IR cross-correlation experiment can be performed with the attosecond pulse train. The IR electric field information can be extracted from the pattern of the delay-dependent photoelectron spectra. Fig. 3.4 shows a typical photoelectron spectrogram that is taken with the current pump-probe setup. The HHG-based EUV pump is generated from a two-color driving field consisting of 800 nm and 400 nm frequency components, and the EUV pump in the time domain is ideally an attosecond pulse train (APT) with periodicity of an optical cycle of the 800 nm driver. When this EUV pump is synchronized to an 800 nm IR probe pulse each individual attosecond burst is phase-locked onto the IR field at exactly the same relative phase. By changing the EUV-IR delay, each individual attosecond burst will create a streaking spectrogram with the same pattern. However, the spectrograms from consecutive single attosecond pulses differ from each other by a phase term that is related to the periodicity of the APT. The final spectrogram will be a coherent sum of all the individual streaking spectrograms. This method is rather similar to the single attosecond pulse streaking experiment except that interference fringes show up in the photoelectron energy. The mean photoelectron energy is oscillating with the EUV-IR delay. The energy peak to peak amplitude of this oscillation ΔE gives a momentum peak to peak amplitude of $\Delta P = \frac{\Delta E}{P_0}$, where P_0 is the momentum of the photoelectron gained from the EUV field only. From Fig. 3.4(a), $P_0 = 1.2\ a.u$ (20 eV photoelectron), $\Delta E = 5$ eV $= 0.184\ a.u$, thus $\Delta P = \frac{0.184}{1.2} = 0.15\ a.u$. The momentum conservation implies that the amplitude of the vector potential of the streaking field is $A_0 = \Delta P = 0.15\ a.u$, corresponding to a peak intensity of 7×10^{11} W/cm^2 at 800 nm. This estimation can be confirmed by a quantum mechanical model based on the strong-field approximation [92,93]. Figure 3.4(b) is the simulated spectrogram with the SFA model using a laser peak intensity of 7×10^{11} W/cm^2, and it agrees well with the experimental results as shown in Fig. 3.4(a). As a comparison, the intensity estimated based on equation 3.1 is 1.5×10^{12} W/cm^2, which is almost twice as

big as that calibrated from the pump-probe measurement.

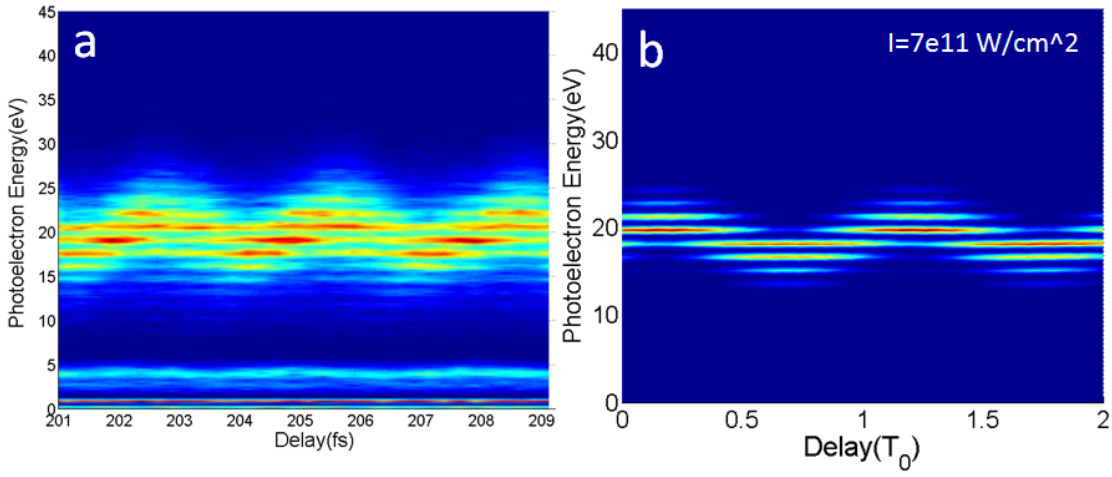

Figure 3.4: The delay-dependent photoelectron spectra of argon with high harmonics generated by a two-color driving field. (a) experimental result, (b) theoretical simulation based on strong field approximation. The IR probe is about 50 fs long; only a small fraction of the spectrogram is shown for intensity calibration. The IR probe intensity is calibrated to be 7×10^{11} W/cm^2.

3.3 Experimental setup

The experimental setup following the laser system is consisting of EUV-IR interferometer and a COLTRIMS imaging system.

3.3.1 Interferometer

The geometry of the Mach-Zehnder interferometer is illustrated in Fig. 3.5. Table 3.1 shows the specifications of the optical elements used in the interferometer. The incoming laser beam is split into two halves by an anti-reflection (AR) coated broadband beam-splitter (Femtolaser). One part of it is focused into the gas cell for high harmonic generation. The typical pressure inside the gas cell is 40 Torr for Ar and 20 Torr for Xe for optimized HHG photon flux. The gas cell is located in a chamber with a background pressure below 10^{-4}-

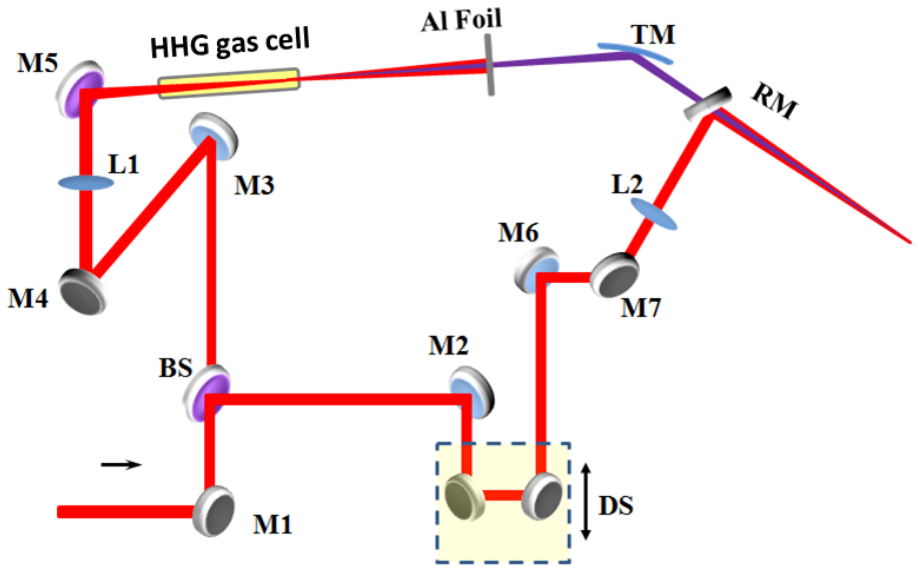

Figure 3.5: Schematic of the EUV-pump IR-probe interferometer

Torr to avoid absorption of EUV photons by the background gas. The generated EUV beam then passes through a 200 nm Al foil to eliminate the IR field before hitting the toroidal mirror, which focuses the EUV light onto the target. At the end of the interferometer there is a recombination mirror, which is a silver mirror oriented at 45 degrees with a 2 mm hole in the center. The EUV beam is delivered through the hole and focused onto the COLTRIMS chamber. The second half of the laser beam gets reflected by the beamsplitter and travels in the air. A delay stage driven by the piezoelectric transducer is inserted in the beam path to provide high precision change of the optical path length. After the delay stage, the IR beam is focused into the vacuum chamber and gets reflected by the recombination mirror. Eventually, the second part of the laser pulse will propagate collinearly with the EUV beam after the recombination mirror. The optical path length of the IR pulse is adjusted to be the same as that of the EUV beam, and therefore a pump-probe experiment can be conducted. In order to find out the time zero where the EUV and IR pulse simultaneously arrive at the recombination mirror, the retractable Al foil in the HHG beam path is pulled out to let the residual IR pulse pass through serving as a reference. Thus we have two visible IR beams,

Optical Element	Lable	Description
Flat Mirrors	M1-M7	Protected silver mirrors
Lens	L1	BK7 Bi-Convex lens, f = 0.5 m, AR coated
Lens	L2	BK7 Bi-Convex lens, f = 1 m, AR coated
Toroidal mirror	TM	R1 = 7370 mm, R2 = 136 mm, incident angel = 7.8°
Filter	Al F	0.2 μm aluminum foil
Beam Splitter	BS	Broadband beamsplitter 50/50 for S polarization
Recombination Mirror	RM	Flat mirror with 0.2 mm through hole in the center
Delay stage	DS	Piezoelectric transducer with 5 nm repeatability

Table 3.1: Specifications of the components for the interferometer

and the time zero can be identified by searching for an interference pattern between the two beams.

The stability of the interferometer is crucial for conducting a pump-probe experiment. Any external disturbance such as temperature fluctuations, air flow,or mechanical vibrations of the optical table and turbo-pumps can cause variation in the optical path length leading to jitter and drift of the relative delay between the two paths of the interferometer. The fast jitter of the delay degrades the resolution of the interferometer, while the slow drift on the delay can cause unphysical results. Thus, care must be taken while designing and aligning the system in order to keep the performance of the interferometer optimized. The air flow effect can be minimized by keeping the whole system in an enclosed environment. The mechanical vibration from the turbo pumps can be isolated by using flexible bellows at critical junctions. Rigid and heavy optical mounts are preferred for the beam-splitter and recombination mirror so that the fast vibrations, which are far from the resonance, can be damped. The only disturbance left is associated with the slow temperature fluctuation of the environment, which can vary by up to 2 Celsius degrees within an hour. The optical elements on the two paths of the interferometer cannot be identical, therefore the thermal expansion of the materials will cause slightly different changes on the two optical path lengths if the temperature changes. We then expect a slow drift of the relative delay on the interferometer (see Fig. 3.6).

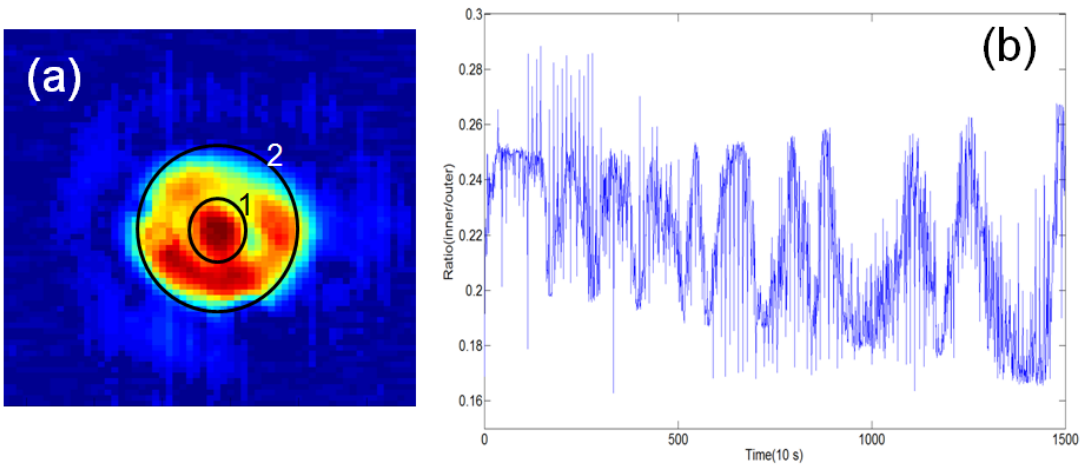

Figure 3.6: (a) The interference pattern recorded on a CCD camera when the two IR beams of the interferometer overlap. (b) The intensity ratio as a function of time. The intensity ratio is defined as the intensity integral inside circle 1 divided by the intensity integral between circle 1 and circle 2. This ratio depends on the relative delay between the two beams. The data shows on average a 20 minute oscillation of the interferometer, which is mainly due to the temperature fluctuation.

In general a locking technique is required to avoid the slow drift problem. In this technique, a reference light with a different wavelength will be aligned carefully to mimic the optical path of the IR pulses after the beamsplitter, and generate an interference pattern. The locking of the interferometer can be implemented by locking the interference pattern of the reference light [94]. Alternatively, the slow drift can also be corrected by performing a Fourier analysis of the experimental data without a locking system. In our experiment, we applied the latter approach to correct error induced by the slow drift of the interferometer. Fig. 3.7 shows the procedure for the correction. The measured data shows the photoelectron energies as a function of EUV-IR delay, which should in principle have a periodicity of one optical cycle of the IR field (2.667 fs), with the corresponding angular frequency ω_0 having a photon energy of 1.55 eV. However, as the delay is increased the period gets smaller in the raw data indicating a drift of the relative delay in the interferometer. By performing the transformation: $\tau_{corr}(\tau) = \int_0^\tau \frac{\omega_c(\tau)}{\omega_0} d\tau$, the periodicity of the photoelectron spectra is guaranteed to be 2.667 fs and thus is more suitable to represent the real physical process.

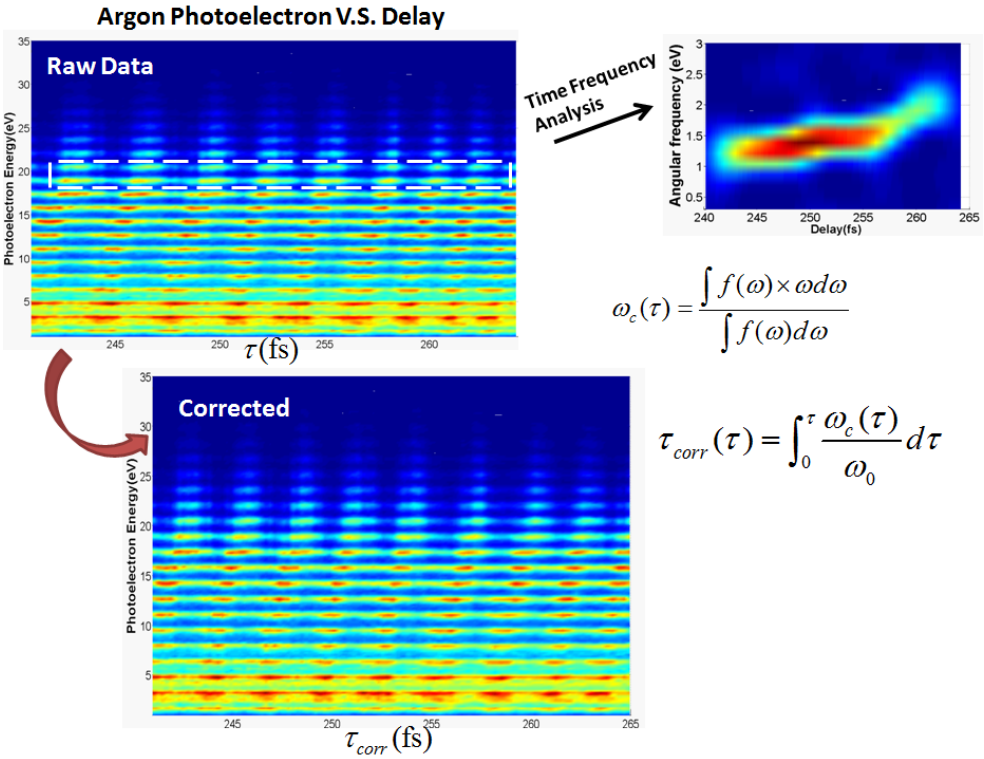

Figure 3.7: Correction of the delay drift embedded in the pump-probe experiment data. High harmonics with both even and odd orders are combined with an 800 nm IR pulse to ionize the argon gas target. Photoelectrons are collected for 30 seconds for each delay with a delay step size of 0.25 fs. Gaussian window is used to perform a time-frequency analysis of the band indicated by the dashed white box. $\omega_c(\tau)$ denotes the mean angular frequency at delay τ. ω_0 is the angular frequency of the IR field. The delay-dependent photoelectron yield in the raw data shows an increase of the periodicity with delay due to the drift of the interferometer. This effect is corrected in the bottom spectrogram.

High harmonic generation unit

The EUV light used in the pump-probe scheme comes directly out of the high order harmonic generation gas cell. It consists of multiple harmonic orders up to a cut-off photon energy of about 40 eV. From the experimental point of view, the two key aspects of performing an EUV-IR pump probe experiment are the photon flux and the time domain structure of the HHG-based EUV light. The higher photon flux and regular temporal structure of harmonics are preferred in order to conduct the dynamic study of a quantum system at a

reasonable pace. These can be realized by optimizing the phase matching process during the high harmonic generation. To be more specific, high harmonics generated from different atoms can add up constructively, and one out of the two quantum trajectories (the so-called short and long trajectories) can dominate in the harmonic spectrum. Several different types of gas units have been tried on the current setup for high harmonic generation.

The very first version of the gas unit was a gas-filled capillary waveguide that is 2.5 cm long and 150 μm in diameter. The detailed schematics can be found in [95]. The advantage of using the waveguide is that the HHG can be phase-matched over a relatively long distance. This is because the intensity of the driving laser is almost constant inside the waveguide and thus possesses a plane-wave feature. The phase matching condition can be achieved by simply balancing the dispersion of the neutral gas with the dispersion caused by the waveguide geometry and free electron. Therefore the high harmonic pulses can be optimized by tuning the gas pressure. However, from our experience the capillary waveguide requires sophisticated laser conditions. For instance, careful alignment is needed to couple the laser into the waveguide properly, which will automatically require very good laser pointing stability; a relatively lower intensity is required to avoid damage on the waveguide and prevent strong plasma effect. Therefore extra technical effort was needed in order to achieve the best performance of the waveguide.

A second gas unit for high harmonic generation is a thin glass tube with an inner diameter of about 2 mm. Gas is sealed inside the glass needle. The driving laser will be focused onto the wall of the glass tube and drill holes so that the high harmonics can propagate out through the holes. This gas cell does not require dedicated laser alignment or very crucial laser pointing control. The phase-matching condition can be easily achieved by moving the location of the glass needle with respect to the laser focus. However, it suffers from a low conversion efficiency due to the relatively short interaction length (2 mm).

A third gas unit for high harmonic generation is the so-called semi-infinite gas cell. A 30 cm cylindrical tube is sealed with a transparent window on one side and an exchangeable

Gas	Pressure	Pulse energy @50 fs	Focus position
Ar	40 Torr	2 mJ	0.5 cm before the cell exit
Xe	17 Torr	1.2 mJ	0.5 cm before the cell exit
O_2	25 Torr	2 mJ	0.5 cm before the cell exit

Table 3.2: Typical optimized conditions for HHG from a semi-infinite gas cell

thin metal sheet on the other side. The driving field will pass through a lens before the thin entrance window and get focused onto the metal sheet with a thickness of about 100 μm. A 200 μm to 300 μm hole is drilled in the metal sheet within a few seconds and the cell is ready for high harmonic generation thereafter. It is called a semi-infinite gas cell due to the fact that the gas cell is much longer than the Rayleigh length of the driving laser pulse and thus the whole focusing volume is the interaction region [96–98]. The major advantages of the third gas unit are: (1) the conversion efficiency is high due to the increased interaction length, (2) the alignment of the beam is trivial, and (3) it is technically easy to handle. Although the phase matching issue may be more complicated due to the Gouy phase and intensity variation across the focusing volume, several experimental tricks can be used to optimize the high harmonic generation process. For example, an aperture is inserted before the focusing lens, so that the intensity and profile of the harmonic spectrum can be tuned by varying the aperture size. Furthermore, by shifting the location of the focal point of the driving field the bandwidth of a single harmonic order can be controlled to some extent. We chose to use the semi-infinite gas cell to reach a compromise between the efficiency and tunability of our HHG source. It has to be admitted that the phase matching of HHG can only be described qualitatively. The optimized experimental conditions vary from run to run. The typical experimental conditions are listed in table 3.2.

3.3.2 COLTRIMS (Reaction microscope)

COLTRIMS stands for Cold Target Recoil-Ion Momentum Spectroscopy. It is an imaging technique for 3-D momentum construction of fragments from a few body system [99, 100].

While a neutral few-body system is broken up via collision with electrons/ions/photons, the charged fragments will be extracted by a combination of electric and magnetic fields created inside the COLTRIMS spectrometer and then hit the detectors. From the measured time of flight and the impact positions of the fragments on the detector, the momentum vector of each fragment can be retrieved. The key components of COLTRIMS are the spectrometer, gas jet, position sensitive detectors and data acquisition system.

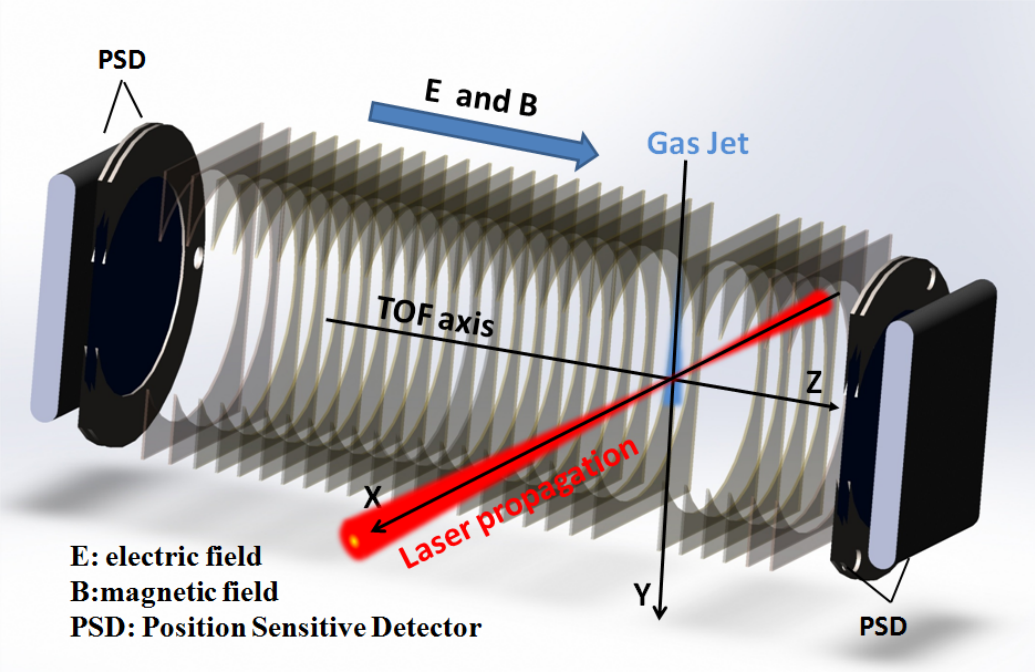

Figure 3.8: Sketch of COLTRIMS spectrometer

Spectrometer

Figure 3.8 shows the sketch of the COLTRIMS spectrometer (see appendix D for realistic image). It mainly consists of a series of thin brass plates and two position sensitive detectors sitting on the two ends. The plates are equally spaced except for the two close to the gas jet, which have a bigger gap serving as the interaction region. Each plate has a circular opening cut in the middle so that the reaction products can travel through the spectrometer. The

Plate dimension	Opening cut diameter	Resistor/Spacing	No. of plates
6 inch × 6 inch	8 cm	2.5 MΩ/mm	47

Table 3.3: Specifications of the COLTRIMS spectrometer

plates are connected with resistors proportional to the spacing of adjacent plates (specifically 2.5 MΩ), thus a homogeneous electric field is created within the spectrometer by applying voltage on the two end plates. The current spectrometer is designed to be asymmetric with respect to the interaction region. The distance is 21 cm from the reaction region to one detector and 5.5 cm from the interaction region to the other detector. In general, the detector located at the longer side of the spectrometer is used to collect electrons while the ions are detected on the short side. By applying a proper voltage across the spectrometer the heavy ions can be collected in 4π solid angle on the short side, and the light electrons can be collected on the long side with acceptable momentum resolution. An additional homogeneous magnetic field parallel to the E-field can be provided by two Helmholtz coils. This can bend the electron trajectories lead to a 4π solid angle detection. In such a configuration, coincidence measurements can be performed by collecting electrons and ion fragments on both sides simultaneously. Table 3.3 shows the dimensions and electronic components of the spectrometer.

The two plates at the end of the spectrometer have a high transmission (T = 80 %) mesh (250 μm× 250 μm mesh hole) attached to them. They are used to shield the strong static electric field caused by the high potential difference between the micro-channel plate (MCP) and the mesh. The voltages on the front MCP for the ion detector and electron detector are -2000 volts and 0 volt with respect to the earth potential, respectively. The voltages on the two meshes of the spectrometer are 0 volts for the electron side and -100 volts for the ion side. With the help of the meshes the electric field of the MCPs can be shielded to some extent while charged particles can still pass through the meshes.

Gas jet

In general, a well collimated supersonic gas jet is used as a gas target in the case of high resolution experiments [99,101]. The multi-stage collimation process can significantly reduce the width of the transverse momentum distribution (perpendicular to the jet direction) of the jet. The momentum width is determined by the geometry of the whole cold jet system (distances between nozzle, skimmers and slits). However, in our EUV-IR pump-probe experiment, the very low conversion efficiency of HHG (on the order of 10^{-6} or less with 800 nm driving pulses) gives a too low counting rate when interacting with a supersonic cold jet. Thus we used a diffusive jet which has a much thicker target than the usual supersonic jet [102].

The effusive jet is essentially a 3 cm long stainless steel needle with 1 mm inner diameter attached to a high pressure environment(2∼3 atmospheres). The quick expansion of the gas out of the needle is directional and provides a thicker local gas density of 10^{-4} Torr a few millimeters away from the needle tip. The interaction region is about 1.5 mm below the needle tip. If the needle is an insulator, the charged particles produced by the interaction can charge the needle up while colliding with it. This effect will distort the homogeneous static-electric field across the spectrometer. Thus, the needle has to be conductive to carry the extra charges away. This is achieved by applying a constant voltage on the needle. The voltage has to coincide with the potential at the same location within the COLTRIMS spectrometer in the absence of the needle. Since the effusive jet is internally "hot" compared to the supersonic gas jet, the thermal motion of the atoms and molecules degrades the ion momentum resolution. In COLTRIMS experiments involving the laser, the laser beam can be focused into a small volume with the size of $w_0^2 \times Z_r$, where $w_0 = 50$ μm is the typical beam waist, and Z_r =1 cm the typical Rayleigh length of the laser beam used in our experiment. The small cross-section of the laser beam at the focal point acts as an effective slit limiting the thermal distribution of the gas target along both the jet and TOF axis. The momentum resolution along the jet direction is improved effectively. Thus, the size of the interaction

region is crucial for determining the system resolution.

Multi-hit detector

The configuration of the detector used in the current setup is standard. Each detector consists of two micro-channel plates (MCP) stacked in a chevron configuration and a square delay-line anode.

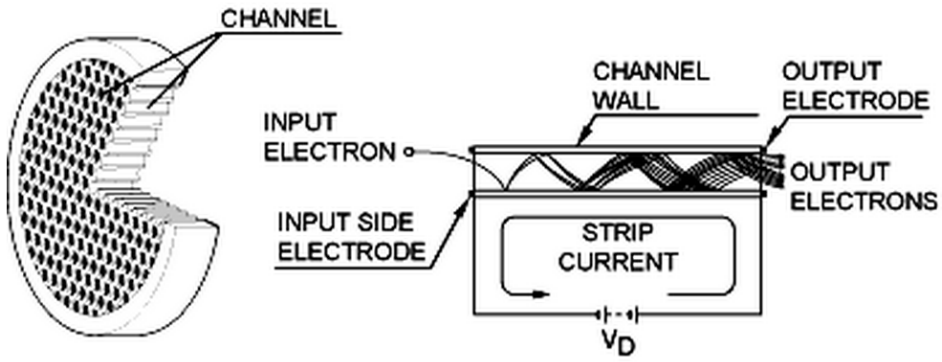

Figure 3.9: Principle of micro-channel plate operation, adapted from [103].

The basic principle of MCP operation is shown in Fig. 3.9. Each MCP possesses an array of micro-channels with typical diameter of 20 μm. The charged particles impacting on the MCP can release electrons from the surface. The electrons passing through each micro-channel will bounce off the inner wall multiple times and emit secondary electrons. Eventually the signal coming out of the back side of the MCP stack is an amplified electron cloud. The delay-line anode will collect the electron cloud to decode the position and timing information of the impact event. The square delay-line anode has a square frame with two wires wrapping around the frame in orthogonal directions creating a grid pattern (shown in Fig. 3.10).

When the electron cloud lands on the delay line anode, electron signals will be induced on each wire and propagate along both directions. Each impact event on the MCP will result in a pair of pulsed electron signals recorded on the two ends of each delay-line wire.

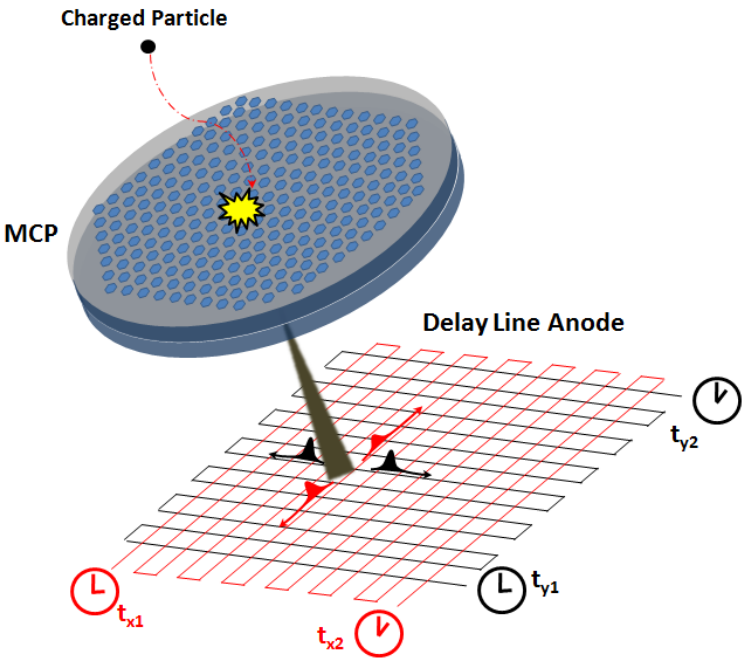

Figure 3.10: Working principle of a multi-hit delay-line detector. Particles impacting on the MCP surface generate an amplified electron cloud at the MCP stack exit. The amplified electron signal lands on the delay-line anode and creates two pairs of signals with timings t_{x1}, t_{x2} and t_{y1}, t_{y2}. The position of the impact on the MCP surface can be calculated from the timing information.

The time difference between the two signals tells by how much the electron cloud on the delay-line anode is off center in the direction associated with the wire direction. Therefore, two dimensional coordinates can be constructed for positions of the electron cloud (or the impact event) if we assign x and y to the two wires, respectively. Assuming that the center of the anode is the origin, it is rather straightforward to formulate the coordinates of the electron cloud as:

$$x = g_x(t_{x1} - t_{x2}) \tag{3.7}$$

$$y = g_y(t_{y1} - t_{y2}) \tag{3.8}$$

where t_{xi}, t_{yi} (i = 1,2) denote the timing of the electron signals arriving at the ends (1 and 2) of the wires (x and y), and g_x and g_y are the conversion factors that transfer the timing (ns)

information to position (mm) information and thus have the dimensions of speed (mm/ns).

Typically some background noise will also induce electron signals on the wires of the delay-line anode. To eliminate this noise, each of the x and y wires consists of a wire pair. The two parallel x (y) wires are close to one another and are labeled as "signal" and "reference". The "signal" wire is maintained at a potential of +50 V with respect to that of the "reference" wire. Therefore the electron cloud from the MCP will preferentially be picked up by the "signal" wire while the noise can be picked up by both "signal" and "reference" wires. By subtracting the signals on the reference wire from those on the signal wire, the noise can be eliminated. This signal subtraction is implemented by using a home-made differential amplifier circuit.

Data Acquisition System

The data acquisition system includes the electronic components for data collection and the software that is used for data taking as well as for off-line data analysis. The diagram of the electronic units is shown in Fig. 3.11. The data collection procedure for each interaction event consists of three blocks: the electron detector, the ion detector and the photodiode detector.

The photodiode detector records the signal of each laser pulse, and the timing of the signal will be registered by a subsequent constant fraction discriminator (CFD). The discriminated timing of each laser pulse will be fed into different channels of the CAMAC system for the following purpose:

(1) ADC strobe channel will wake up the TDC unit and enables the communication between the CAMAC crate and the computer;

(2) The photodiode signal fed into TDC will serve as a "time zero" of each interaction event so that the time-of-flight information of particles impacting on MCPs can be extracted;

(3) the COMMON channel defines the time window of the TDC, and signals with a time of flight (TOF) larger than the time window will be abandoned.

The electron and ion detectors have rather similar electronic blocks except that the bias voltages are different. After each interaction event between the laser pulse and the gas target, the particles (electrons or ions) created will impact on the detectors and generate pulsed signals on the delay-line anode. These signals first pass through the differential amplifier for amplification and noise reduction purposes. Then the timing of the amplified signals will be discriminated by the CFD before being sent to the TDC for TOF conversion. The LeCroy 3377 TDC is a 32 channels multi-hit converter with a time range of up to 32 μs and a resolution of 500 ps.

A Labview program developed mostly by former student Timur Osipov is used for data collection in an event by event mode, that is the TOF and position information of particles from each laser shot are registered. The Labview program gives preliminary on-line information such as the time sum, position image, and time-of-flight spectrum. More accurate and careful off-line data analysis requires a Fortran based program, Physics Analysis Workstation (PAW). Precise reconstruction of the physical quantities such as momentum and energy requires the predetermination of a few experimental constants: initial time (t_0), initial position (x_0, y_0), distance of flight (S) and the field strength (E, B). In principle, all these constants could be predetermined if the whole system is designed and measured very carefully. However, any change of the setup, i.e. the optical alignment, the electronic units, or the location of the gas jet, could change the values of these constants. This problem is solvable thanks to the fact that the COLTRIMS is a self-calibrated system. Some of the constants can be calibrated from the raw data itself thus accurate data analysis is guaranteed. A detailed discussion of the calibration process can be found in appendix A.

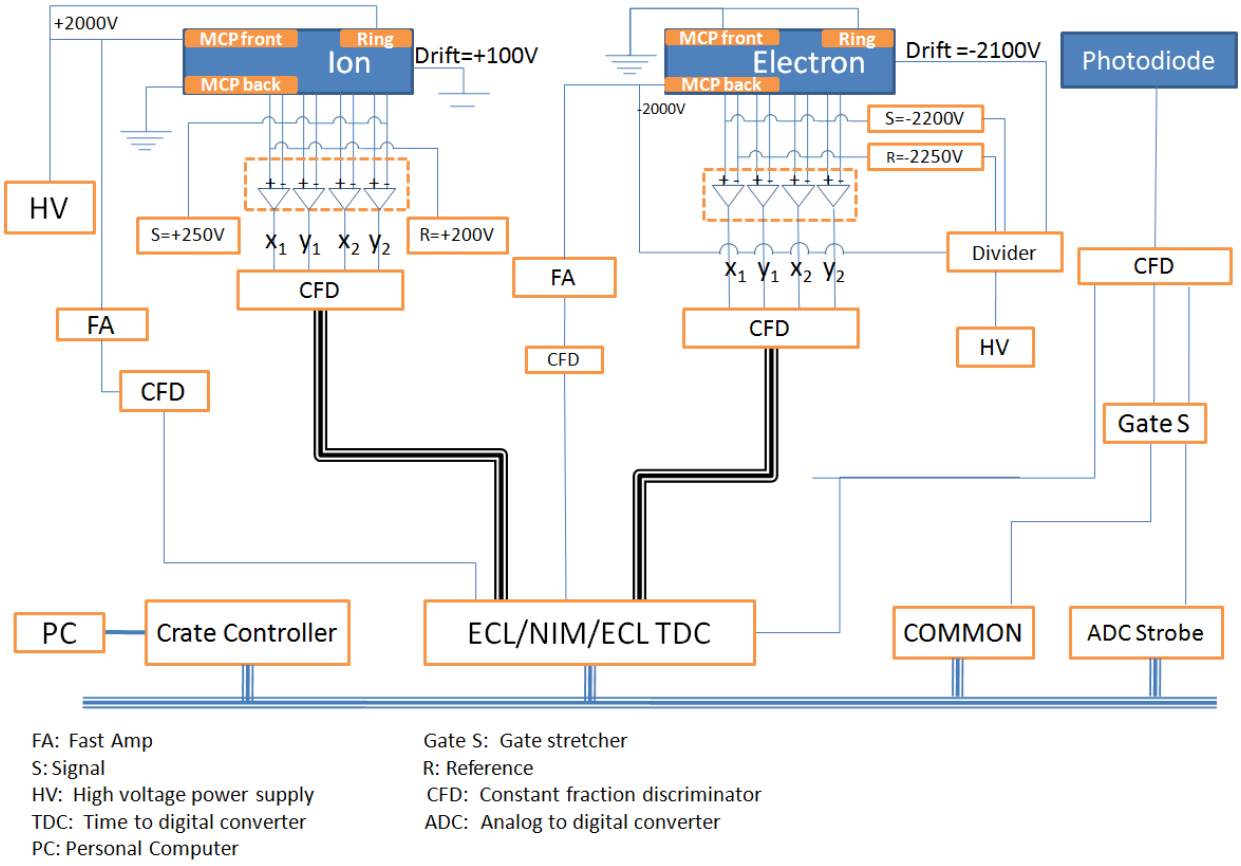

Figure 3.11: The diagram of the data acquisition system electronics

Chapter 4

Pump-probe studies of molecular dynamics

4.1 Background

The pump-probe method with HHG-based EUV as the pump and IR as the probe is a recent development. When a gas-phase target is exposed to an EUV-IR combined light source, the interaction can be simplified as a two-step process. Firstly, the EUV burst, which is a weak perturbation, can excite or ionize the target via a single photon process. The spectral range and timing of the first step are known with an uncertainty that is governed by the time-energy uncertainty relationship. Secondly, a delayed intense IR pulse will generally fragment the system prepared by the EUV burst via a multiphoton process. The products recorded at each delay between the pump and probe correspond to a "snapshot" of the process of interest. Dynamic evolution can be decoded by analyzing these time-resolved "snapshots". Unlike the more mature IR-pump IR-probe scheme, where the intense femtosecond IR pump strips the outermost shell electrons via multiphoton or tunneling ionization, the EUV pump not only provides sub-femtosecond time resolution but can also access inner shell electrons if the photon energy is large enough. By removing an inner shell electron, the corresponding

ion counterpart is left in an excited state followed by the rearrangement of the remaining electrons. The time-resolved behavior of this rearrangement process can be tracked by using an IR probe. One phenomenon associated with this electron configuration rearrangement is autoionization [41–44,46,48]. The physical process of autoionization is illustrated in Fig. 4.1.

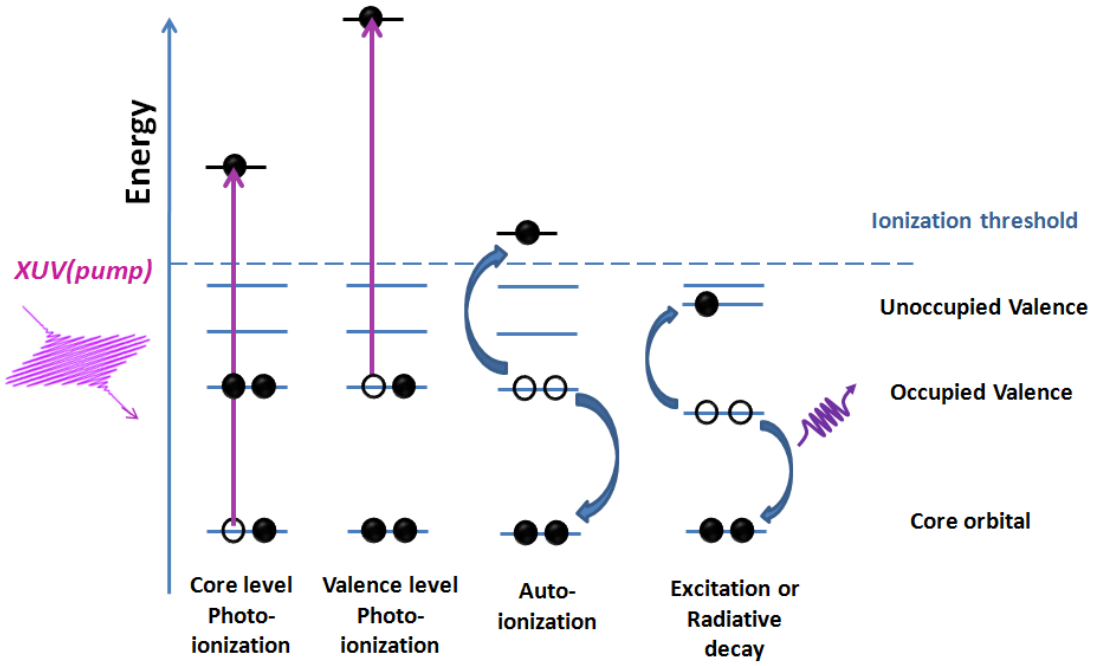

Figure 4.1: Schematics of electron rearrangement after EUV photoionization. Adapted and modified from Fig. 2 in reference [104].

In this process, an inner shell electron is knocked out via photoionization, creating an inner shell vacancy. A valence electron can fill the "hole" associated with the liberated inner shell electron, while a second valence electron will carry away the transition energy offered by the first valence electron and then the ion gets further ionized. The autoionization is energetically allowed only if the transition energy associated with the first valence electron is greater than the binding energy of the second valence electron [104]. In atoms, if the autoionization is energetically not allowed, the excited ion will decay into its ground state by emitting photons instead of electrons. However, for molecules, autoionization can still occur even it is forbidden when the excited cation is created. Since electrons are shared by multiple nuclei in the molecular environment, the electron binding energy depends on the geometric

configuration of the nuclei in the molecule. After photoionization the molecular cation will rearrange itself and evolve toward a more stable configuration. This leads to a shift of valence electron binding energy and possibility to open the autoionization channel [48].

In this chapter, autoionization channel in molecular systems were studied with a pump-probe method. Using the experimental setup introduced in chapter 3, measurements of two molecular systems, O_2 and CO, are demonstrated. We chose these particular molecules for the following reasons:

(1) High-resolution COLTRIMS measurements of these molecules using synchrotron radiation (data were taken from the Advanced Light Source (ALS) at Lawrence Berkeley National Laboratory (LBNL)) are available through collaborations with groups from LBNL. Deeper insight of the physical process can be gained by combining the high-resolution synchrotron work with our pump-probe studies.

(2) It is known from previous pioneering work that autoionization is a common phenomenon observed during the fragmentation of an oxygen-bearing diatomic molecule. The cation states populated via the photoionization can dissociate into a charged ion plus autoionizing atomic oxygen atoms, which will eventually lead to the population of dication states and ion pairs can be observed. It makes sense to start from these well-studied examples and to uncover their dynamic information.

Our findings from these studies are reported in the following two papers (see section 4.2 and 4.3).

4.2 Oxygen molecules: O_2

"Dynamic modification of the fragmentation of autoionizing states of O_2^+"

W. Cao, G. Laurent, S. De, M. Schöffler, T. Jahnke, A. Alnaser, I. A. Bocharova, C. Stuck, D. Ray, M. F. Kling, I. Ben-Itzhak, Th. Weber, A. L. Landers, A. Belkacem, R. Dörner, A. E. Ore, T. N. Rescigno and C. L. Cocke

Phys. Rev. A, **84**, 053406 (2011)

Dynamic modification of the fragmentation of autoionizing states of O_2^+

W. Cao,[1] G. Laurent,[1] S. De,[1] M. Schöffler,[2] T. Jahnke,[3] A. S. Alnaser,[4] I. A. Bocharova,[2] C. Stuck,[3] D. Ray,[1] M. F. Kling,[1] I. Ben-Itzhak,[1] Th. Weber,[2] A. L. Landers,[5] A. Belkacem,[2] R. Dörner,[3] A. E. Orel,[6] T. N. Rescigno,[2] and C. L. Cocke[1]

[1]*J. R. Macdonald Laboratory, Department of Physics, Kansas State University, Manhattan, Kansas 66506, USA*

[2]*Lawrence Berkeley National Laboratory, Chemical Sciences, Berkeley, California 94720, USA*

[3]*Institut für Kernphysik, University of Frankfurt, D-60438 Frankfurt, Germany*

[4]*Physics Department, American University of Sharjah, Sharjah, United Arab Emirates*

[5]*Department of Physics, Auburn University, Auburn, Alabama 36849, USA*

[6]*Department of Applied Science, University of California, Davis, California 95616, USA*

(Received 13 September 2011; published 10 November 2011)

The dynamic process of fragmentation of excited states of the molecular oxygen cation is investigated in a two-part study. First, using monochromatic 41.6 eV radiation and cold-target recoil-ion momentum spectroscopy detection of $O^+ + O^+$ ion pairs and associated electrons, we establish that this channel is populated only by an indirect process enabled by autoionization of excited oxygen atoms and identify the final active potential curves. Second, we probe the dynamics of this process using an attosecond pulse train of 35–42 eV EUV followed by an intense IR laser pulse. The results are compared with a model calculation.

DOI: 10.1103/PhysRevA.84.053406 PACS number(s): 34.50.Rk, 33.80.Rv, 42.65.Ky

I. INTRODUCTION

The tracking of the dynamics of wave-packet motion in small molecules using pump-probe timing, with infrared pump and infrared probe, is now a mature subject [1,2]. The use of EUV as the pump, a more recent development [3–7], has the advantage over the IR pump that the EUV can populate, via a single-photon process, a range of excited states of various ionization states of the molecule. When high-order-harmonic generation (HHG) is used to generate the EUV, the resulting radiation is in the form of a short attosecond pulse train (APT) [8–10], which can be made short enough (below 10 fs) to track vibrational motion even in light molecules. Such an APT still retains some spectral resolution, allowing the experimentalist some degree of control over the range of excitation generated by the pump.

In this work we fragment the oxygen molecule with an APT. It is well known that the fragmentation of any oxygen-bearing diatomic molecule can produce autoionizing excited states of neutral atomic oxygen fragments [11–14]. Since the autoionization usually occurs on a time scale longer than that for fragmentation, the population of cation states of the molecule which dissociate to a charged ion plus autoionizing atomic oxygen atoms ultimately results in the observation of ion pairs in the dication channel. One of the pioneering EUV-IR pump-probe experiments on molecular oxygen [4] explored the dynamics of this process, and argued that the autoionization of the molecule was not only interrupted by a delayed IR pulse, but that this pulse actively participated in the process by adding a photon of energy to the autoionization electron. Photoelectron spectra were interpreted to indicate that only when the spontaneous process became energetically allowed could this mechanism proceed. In this work we probe this system further by observing the kinetic-energy release (KER) in the $O^+ + O^+$ channel as a function of the delay between the EUV populating pulse and the IR probe pulse, and proposing a specific path to interpret the result. We observe a large increase in the KER when the IR probe arrives, which we interpret to mean that the evolution from a specific cation potential-energy curve (PEC) to a dication PEC is hastened by the arrival of the IR.

There have been numerous previous studies of the production of electron or ion pairs from the ionization of molecular oxygen. The high-resolution spectra and associated analysis by Lundquist *et al*. [15] of the KER of $O^+ + O^+$ pairs identified the major channels through which the dication breaks if the excitation level exceeds ∼40 eV (measured from the ground state of the neutral; see Fig. 1). This work has been the starting point for the interpretation of a number of experiments on KER spectra of the dication generated from a variety of excitation processes [4,16]. The important role of autoionizing channels populated by photoionization was first studied by Price *et al*. [12], as well as Hsieh *et al*. [13].

II. MONOENERGETIC BEAM SPECTRA

In order to be able to interpret KER spectra obtained with the broadband EUV from harmonic generation, we have first taken cold-target recoil-ion momentum spectroscopy (COLTRIMS) spectra with a monochromatic photon beam from the Advanced Light Source (ALS) at Lawrence Berkeley National Laboratory. The technique is described in detail elsewhere [17,18]. A monochromatic 41.6 eV EUV beam is directed onto a supersonic jet of molecular oxygen. The momenta of all ions and electrons emerging from the interaction region are recorded in coincidence for each event. At a photon energy of 41.6 eV one can make a direct double ionization to a dication state only for the $A^3\Sigma_u$ and $X^1\Sigma_g$ states (see Fig. 1). At the Franck-Condon (FC) distance of 2.27 a.u., population of the $X^1\Sigma_g$ is mainly to bound states, and population of the $A^3\Sigma_u$ state is barely possible. The major dissociating states of the dication start with the $W^3\Delta_u$ [13] and at 41.6 eV one cannot reach them. Thus there is essentially no direct dissociative double ionization of molecular oxygen at this photon energy. This is in contrast to the situation for CO, which we reported earlier [7].

Nevertheless, a strong yield of $O^+ + O^+$ ion pairs and electron pairs is observed. Figure 2 shows a density plot of the yield measured in the $O^+ + O^+ + e^- + e^-$ channel (four-particle coincidence). In Fig. 2(b), the energy of one

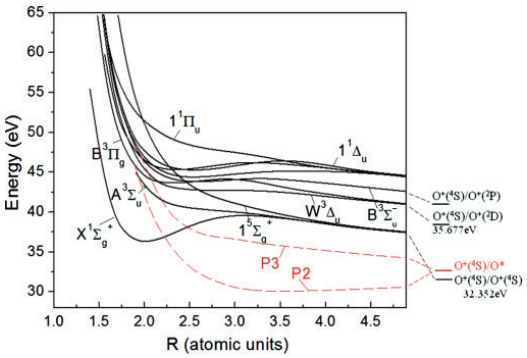

FIG. 1. (Color online) Partial energy-level diagram for the dication of O_2 (adapted from Ref. [15]). The red-dashed lines labeled as $P2$ and $P3$ indicate the calculated doubly excited cation states which can autoionize into the $O^+(^4S)/O^+(^4S)$ limit (see text).

electron (E_1) is plotted versus the energy of the other one (E_2). Since there is nearly no direct population of this channel, we identify all events as resulting from the production of a cation of O_2 which dissociates to $O^+ + O^*$, with the O^* then autoionizing after fragmentation to O^+ and an electron. Labeling, for the moment, the autoionization electron E_2 and the photoelectron E_1, the strong vertical stripes appearing near $E_2 = 0.4$, 0.7, and 1.6 eV are due to autoionization lines emitted from excited O neutrals after dissociation of the molecule has taken place. The value of E_1 along each line gives the spectrum of the associated photoelectron, and thus serves to identify the location of the initially populated PEC on which the dissociation of the cation occurs prior to autoionization. Of course, since we have no way to distinguish the autoionization electron from the photoelectron, the same features appear with E_1 and E_2 interchanged (symmetry about the diagonal). The spectrum of Fig. 2(b) is closely related to Fig. 2 of Ref. [11], and detailed identifications of the autoionization lines are given in that work.

In Fig. 2(a), the KER of the ion pair is plotted versus the sum energy of the two electrons. In such a plot, all events

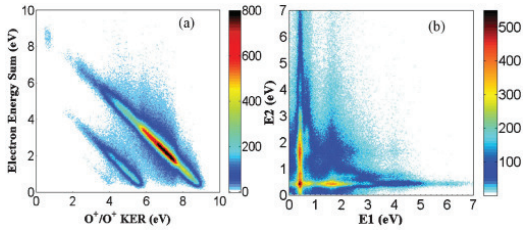

FIG. 2. (Color online) Correlation plots of the four-particle ($O^+ + O^+$ and the associated two electrons) coincidence experiment. (a) Density plot of the energy sum of the two electrons versus the $O^+ + O^+$ KER. (b) Density plot of the kinetic energy of the designated second electron (E_2) versus that of the first electron (E_1). The data were taken at the COLTRIMS station at the ALS with a photon energy of 41.6 eV.

leading to a particular final state of $O^+ + O^+$ are energetically constrained to a diagonal line. The energy difference between the photon energy and the four particles' sum energy will determine the final dissociation limit of the corresponding process. There are two diagonal lines in Fig. 2(a) which show that two autoionizing channels are involved. The higher energy line, the main one, corresponds to the $^4S/^4S$ final limit of $O^+ + O^+$ (32.352 eV). It is populated through an autoionizing state(s) of the cation $O^*(\ldots 2p^3[^2D]3p)/O^+(^4S)$ (and similar states; see Ref. [11]), which then decays to the $^4S/^4S$ limit. From the electron spectra of Fig. 2(a) we deduce that the energy of the autoionizing state(s) near the FC radius of 2.27 a.u. is near 39 eV, which produces the observed photoelectron energy E_1 near 1.8 eV. This corresponds to the $A1$ and $A2$ lines identified by Feifel *et al.* [11]. The lower energy line with a much weaker population corresponds to a final dissociation limit of ~35.6 eV, which can be identified as a final dication state correlated to the $O^+(^4S)/O^+(^2D)$ limit (see Fig. 1). This is similar to the $A3$ and $A4$ lines identified by Feifel *et al.* [11]. In fact, there is a wide range of E_1 along this line, suggesting that several PEC of the cation participate. The lack of any sharp features in E_1 also suggests that the participating PEC(s) are fairly steep in the FC region.

III. THEORETICAL CALCULATIONS

To support the interpretation of the measured data and better characterize the principal autoionizing excited state(s) of the cation involved, we carried out configuration-interaction (CI) calculations on the electronic states of O_2^+, with a view toward identifying inner-valence excited states that can be produced from ground-state ($^3\Sigma_g^-$) O_2 by absorption of a single EUV photon. A molecular orbital basis for the calculations was constructed by carrying out multiconfiguration self-consistent field calculations on the ground state of the dication with an augmented, correlation-consistent-polarized, valence triple-ζ basis on the oxygens. For the CI calculations, we kept the core oxygen $1s$ orbitals doubly occupied and included all single excitations from a multireference, complete active space (CAS) set of configurations using eight molecular orbitals (oxygen $2s$ and $2p$) in the active space.

The independent-particle (Koopmans') model generally breaks down for inner-valence singly charged ions, which are characterized by strong configuration mixing and numerous curve crossings. In the FC region, removal of an inner-valence electron—in this case from an O $2s$ ($2\sigma_g$ or $2\sigma_u$) orbital—produces a number of excited states with varying amounts of valence character. States in the energy range of interest (~39 eV in the FC region) here involve a $2\sigma_g$ vacancy. The calculations show two such states of symmetry, $^4\Sigma_g^-$ and $^2\Delta_g$, respectively, which lie just above the ground state of the dication in the FC region. The PECs for both states are shown in Fig. 1. The dominant valence configuration for both states is $(\ldots 2\sigma_g^{-1}\pi_g^2)$. As the internuclear separation is increased beyond 2.27 a.u., there are numerous crossings among the excited states and the two inner-valence states rapidly lose their valence character as they take on more Rydberg character. To arrive at the plotted curves, we examined the dominant CI coefficients as a function of R, allowing states to cross if there was little interaction, but following the adiabatic curve

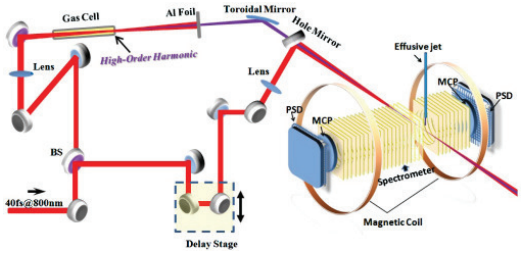

FIG. 3. (Color online) Schematic of the pump-probe experimental apparatus.

otherwise [14]. The ${}^4\Sigma_g{}^-$ and ${}^2\Delta_g$ states cross the O_2^{2+} ground state near $R = 66$ a.u. and can then autoionize. It is likely that the ${}^4\Sigma_g{}^-$ and ${}^2\Delta_g$ inner-valence states correspond to the "$P2$" and "$P3$" states observed by Feifel *et al*. [11], with the higher-energy $P3$ state most likely providing the dominant indirect ionization route observed in the COLTRIMS spectra. We note that, according to the observations of Feifel *et al*., the $P3$ state feeds both the $A1$ ($\ldots 2p^3[^2D]3p$, ^3D) and "$A2$" O^* autoionizing states near 0.4 and 0.5 eV, respectively. The data of Fig. 2(b) suggests that the $A1$ channel is dominant. The pump-probe data described below confirms this assignment.

IV. PUMP-PROBE EXPERIMENT

Armed with an understanding of the origin of $O^+ + O^+$ pairs from irradiation of molecular oxygen in the 40-eV-and-below region of excitation, we now proceed to explore the dynamics of the fragmentation process. HHG was used to produce an APT of EUV light. Since the APT has a pulse train structure extending over a shorter time (we estimate 10–20 fs here) than the pulse duration of the driving laser field, a time-resolved experiment can be conducted to explore the dynamic process of fragmentation on the time scale of the probe pulse. Figure 3 shows the schematic of our pump-probe experimental setup. An 800 nm Ti:sapphire laser pulse with a repetition rate of 1 kHz and a pulse duration of 40 fs was delivered to the EUV-IR interferometer. Part of the IR beam was focused into a semi-infinite gas cell containing 30 torr of argon gas to generate high harmonics serving as the EUV pump. A 200 nm aluminum foil was placed after the gas cell to eliminate the residual IR beam. The EUV beam was then focused to the target jet of a COLTRIMS system [17,18] by a toroidal reflector. The usual COLTRIMS supersonic jet was replaced by a diffusive jet to raise the target density. Another portion of the IR pulse was reflected by the beam splitter (BS) before the harmonic generation and recombined with the EUV, after an appropriate and adjustable delay, to provide the probe beam. The focused intensity of the probe was below 10^{12} W/cm^2. We deduced the harmonic content of the APT using the photoelectron spectrum it generated from an Ar target. The photon energy is the sum of the observed photoelectron energy and the 15.76 eV first ionization potential of Ar. Figure 4 shows the measured photoelectron spectrum from Ar, which reveals radiation mainly from the 21st (32.5 eV) through 27th (41.9 eV) harmonics, with dominance by the 25th (38.8 eV).

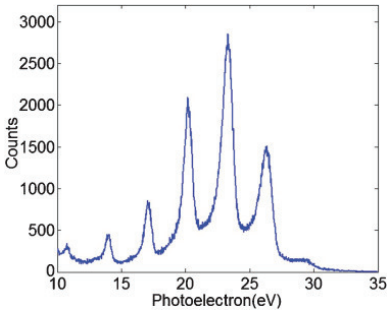

FIG. 4. (Color online) Photoelectron spectrum from EUV interaction with an argon target.

In Fig. 5 we show the KER in the $O^+ + O^+$ channel as a function of the pump-probe delay. At negative delay, when IR comes before XUV, a single broad peak near a KER of 6.8 eV is seen. This spectrum is the same as was obtained with no IR. Such a KER would result from states of the cation lying, in the FC region, near an excitation of 39 eV. Similar to the data of Fig. 2(a), this channel could be identified as due to the following process: $O_2 + h\nu \rightarrow O^+/O^* + e^- \rightarrow O^+(^4S)/O^+(^4S) + e^- + e^-$.

The fragmentation takes place first in an autoionizing excited state of the cation, hereafter referred to as AIC. The energetic properties of this state are known in the FC region, where it must be near 39 eV from Fig. 2(a), and at large internuclear distances where it must lie at 32.75 eV. The calculated AIC $P3$ described in the previous section and shown in Fig. 1 as a dashed red line has these properties. The AIC $P2$, also calculated and shown in Fig. 1, has too low an energy in the FC region to match the experimental data.

When the IR pulse arrives, the experimental KER is seen to increase abruptly to >10 eV. This increase then decays slowly with a lifetime near 250 fs. We interpret this to result from the removal of the most loosely bound electron from the AIC state, resulting in the population of a dissociative dication state.

For positive delays, the total KER will be the summation of the kinetic energy accumulated on AIC before the IR

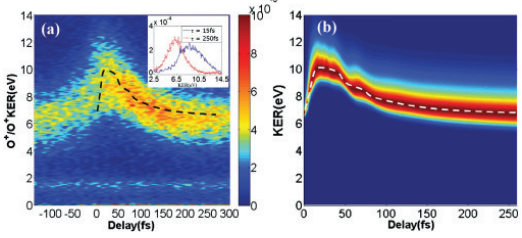

FIG. 5. (Color online) (a) Experimental density plot of KER versus delay of IR pulse with respect to the EUV pulse. Inset shows the projections of the spectra at different delays. (b) Calculated density plot of KER versus delay for the AIC $P3$. The dashed line shows the centroid of the calculated plot and is used to compare with the experimental data in panel (a).

pulse arrives and the kinetic energy accumulated on the dication curve after the IR pulse arrives. For large internuclear distances, both the AIC and dication curves are well known. The lack of Coulomb repulsion in the AIC state leads to a nearly flat potential curve, while the dication curve retains a repulsive Coulomb tail. Thus we expect to see an increase in the $O^+ + O^+$ KER coming from the extra Coulomb energy of the ion pair. The larger the delay, the larger the internuclear distance the AIC wave packet can reach prior to ionization and the smaller the KER increase.

We model the KER versus delay curve quantitatively. As indicated above, outside the FC region, the AIC states are well described as dication core states with a loosely bound $3s$ or $3p$ electron added. The dication core state of the AIC should be one which fragments to the $O^+ + O^+ {}^4S/{}^2D$ state, so as to provide the core energy necessary for ultimate autoionization for the uninterrupted fragmentation. We assume an initial population by the APT of a wave packet on the $P3$ AIC potential curve shown in Fig. 1. The shape of this packet is that of the lowest vibrational state of the neutral oxygen molecule. Using a numerical solution to the one-dimensional time-dependent Schrödinger equation, we allow this wave packet to propagate on the $P3$ AIC until the IR probe pulse arrives. At this point, the wave packet is assumed to be promoted to the dication core state, from which it completes its fragmentation. The KER is calculated from the asymptotic form of the final wave packet. Although many dication states could participate, in reality we choose the $W^3\Delta_u$ PEC from the ${}^4S/{}^2D$ manifold, the lowest-lying state with the correct asymptote, as the final dication state. The resulting plot of KER versus delay is shown in Fig. 5(b). While there is some fine structure in the plot for delays less than 50 fs, the 40 fs pulse duration of the probe pulse does not allow us to resolve this structure experimentally. The centroid of the calculated KER is shown as a light dashed line in Fig. 5(b). The same line is shown as a heavy dashed line superimposed on the data of Fig. 5(a). In this simulation, the abrupt increase on the KER for short delays is caused by the fact that the AIC $P3$ is much steeper than the $W^3\Delta_u$ PEC for small internuclear distance ($R < 3.0$). It is then followed by a slow KER decreasing over 250 fs corresponding to a large internuclear behavior as discussed before. The qualitative agreement shown between calculation and experiment suggests the validity of the assumption of the participating curves and supports the interpretation of the dynamics of this process. We have also modeled the KER versus delay using the $P2$ curve in Fig. 1 and found that it gives a rather poor match to the experimental data, with peak KER values at short delays much larger than that observed and smaller KER values at long delay times.

Although the main feature of the O_2 dynamic study results from the dissociation through the ${}^4S/{}^2D$ asymptote as discussed above, other dissociation limits can also be involved due to the coupling between different electronic curves at the crossing point in the presence of the laser field. The inset in Fig. 5(a) shows the KER spectra at two different delays (15 and 250 fs). When the IR pulse comes slightly after the XUV pulse, the KER spectrum goes up to 11 eV with a bandwidth of 5.2 eV, while for a large delay (250 fs), the bandwidth of the KER is only 3.6 eV. This can be qualitatively explained by considering the coupling between different dication states. The initially populated wave packet on the AIC state is moving outward. At $R \sim 2.6$ a.u. (corresponding to a delay $\sim$13 fs), the $1\,{}^5\Sigma_g{}^+$ and $W^3\Delta_g$ dication curves cross. If the IR pulse arrives at this delay, it can do two things. First, the IR pulse can promote the system onto the $W^3\Delta_g$ dication state; second, the IR pulse can open up the crossing point of $1\,{}^5\Sigma_g{}^+$ and $W\,{}^3\Delta_g$ states so that the $O_2{}^{2+}$ can dissociate via the $1\,{}^5\Sigma_g{}^+$ curve and reach the ${}^4S/{}^4S$ limit instead of the ${}^4S/{}^2D$ limit. Therefore, higher KER and broader spectrum will be expected. For large delays, where the internuclear distance is well beyond the crossing point of the $1\,{}^5\Sigma_g{}^+$ and $W^3\Delta_g$ states, no coupling is involved and the $O_2{}^{2+}$ can only dissociate into the ${}^4S/{}^2D$ limit, which gives a relatively narrower KER bandwidth.

V. SUMMARY AND CONCLUSION

In conclusion, we have studied the dynamic process of the fragmentation of an autoionization cation state(s) in oxygen molecules. The study involves two parts. First, a 41.6 eV monochromatic photon beam from the ALS was used to ascertain that, for photon energies below 41 eV, the yield of $O^+ + O^+$ ion pairs from single-photon absorption is dominated by an indirect process, namely, fragmentation of a molecular state of the cation followed by autoionization of the neutral fragment. The dominant such state is found to have energy near 39 eV in the FC region, and near 32.8 eV at large internuclear distances. Theoretical calculations identify this state as a $^2\Delta_g$ molecular cation ($P3$ in Fig. 1) having a predominantly $2\sigma_g{}^{-1}$ character in the FC region and correlating with $O^+({}^4S)/O^*(3p'[{}^3D])$ at large internuclear separation. Second, the dynamics of the fragmentation of this state was investigated in a pump-probe experiment. The fragmentation process was interrupted by a short IR pulse, which served to remove the most loosely bound electron from the cation state, producing a dissociating dication state which asymptotically reaches the $O^+({}^4S)/O^+({}^2D)$ limit. The experimental observation was that the kinetic-energy release of the ion pair was increased substantially by the arrival of the IR pulse, by an amount which decayed slowly as a function of delay between APT and IR pulses. Using the autoionizing cation state obtained from CI calculations and reasonable assumptions concerning the form of the dication state involved, a model for the fragmentation process was evaluated which showed good agreement with the experiment. The behavior of this process is very similar to one reported earlier by us for CO, except that in this case *only* the indirect autoinizing route to production of fragments from the dication is possible. It is becoming increasingly clear in EUV(pump)-IR(probe) experiments, that the general situation found here is a recurrent theme. The main effect of the IR probe is to remove loosely bound electrons from excited states of cation (or higher charged) molecules created by the EUV, thereby boosting the system to the next higher charge state and enhancing the KER of the fragments.

ACKNOWLEDGMENTS

This work was supported by Chemical Sciences, Geosciences and Biosciences Division, Office of Basic Energy Sciences, Office of Science, U.S. Department of Energy. W.C.

was supported by the National Science Foundation under Grant No. CHE-0822646. G.L. was supported by the US Army Research Office under Grant No. W911NF-07-1-0475. M.F.K. was partially supported by the German Science Foundation via the Emmy-Noether program and the Cluster of Excellence: Munich Center for Advanced Photonics. M.S. gratefully acknowledges support by the Alexander von Humboldt foundation.

[1] Th. Ergler, A. Rudenko, B. Feuerstein, K. Zrost, C. D. Schröter, R. Moshammer, and J. Ullrich, Phys. Rev. Lett. **95**, 093001(2005).
[2] A. S. Alnaser *et al*., Phys. Rev. A **72**, 030702(R) (2005).
[3] E. Gagnon, P. Ranitovic, X. M. Tong, C. L. Cocke, M. M. Murnane, H. C. Kapteyn, and A. S. Sandhu, Science **317**, 1374 (2007).
[4] A. S. Sandhu, E. Gagnon, R. Santra, V. Sharma, W. Li, Ph. Ho, P. Ranitovic, C. L. Cocke, M. M. Murnane, and H. C. Kapteyn, Science **322**, 1081 (2008).
[5] I. Thomann, R. Lock, V. Sharma, E. Gagnon, S. T. Pratt, H. C. Kapteyn, M. M. Murnane, and W. Li, J. Phys. Chem. **112**, 9382 (2008).
[6] J. M. Glownia *et al*., Opt. Express **18**, 17620 (2010).
[7] W. Cao *et al*., Phys. Rev. A **82**, 043410 (2010).
[8] P. M. Paul, E. S. Toma, P. Breger, G. Mullot, F. Augé, Ph. Balcou, H. G. Muller, and P. Agostini, Science **292**, 1689 (2001).
[9] P. Antoine, A. L'Huillier, and M. Lewenstein, Phys. Rev. Lett. **77**, 1234 (1996).
[10] Y. Mairesse *et al*., Science **28**, 1540 (2003).
[11] R. Feifel, J. H. D. Eland, and Edvardsson, J. Chem. Phys. **122**, 144308 (2005).
[12] S. D. Price and J. H. D. Eland, J. Phys. B **24**, 4379 (1991).
[13] S. Hsieh and J. H. D. Eland, J. Phys. B **29**, 5795 (1996).
[14] T. Osipov *et al*., Phys. Rev. A **81**, 011402 (2010).
[15] M. Lundqvist, D. Edvardsson, P. Baltzer, M. Larsson, and B. Wannberg, J. Phys. B **29**, 499 (1996).
[16] A. S. Alnaser, S. Voss, X. M. Tong, C. M. Maharjan, P. Ranitovic, B. Ulrich, T. Osipov, B. Shan, Z. Chang, and C. L. Cocke, Phys. Rev. Lett. **93**,113003 (2004).
[17] J. Ullrich, R. Moshammer, R. Dörner, O. Jagutzki, V. Mergel, H. Schmidt-Böcking, and L. Spielberger, J. Phys. B **30**, 2917 (1997).
[18] R. Dörner, V. Mergel, O. Jagutzki, L. Spielberger, J. Ullrich, R. Moshammer, and H. Schmidt-Böcking, Phys. Rep. **330**, 95 (2000).

4.3 Carbon monoxide: CO

"Dynamic modification of the fragmentation of CO^{q+} excited states generated with high-order harmonics"

W. Cao, S. De., K. P. Singh, S. Chen, M. Schöffler, A.S. Alnaser, I. A. Bocharova, G. Laurent, D. Ray, S. Zherebtsov, M. F. Kling, I. Ben-Itzhak, I. V. Litvinyuk, A. Belkacem, T. Osipov, T. Rescigno and C. L. Cocke

Phys. Rev. A, **82**, 043410 (2010)

Dynamic modification of the fragmentation of CO^{q+} excited states generated with high-order harmonics

W. Cao,[1] S. De,[1] K. P. Singh,[1] S. Chen,[1] M. S. Schöffler,[3] A. S. Alnaser,[4] I. A. Bocharova,[1,3] G. Laurent,[1] D. Ray,[1] S. Zherebtsov,[2] M. F. Kling,[1,2] I. Ben-Itzhak,[1] I. V. Litvinyuk,[1,5] A. Belkacem,[3] T. Osipov,[3] T. Rescigno,[3] and C. L. Cocke[1]

[1]*J. R. Macdonald Laboratory, Physics Department, Kansas State University, Manhattan, Kansas, 66506, USA*
[2]*Max-Planck Institute of Quantum Optics, Hans-Kopfermann-Strasse 1, D-85748, Garching, Germany*
[3]*Lawrence Berkeley National Laboratory, Berkeley, California 94720, USA*
[4]*Physics Department, American University of Sharjah, Sharjah, UAE*
[5]*Centre for Quantum Dynamics, Griffith University, Nathan, Queensland 4111, Australia*

(Received 15 May 2010; published 8 October 2010)

The dynamic process of fragmentation of CO^{q+} excited states is investigated using a pump-probe approach. EUV radiation (32–48 eV) generated by high-order harmonics was used to ionize and excite CO molecules and a time-delayed infrared (IR) pulse (800 nm) was used to influence the evolution of the dissociating multichannel wave packet. Two groups of states, separable experimentally by their kinetic-energy release (KER), are populated by the EUV and lead to C^+-O^+ fragmentation: direct double ionization of the neutral molecule and fragmentation of the cation leading to C^+-O^*, followed by autoionization of O^*. The IR pulse was found to modify the KER of the latter group in a delay-dependent way which is explained with a model calculation.

DOI: 10.1103/PhysRevA.82.043410 PACS number(s): 34.50.Rk, 33.80.Rv, 42.65.Ky

I. INTRODUCTION

The real-time probing of wave-packet dynamics in small diatomic molecules with infrared pulses is a mature subject, having now been practiced over nearly two decades [1]. The use of extreme ultraviolet (EUV: 20–100 eV) pump pulses with infrared probe pulses is a much more recent development. The importance of the EUV pump is that it can, in a single-photon process and at a well-defined time, excite and ionize the target to a high level of excitation while maintaining, within the limits of the uncertainty principle, spectral control over the degree of excitation or ionization. Short EUV bursts pump radiation from harmonic generation have been used in several cases to populate excited or ionized states of light diatomic molecules whose subsequent fragmentation can be followed or influenced by a short infrared (IR) probe [2–5]. It is typically the case that the spectral resolution of the EUV burst is inferior to that which can be obtained with, for example, a synchrotron radiation source. It is thus profitable to combine high-resolution synchrotron work with pump-probe studies of the dynamics, exploiting the advantage of each to deepen our understanding of the fragmentation process.

The ion kinetic energy release of doubly charged carbon monoxide has been studied extensively [6–10], and vibrationally resolved measurement [6–8] and multiple pathways of C^+-O^+ fragmentation [9,10] have been reported. In a recent study of the fragmentation of CO, Osipov *et al.* [11] reported high-resolution COLTRIMS measurements of C^+-O^+ fragments produced by ionizing neutral CO with 43-eV photons from the Advanced Light Source (ALS). They were able to identify two main decay paths to this final channel (see Fig. 1): (a) a direct path from the population of dissociating states of the dication of CO at an energy above that necessary to surpass a predissociation crossing and/or well barrier (approximately 42 eV) and (b) an indirect path from the population of highly excited states of the cation of CO which dissociate to a C^+ ion and a highly excited O^* fragment. The excited oxygen atom then autoionizes after dissociation has taken place. With the help of model calculations they were able to identify at least two inner-valence states of the cation which could contribute to this latter process. In this paper we probe the time dependence of this fragmentation process by using an IR pulse applied during the fragmentation to alter the decay route. In principle, such a pulse could modify both the direct and indirect processes, but we conclude on the basis of our experimental results that the major effect is on the indirect pathway.

II. RESULTS AND DISCUSSION

As preparation for the time-dependent measurements, we first look at a COLTRIMS [13,14] spectrum in the C^+-O^+ fragmentation channel, taken with a monoenergetic photon beam. Figure 2 shows the kinetic-energy release (KER) in the C^+-O^+ channel plotted versus the sum energy of the two electrons ejected by the EUV photon. This figure is very similar to Fig. 1 of Ref. [11], except that the photon energy is 47 eV, appropriate for our experiment, instead of the 43 eV of the synchrotron work. Energy conservation requires that, for a given dissociation limit for the C^+ and O^+, the events lie on a single diagonal line. Figure 2 shows (as does Fig. 1 of Ref. [11]) that the production of the ground states of the separated ions, with an asymptotic energy of 35.8 eV, dominates. There is also a weak diagonal line below the dominant one which corresponds to events feeding the excited state C^+-O^{+*} with a probability of a few percent. The weak vertical line around the sum electron energy of 5 eV is due to random events. Thus we are entitled to assume that the ground state is the only active fragmentation channel over this range of photon energies. This greatly simplifies our task when doing the time-resolved experiment, since it shows that the KER provides the same information as would the sum energy of the two electrons. In our EUV + IR experiment, we measure only

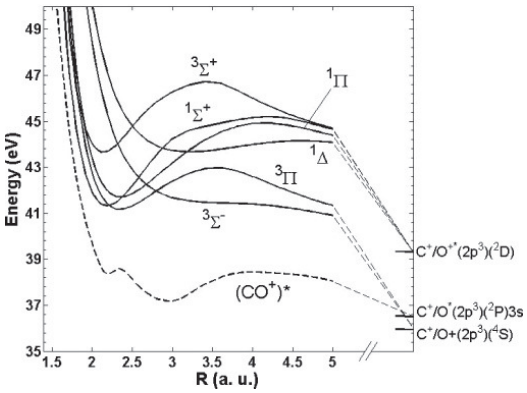

FIG. 1. Partial energy level diagram for the dication of CO (adapted from Refs. [11] and [12]). The solid lines are dication potential energy curves. The dashed line is one of the curves calculated in Ref. [11] for the cation decay, populating an autoionizing state of the oxygen neutral. Zero energy is taken to be the bottom of the neutral ground-state potential curve, which has a minimum near 2.14 a.u. (Franck-Condon region).

the momenta of the C^+ and O^+ ions (and not the electrons) in order to determine the energetics of the fragmentation.

Figure 2 shows two major groups along the energy conservation line. The higher KER one, beginning roughly at a KER of 6 eV, is due to the direct population of dication states in the Franck-Condon region. The population of vibrational states of the $^3\Pi$ ground state of the dication with energies near and above the predissociation crossing of the $^3\Pi$ curve with the $^3\Sigma^-$ curve leads to direct fragmentation into the C^+-O^+ channel. Because of the necessity that this energy surpasses

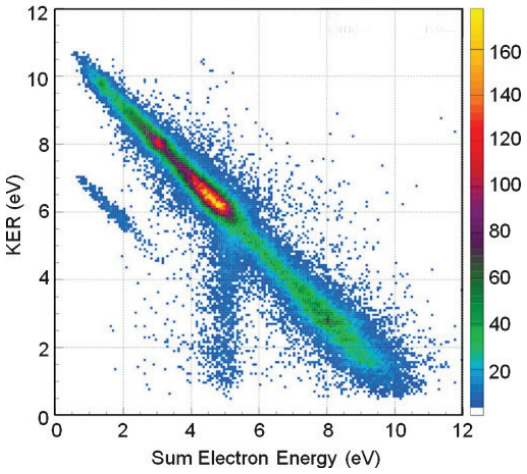

FIG. 2. (Color online) Density plot of KER in the C^+-O^+ channel versus the sum energy of the two electrons. The data were taken at the COLTRIMS station at the ALS at photon energy of 47 eV. (See Osipov *et al.* [11].)

approximately 41.6 eV, the predissociation crossing, the KER from this process will lie mainly above 5.8 eV. Furthermore, population of higher states of the dication can also lead to fragmentation to the same final channel with KER above, but not below, 5.8 eV. The second group with KER peaking near 3 eV is due to the production of excited states of the cation, as discussed in Ref. [11]. These states dissociate to the ground state of C^+ plus a core-excited state of O^* [3,15–17]. For example, a state of the configuration $[\ldots(2p)^3(^2P)3s]$ is one such state [10]. The O^* then autoionizes after the fragmentation has taken place. In fact, many autoionizing states of O which can participate in this process are known [15–17]. The lifetime of this autoionization process is not known precisely, but it is expected to be in the picosecond range or longer [15], longer than the dissociation time.

The time-dependent experiment, the main subject of this paper, addresses the following question: Can one modify the fragmentation process by the application of a short IR pulse during the fragmentation process? One might expect that such an IR pulse could modify the behavior of the wave packet of the dication at the predissociation crossing for the direct process. One might similarly expect that the IR pulse could modify the indirect wave packet in the cation by possibly removing an electron from this highly excited molecule.

A schematic of the experimental setup for the time-dependent measurement is shown in Fig. 3. A 10-fs, 1-mJ pulse was generated by passing a 35-fs pulse of 800-nm radiation through a spectrum-broadening capillary-containing Ne gas, followed by chirped mirrors. The EUV pulses were generated by focusing the 10-fs pulse into a gas cell containing 20 Torr of Ar gas. The resulting harmonic spectrum spans from the 21st to the 31st harmonics (32–48 eV), as measured both with an EUV spectrometer and from the photoelectron spectrum of He. The spectrum is centered at the 25th harmonic (38.9 eV) with a full width at half maximum of about 7 eV. The harmonics were recombined with a fraction of the infrared beam using a recombination mirror and both beams were focused onto a diffusive jet located in the center of a COLTRIMS spectrometer [13,14]. Ions resulting from the fragmentation of the CO^{q+} molecule were projected by a uniform electric field onto the

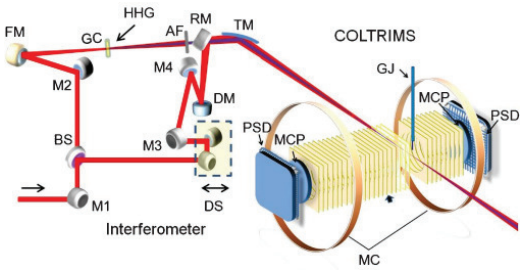

FIG. 3. (Color online) Schematic of the experimental apparatus used in the time-resolved study. M1-M4: plane mirror; BS: beam splitter; RM: recombination mirror; MCP: microchannel plate; FM: focusing mirror; GC: gas cell; DS: delay stage; PSD: position-sensitive detector; DM: diverging mirror; AF: Al filter; TM: toroidal mirror; MC: magnetic coils; GJ: effusive gas jet; HHG: high-order harmonic generator.

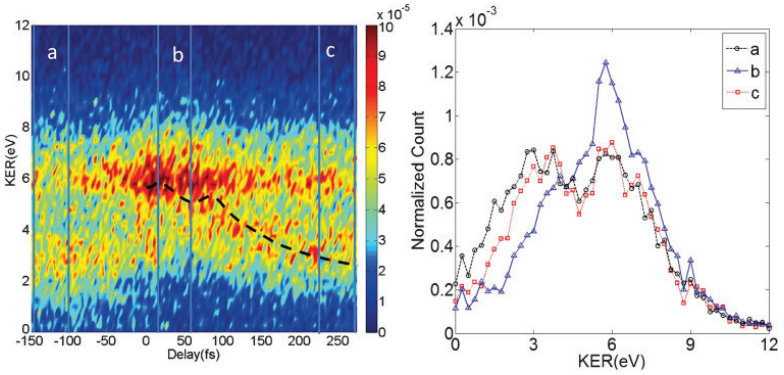

FIG. 4. (Color online) (Left) Density plot of KER versus delay of the IR pulse with respect to the EUV pulse. (Right) Projection of this spectrum onto the KER axis for delays indicated by a, b, and c in the left-hand panel.

surface of a time- and position-sensitive detector, and the initial momenta of the fragments were determined from the times and positions of arrival of the particles using classical equations of motion [13]. From the measured momenta of the C^+ and O^+ ions it was first verified that the ions came from the same molecule, and then the KER was determined. Although the electron momenta were also measured in determining the harmonic content of the beam, they were not used in the present data analysis for CO fragmentation. The 1-kHz repetition rate of the laser was too low to allow us to do a four-particle coincidence experiment, as was done in generating Fig. 2. The delay of the IR pulse relative to the arrival of the EUV pulse was varied using a Mach-Zender interferometer. The intensity of the IR pulse was about 5×10^{12} W/cm^2.

The left-hand panel of Fig. 4 shows a density plot of KER versus EUV-IR delay. The determination of the time zero in this figure was made by removing the aluminum foil and observing the delay for which the interference pattern between IR pulses traveling on the pump and probe paths was optimized. A small correction was then made for the fact that the EUV burst arrives slightly earlier than the center of the driving IR pulse, since the EUV burst is generated on the rising edge of the IR pulse. This small shift (approximately 5 fs) was determined by measuring the sideband pattern generated by the EUV and IR pulses in the photoelectron spectrum of argon and comparing the time delay for which this peaked with the time delay observed in the IR interference pattern. We estimate a possible error of 5 fs on our determination of the time zero.

The right-hand panel of Fig. 4 shows the KER spectra taken for different windows on the delay of the IR pulse. If the IR pulse comes before the EUV pulset, the KER spectrum is the same as it is when no IR pulse is used at all. The KER spectrum for this case (a) shows two main peaks. Direct double ionization is responsible for the peak above 5.8 eV, while delayed double ionization gives the lower peak centered near 3 eV. (We note that the KER alone is sufficient to determine the energy deposited in the molecule in this case, although a range of photon energies and corresponding electron sum energies are involved for each KER. A monoenergetic photon is not necessary for the identification of the decay channel.) When the IR pulse is coincident with the EUV pulse (case b) the delayed double ionization peak is seen to move to much higher KER, now overlapping with the direct double ionization peak. This increase in KER from this channel then gradually decreases as the IR pulse comes later after the EUV pulse, finally returning nearly to the same spectrum as when the IR pulse comes first (case a).

Our interpretation of Fig. 4 is that the major effect of the IR pulse is on the autoionization channel, not the direct double ionization channel. The KER through the cation states is modified because the IR pulse can ionize them to form dications. An electron with a binding energy I_p is driven over-barrier at the peak field by an IR pulse with an intensity given by $I = (I_p/12.4)^{1/4}$, where I is in units of 10^{14} W/cm^2 and I_p is in electron volts. At a laser intensity of 10^{12} W/cm^2, electrons with binding energies below 3.9 eV are over-barrier at the peak of the electric field. Excited molecular states are quite fragile in modest IR fields. The gain in KER results from the conversion of the cation to the dication during the fragmentation, which adds a large Coulomb contribution to the dissociation energy if the conversion occurs early in the fragmentation.

To support this interpretation quantitatively, we have modeled this process using one of the two potential curves for the autoionizing cation given in Ref. [11]. A schematic of the process is shown in Fig. 5(a). The cation is assumed to be populated by the EUV with a vibrational wave function corresponding to the vibrational ground state of neutral CO. This wave function is allowed to propagate on the cation curve. After some delay (τ) the IR pulse is assumed to move the molecular ion onto a potential curve of the dication and the vibrational wave function is allowed to propagate on this potential curve. The KER accumulated over the entire process to large internuclear distance (R) is then evaluated. A plot of the resulting average KER versus τ is shown in Fig. 5(b). In calculating this result we have assumed that the wave packet is promoted to the $^3\Pi$ state of the dication for internuclear distances inside the predissociation crossing at 2.8 a.u., and to the $^3\Sigma^-$ state for larger internuclear distances. For about the first 90 fs, the wave packet is traveling on the complicated

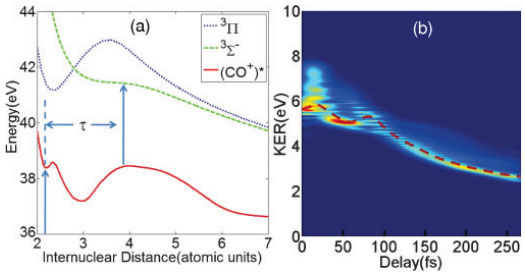

FIG. 5. (Color online) (a) Schematic of potential curves used in the model calculation. (b) Density plot of KER versus time delay τ. The dashed red line is drawn through the major population and used in Fig. 4 to compare this result with the experiment. See text for details.

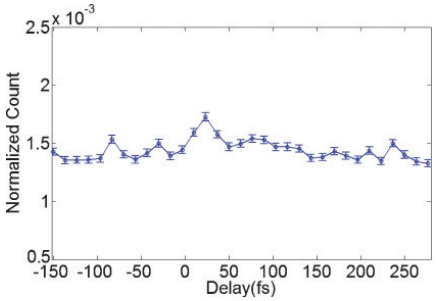

FIG. 6. (Color online) Total yield in the C^+-O^+ channel versus τ, normalized to the number of laser shots at each delay.

part of the potential curves inside an internuclear distance R of 6 a.u. Over this range of R, the difference between the cation and dication potentials is not yet decreasing monotonically as it does later. The calculated KER for times less than 90 fs is thus complex, but not yet systematically decreasing. For larger delays, the wave packet travels on the rapidly descending Coulomb part of the dication potential curve and the KER decreases monotonically with τ. This behavior is very similar to that observed in the experimental data of Fig. 4. The qualitative shape of the calculated curve is not very sensitive to the exact dication potential curve on which the final dissociation is assumed to occur. For example, using either the $^3\Pi$ or $^3\Sigma^-$ dication potential curve alone produces a similar result, as does the use of the other autoionizing cation curve given in Ref. [11]. In order to compare the model calculation with the data, we have drawn a smooth dashed curve through the model result in Fig. 5(b), and we show the same curve superimposed on the data of Fig. 4(a). It is seen that the model curve agrees well with the observation, supporting our interpretation of the influence of the IR pulse on the fragmentation of the ionized or excited CO molecule by the EUV pulse.

If the only role of the IR pulse were to promote the autoionizing state of the cation to the dication, one would expect that the total yield in the C^+-O^+ channel should not vary as a function of τ. In fact, a small increase of yield in the region where the IR and EUV pulses overlap is observed, as is shown in Fig. 6. It is possible that this increase could be caused by an enhancement of the predissociation crossing of the $^3\Pi$ and $^3\Sigma^-$ curves due to the IR pulse, which might enhance the direct double ionization channel. It should take the wave packet approximately 20 fs to reach this crossing, and thus such an effect should maximize not at $\tau = 0$ but nearer to $\tau = 20$ fs. The data are consistent with such an effect. Thus while the main effect of the IR pulse is certainly on the indirect double ionization channel, there is some weak evidence for enhancement of the direct channel as well.

III. CONCLUSION

In summary, we have found that the effect of applying a delayed IR pulse to a fragmenting CO molecule, following excitation and ionization by a 32–48 eV EUV pulse, is primarily to convert the autoionizing path discussed by Osipov *et al.* [11] into a direct double ionization path. This finding is very much in accord with two previous experiments on the EUV-IR pump-probe investigations of the dynamics of fragmentation in light molecules [2,3]. Whereas ground-state molecules and molecular ions are rather immune to the application of weak IR pulses, excited states with loosely bound electrons are not. Since EUV ionization usually populates a wide range of excited states, ionization by the IR pulse is readily enabled by this process. The dominant fragmentation pathways then become very sensitive to being guided by the IR pulse. It is likely that this general situation will reign in most EUV-IR pump-probe experiments, including those in which the branching ratios of final products are modified by the presence of a delayed IR field.

ACKNOWLEDGMENTS

This work was supported by Chemical Sciences, Geosciences and Biosciences Division, Office of Basic Energy Sciences, Office of Science, U.S. Department of Energy, by the National Science Foundation under Grant No. CHE-0822646, by the U.S. Army Research Office under Grant No. W911NF-07–1-0475, and by the German Science Foundation via the Emmy-Noether program and the Cluster of Excellence: Munich Center for Advanced Photonics.

[1] A. H. Zewail, Science **242**, 1645 (1988).
[2] E. Gagnon *et al.*, Science **317**, 1374 (2007).
[3] A. S. Sandhu *et al.*, Science **322**, 1081 (2008).
[4] G. Sansone *et al.*, Nature (London) **465**, 763 (2010).
[5] F. Kelkensberg *et al.*, Phys. Rev. Lett. **103**, 123005 (2009).
[6] M. Lundqvist, P. Baltzer, D. Edvardsson, L. Karlsson, and B. Wannberg, Phys. Rev. Lett. **75**, 1058 (1995).
[7] F. Penent, R. I. Hall, R. Panajotovic, J. H. D. Eland, G. Chaplier, and P. Lablanquie, Phys. Rev. Lett. **81**, 3619 (1998).
[8] J. H. D. Eland *et al.*, J. Phys. B **37**, 3197 (2004).
[9] P. Lablanquie *et al.*, Phys. Rev. A **40**, 5673 (1989).

[10] U. Becker, O. Hemmers, B. Langer, A. Menzel, R. Wehlitz, and W. B. Peatman, Phys. Rev. A **45**, R1295 (1992).
[11] T. Osipov *et al.*, Phys. Rev. A **81**, 011402 (2010).
[12] T. Sedivcova *et al.*, J. Chem. Phys. **124**, 214303 (2006); T. Sedivocova-Uhlicova *et al.*, Int. J. Quantum Chem. **107**, 2654 (2007).
[13] J. Ullrich *et al.*, Rep. Prog. Phys. **66**, 1463 (2003); R. Doerner *et al.*, Phys. Rep. **330**, 95 (2000).
[14] S. Voss *et al.*, J. Phys. B **37**, 4239 (2004).
[15] R. Feifel *et al.*, J. Chem. Phys. **122**, 144308 (2005).
[16] S. Hsieh *et al.*, J. Phys. B **29**, 5795 (1996).
[17] S. D. Price *et al.*, J. Phys. B **24**, 4379 (1991).

Chapter 5

Pump-probe measurement of electron dynamics in high order harmonic generation

5.1 Introduction

In chapter 4 we demonstrated the first application of the EUV-IR pump-probe technique: dynamic studies of excited molecular cations with femtosecond resolution. The application is based on the fact that the EUV source can interact with inner shell electrons and activate a dynamic process in the molecule. Another unique property of the HHG-based EUV source is its highly coherent temporal structure [57, 58]. The regular phase relationship between different harmonics supports the formation of an attosecond pulse train (APT) [5]. By locking the APT to the carrier of an IR probe pulse sub-cycle information on the light-matter interaction is accessible. This effectively opens the door to the second application of the the EUV-IR pump-probe technique: measuring and controling the electron wave-packet, which possesses a characteristic time of sub-femtosecond. In this chapter, the electron dynamics in atoms will be explored. Specifically, the quantum trajectories of electrons related to the

bifurcated high harmonics is of interest. By measuring both the phase and amplitude of high harmonics with the RABBITT technique [5, 35], a deeper insight into the mechanism of the bizarre spectral splitting phenomenon is gained.

5.2 Experimental results

"Spectral Splitting and quantum path study of high harmonic generation from a semi-infinite gas cell"

Wei Cao, Guillaume Laurent, Cheng Jin, Hui Li, C.D Lin, I. Ben-Itzhak, C. L. Cocke

J. Phys. B: At. Mol. Opt. Phys. **45** (2012) 074013

IOP Publishing Journal of Physics B: Atomic, Molecular and Optical Physics

J. Phys. B: At. Mol. Opt. Phys. **45** (2012) 074013 (8pp) doi:10.1088/0953-4075/45/7/074013

Spectral splitting and quantum path study of high-harmonic generation from a semi-infinite gas cell

W Cao, G Laurent, Cheng Jin, H Li, Z Wang, C D Lin, I Ben-Itzhak and C L Cocke

J R Macdonald Laboratory, Kansas State University, Manhattan, KS 66506, USA

E-mail: caowei1688@gmail.com

Received 4 October 2011, in final form 24 November 2011
Published 16 March 2012
Online at stacks.iop.org/JPhysB/45/074013

Abstract

We have investigated the spectral splitting of high harmonics generated in a semi-infinite gas cell. By performing an EUV–IR cross-correlation experiment, we are able to use the phase behaviour of the different sub-peaks of each harmonic to identify them with different electronic trajectories. Both microscopic and macroscopic analyses of the spectra effects are made. The identification of a particular trajectory with a particular component of the splitting on the basis of a single-atom model is found to be incorrect, while the full macroscopic treatment is in agreement with the experiment.

(Some figures may appear in colour only in the online journal)

1. Introduction

When atoms and molecules are exposed to strong electromagnetic fields, electrons can be stripped partially. In a time scale of the order of several atomic units (∼24 as), the resulting electron wave packet can involve both continuum and bound electronic states. The coupling between the bound and free electrons in the presence of the strong field leads to numerous interesting physical phenomena such as multi-photon ionization, tunnelling ionization, sequential/non-sequential double ionization and high-harmonic generation (HHG). Among these, HHG has been studied extensively in the last decade due to its potential applications in attosecond science [1–3] and as a coherent EUV source [4, 5]. HHG has also been applied to molecular orbital tomography [6] and time-resolved studies of molecules [7].

The three-step model [8] conceptually describes the process of HHG from a classical point of view. Two well-known major quantum paths of the returning electron (short and long trajectories) have been identified in this intuitive classical picture. Many topics associated with these quantum paths have been raised since then. In order to control and optimize the attosecond pulse train (APT), it has often been expedient to eliminate, through quantum path control, one or the other of these paths. Macroscopically, this can be realized either by playing with the optical geometry [9, 10] or by using a spatial filter [11]. Microscopically, a bichromatic electric field has been used as an efficient tool to enhance one or the other path by controlling the timing of the ionization step [12–14]. On the other hand, if the study of the underlying formation of the HHG is the intent, information can be gained from the quantum path interference between the two components. In this case, the participation of both paths with similar amplitudes is preferable to obtain optimal contrast in the interference pattern [15, 16].

One phenomenon which can result from the participation of both paths is the spectral splitting of each harmonic into two components. This phenomenon has been studied and observed by several groups [17–21]. Wang *et al* [17] reported that intensities well above the saturation value for argon produced a spectral splitting and proposed that the cause was a propagation effect resulting in a splitting of the harmonic pulse envelope into two components accompanied by a related spectral splitting. Zhong *et al* [18] also reported the HHG splitting in the over-saturated intensity region. They did a similar 1D propagation of HHG and found that the plasma's induced distortion of the fundamental field played a key role in the splitting of HHG. Brunetti *et al* [19] reported the

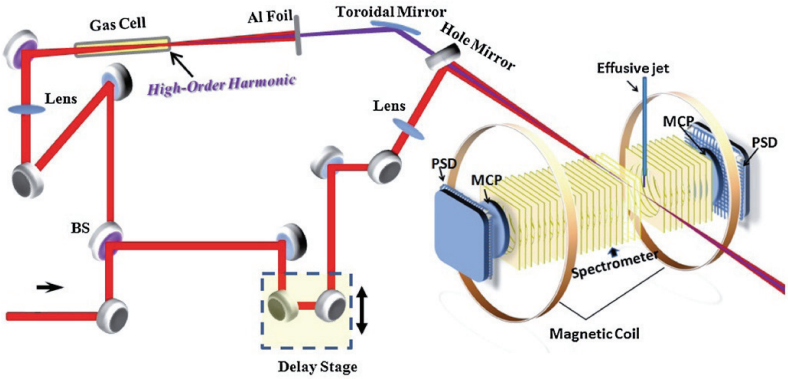

Figure 1. The schematic of the experimental setup.

substructure in each harmonic and attributed the splitting to properties of the single-atom response. Xu *et al* [20] observed a splitting of HHG generated at 1240 nm and attributed the structure to interference between short and long trajectories. He *et al* [21] observed the double and even triple peak structure in argon HHG, and interpreted this in terms of quantum path interference between short and long trajectories. They found that propagation effects enhanced the phase matching for the long trajectory making it of an intensity competitive with the short trajectory.

All previous measurements on the spectral splitting have been limited to intensity profiles. In order to gain deeper insight into the HHG process, it is necessary to know the phase as well as the intensity of each harmonic. In this paper, we provide such phase measurements. We do this by performing an EUV–IR cross-correlation experiment (RABBITT [22–25]). When the HHG are synchronized with a weak fundamental laser field and both fields interact with atoms, photoelectrons are produced via a two-photon process with energies sitting between those produced by adjacent harmonic photoelectrons (we will call these sideband photoelectrons hereafter). As can be explained from second-order perturbation theory, the sideband amplitude oscillates with EUV–IR delay with a periodicity of one half cycle of the fundamental field. The phase of the sideband oscillation corresponds to the first derivative of the phase of the HHG with respect to harmonic number, and thus a measurement of this oscillation yields experimental information on the phase of the HHG. In this paper, we use this phase information in addition to the spectra to investigate the physical processes which lead to the spectral splitting.

2. Experimental setup

The schematic of the experimental setup is shown in figure 1. The 2 mJ 50 fs laser beam generated from a commercial Ti:sapphire laser system is divided into two halves by a beam-splitter (BS). Part of the beam is focused by a 50 cm spherical lens into a gas cell filled with argon gas for HHG. A diaphragm is placed before the lens to control and adjust the laser beam diameter. We use a semi-infinite gas cell which is similar to that used in [25]. The cell is 30 cm long sealed with an AR-coated entrance window at one end and an exchangeable metal plate at the other end. The semi-infinite gas cell has the advantage over a gas jet that it has a higher conversion efficiency because of the increased focusing volume [26]. Another advantage is the improved stability of the spectrum due to the relatively stable gas flow in the interaction region. Since many parameters (gas pressure, focus position, beam diameter, etc) will affect the spectrum of HHG in order to systematically investigate the dependence of the spectrum on the location of the interaction region within the gas, we fix the gas pressure (30 Torr) and diaphragm at a position (0.8 cm in diameter) where reasonable flux is obtained, and then scan the focal position of the driving field along the direction of propagation of the laser. The peak intensity of the driving field is estimated to be no more than 6×10^{14} W cm^{-2} in vacuum. A 200 nm aluminum foil is used to block the IR beam after the gas cell. One meter downstream of the harmonic generation region, a toroidal reflector is applied at a grazing angle of 7° to deliver the EUV into the interaction region. The other part of the beam after the BS is passed through a piezoelectric transducer delay stage and recombines with the EUV beam via a hole mirror. The 2 mm hole is equivalent to a spatial filter for the EUV beam, limiting the angular spread of the HHG observed.

After recombination, the IR and EUV beams propagate collinearly and are focused onto the gas target located in the detection system. Photoelectrons from the interaction of the beams with the gas jet are detected by a position- and time-sensitive channel-plate detector, from which their energies are determined. Further details on the cold target recoil ion momentum spectroscopy (COLTRIMS) spectrometer are described in [27, 28]. For the present experiment, the COLTRIMS spectrometer was operated field free and only electrons were detected.

3. Experimental results

Figure 2 shows the photoelectron spectra of argon generated from HHG without IR. The photon energies of the EUV can

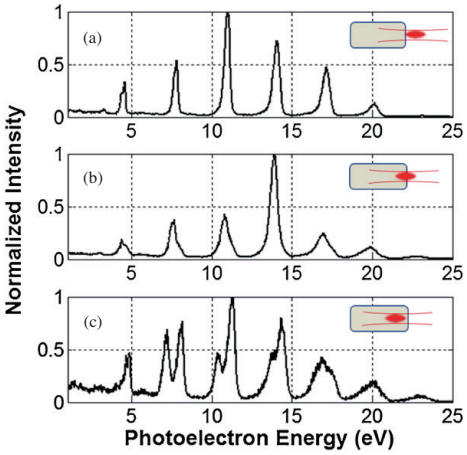

Figure 2. Experimental argon photoelectron spectra of harmonics generated with three different focusing geometries. The focal point is located (a) 3 mm after, (b) at and (c) 6.3 mm before the exit of the gas cell. The red dots indicate the focusing volume of the laser.

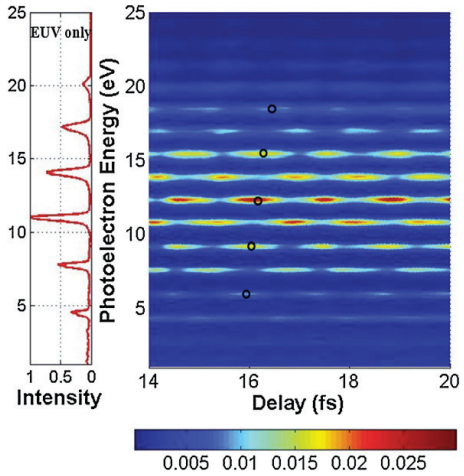

Figure 3. Left panel: the argon photoelectron spectrum when only the EUV is present. Right panel: the argon photoelectron spectrum versus EUV–IR delay. For specific delay, the spectrum has been normalized to the laser shots. The HHG were generated under the condition of figure 2(a) (focus beyond gas cell, case I) except that the IR was added. The black open circles indicate the positions of the maxima in the sideband oscillations.

be obtained from the photoelectron energy by adding the first ionization potential of argon (15.76 eV) to the photoelectron energy. When the driving pulse is focused outside the gas cell (3 mm beyond the exit aperture, case I), clean and sharp HHG peaks are observed indicating that a single quantum path (short trajectory) has been selected [29]. When we move the focal point to coincide with the exit aperture of the gas cell (case II), the HHG peaks start to get broader. When the focal point is located before the cell exit (6.3 mm before the exit aperture, case III), a clear double-peak structure is observed for each harmonic. This observation is consistent with the results from [17] and [19], which means that this could be a general and universal phenomenon in harmonics.

When the IR is present, the photoelectron spectrum develops sidebands which oscillate in intensity as the delay between the IR and EUV is varied. The phase of this oscillation can be used to extract the relative phases of the harmonics which are adjacent to each sideband using the well-established RABBITT technique [22–25]. Figure 3 shows a RABBITT scan corresponding to case I with the focus beyond the gas cell. No splitting of the HHG is observed for this case, and the oscillation maxima of the sidebands lie on a nearly straight line with a small positive slope. As discussed in [24], this slope is the characteristic of the HHG chirp expected for short trajectories.

Figure 4 shows the corresponding RABBITT scan for case III, for which strong spectral splitting is observed. The spectrum is somewhat busy due to the presence of sidebands from both the blue (higher energy) and red (lower energy) sub-peaks of each split harmonic. The expected locations of the sidebands from each component are indicated in the figure. It is immediately clear that the oscillation maxima of the blue and red sidebands line up along quite different straight lines, indicating that the chirps of the two components are quite different in both sign and size. The blue component has a small

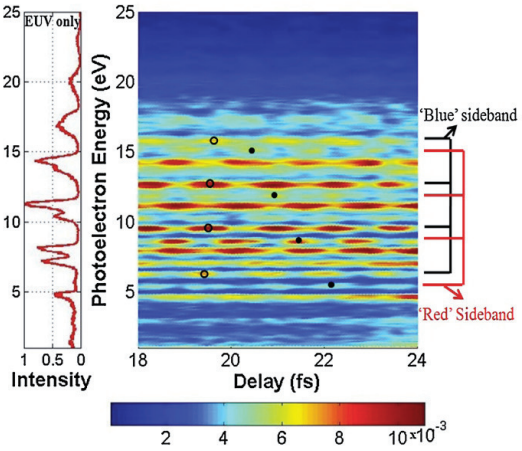

Figure 4. The same as figure 3 except that the harmonics are generated under the conditions of figure 2(c) (focus inside the gas cell, case III). The black open circles and black dots indicate the maxima of the oscillations of the two sideband groups located between each pair of HHG.

positive slope similar to that seen for case I and consistent with that expected for short trajectories. The red component has a large negative chirp, of the sign expected for long trajectories.

In the usual RABBITT analysis, the IR pulse is restricted at low intensities so that second-order perturbation theory can be used to analyse the spectrum. In figures 3 and 4, the amplitude of the sideband peaks is comparable to that of the main peaks and one might question whether the probe

intensity that we used is too high for a valid RABBITT analysis. It is true that higher probe intensity tends to flatten the phase of HHG [30], and the calculation of the pulse duration from the deduced phases can be underestimated using the second-order perturbation theory. However, it almost has no effect on qualitatively determining trajectory groups based on the sign of slope of the line connecting the sideband oscillation maxima. To confirm this, we also took data with a much lower probe intensity and found that the same sideband pattern was produced, although with slightly worse counting statistics. We further investigated this point using a strong field approximation (SFA) calculation (described below) and found that the sideband pattern changes little with IR probe intensity below 10^{12} W cm^{-2}, the intensity range used in this experiment.

4. Theoretical comparison

4.1. Single-atom response

We first investigate to what extent these results can be understood on the basis of the generation of harmonics from a single atom, without taking into account propagation effects in the gas medium. We begin with a brief summary of the semi-classical picture which identifies the major physical effects expected. In this picture, the ionized electron is tunnel-ionized at the initial time t_e. When the electric field reverses its direction, electrons can be pulled back and recollide with the ion core at the final time t_f, which indicates the emission time of HHG. The time pair (t_e, t_f) defines an electronic trajectory. HHG below the cutoff is attributed mainly to these two trajectory groups, short (with $\tau = t_f - t_e$ near a half optical cycle) and long (with τ near a full optical cycle) [24]. The phase, or the classical action of the electron trajectory which also approximately corresponds to the phase of the emitted harmonic, can be approximately expressed as $\phi_j(t) \approx -U_p\tau_j \approx -\alpha_j I(t)$ [15], where U_p is the pondermotive energy of the driving laser and τ_j is the electron excursion time for the jth trajectory. The constant α_j is roughly proportional to τ_j and $I(t)$, the time-dependent laser intensity. Therefore, the phase is proportional to the laser intensity. Since the long trajectory has a longer excursion time than that of the short trajectory, the magnitude of α_j is much larger for this case and the phase is more sensitive to the laser intensity than is that for the short trajectory [31]. The variation of intensity during the finite pulse duration leads to a corresponding time variation of the phase, and the time derivative of this appears as a frequency shift in the HHG spectrum. The leading-edge portion of the driving field corresponding to an increasing intensity with time will drive a blue shift, while the trailing-edge portion of the driving field will drive a red shift with a decrease of the intensity. The shift is much larger for the long trajectory than for the short one and thus should shift the frequencies for these two trajectories differently and lead to a spectral splitting for each harmonic. If HHG from both short and long trajectories are present and both were emitted only on the rising edge of the pulse, one would expect a large blue shift for the long trajectory and a small blue shift for the short trajectory. Similarly, the expected chirp of the HHG is expected to be different for the short and long trajectories. For short trajectories, the emission time increases with harmonic number, while for long trajectories, it decreases. As discussed in [24], this implies that in a RABBITT scan, a line drawn through the maxima of the sidebands will have a small positive slope (positive chirp), while the corresponding slope for long trajectories will be negative (negative chirp).

In order to evaluate this single-atom expectation quantitatively, we performed a quantum mechanical calculation of the HHG spectrum in a slightly modified version of the SFA. Using the Lewenstein model [32], the time-dependent dipole moment of an atom in a strong field is given as

$$D(t) = \mathrm{i}\int_0^\infty \mathrm{d}\tau \left(\frac{\pi}{\varepsilon + \mathrm{i}\tau/2}\right)^{3/2} \mathrm{d}^*[P_s(t,\tau) - A(t)]a^*(t) \times \exp(-\mathrm{i}S(P_s,t,\tau)) \times E(t-\tau)\cdot \mathrm{d}[P_s(t,\tau) - A(t-\tau)] \times a(t-\tau) + \mathrm{c.c.}, \quad (1)$$

where $d(p)$ is the transition dipole matrix element between the ground state and a continuum state with momentum p. $E(t)$ and $A(t)$ represent the electric field of the laser pulse and the associated vector potential, respectively, and ε is a positive regularization constant. P_S and $S(P,t,\tau)$ are the canonical momentum and quasi-classical action of the continuum electron, respectively. Ground-state depletion is included by introducing the ground-state amplitude $a(t) = \exp\left[-\frac{1}{2}\int_{-\infty}^{t} w(t')\,\mathrm{d}t'\right]$ [44], where $w(t)$ is the ionization rate calculated with the ADK model [33]. We denote the Fourier transform of $D(t)$ as the induced dipole $D(\omega)$, and the HHG intensity is proportional to $\omega^4\,|D(\omega)|^2$, the momentum of the free election p and the angular frequency of the harmonic photon ω is related by the energy conservation law: $\hbar\omega = p^2/2 + I_p$.

In the SFA model, the transition dipole element $d(p)$ is calculated assuming that the unbound electron is a free electron in the strong laser field. An improvement on this model, which incorporates the interaction of this electron with the residual ion, can be obtained using the 'quantitative rescattering' (QRS) model [34–36]. In this model, the induced dipole moment $D(\omega)$ can be written as the product of a returning electron wave packet $W(\omega)$ and the photo-emission transition dipole $d_e(\omega)$ of the atom from the stationary scattering calculation: $D(\omega) = W(\omega)d_e(\omega)$. The electron wave packet $W(\omega)$ is a property of the laser only and can be deduced by dividing the SFA expression in equation (1) by $d(p)$. The transition dipole $d_e(p)$ is then calculated using 'exact' numerical wavefunctions for the bound and continuum states within the single active electron approximation. The resulting expression for the induced dipole $D(\omega)$, which becomes the result from equation (1) multiplied by the ratio $d_e(\omega)/d(p)$, was used to calculate the HHG spectrum.

Figure 5(a) shows the depletion factor $a(t)$ and figure 5(b) shows the HHG spectrum of argon calculated using the QRS model. In the calculation, the excursion time of the electron is limited to one optical cycle to eliminate the contribution from high-order recollision processes. This assumption is reasonable and emphasizes the major physical effect due to the

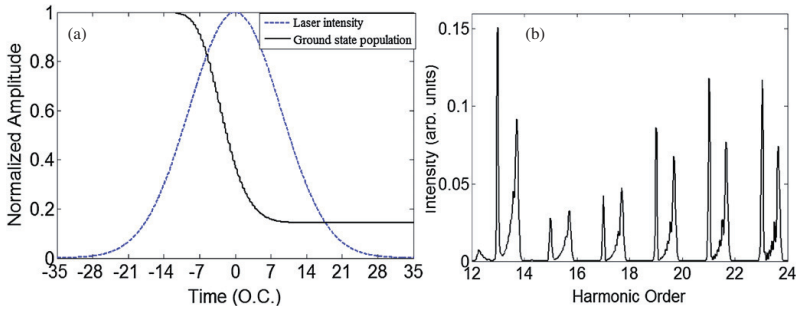

Figure 5. (a) The normalized laser intensity profile (blue dashed line) and the time-dependent ground-state population (black solid line) of argon. (b) The calculated HHG spectrum of argon under the single-atom response. The driving field is 60 fs with peak intensity of 3×10^{14} W cm^{-2}.

fact that high-order processes have more rapid phase variation because of the longer excursion time, and thus will die out quickly in the medium. The 60 fs long pulse has an intensity close to the saturation intensity of argon ($\sim 2 \times 10^{14}$ W cm^{-2}). In the model, the ground state is dramatically depleted, and harmonic generation ceases before the arrival of the peak of the pulse. Therefore, only blue shifts occur in the spectrum and short and long trajectories are separable in the frequency domain, with the higher frequency corresponding to the long trajectories.

Next we need to calculate the expected RABBITT spectrum. In the SFA, the IR-assisted EUV photo-ionization process can be simulated analytically [25]; the transition amplitude to the final continuum state $|v\rangle$ is given by

$$y(v,\tau) = -\mathrm{i}\int_{-\infty}^{+\infty} \mathrm{d}t\, \mathrm{e}^{\mathrm{i}\phi(t)} d_{p(t)} E_X(t-\tau)\, \mathrm{e}^{\mathrm{i}(W+I_P)t},$$
$$\phi(t) = -\int_{t}^{+\infty} \mathrm{d}t'[v \cdot A(t') + A^2(t')/2], \qquad (2)$$

where v is the momentum of the final continuum state $|v\rangle$. E_X(t) is the electric field of the EUV pulse, $A(t)$ is the vector potential of the IR field and d_P, W and I_P stand for the transition dipole moment, final kinetic energy of the electron and ionization potential of the target, respectively.

The right-hand panel of figure 6 shows the calculated RABBITT density plot of photoelectron yield versus EUV/IR delay. The spectrum of figure 5 is shown in the left-hand panel for reference. The calculated RABBITT spectrum shows clearly that the red and blue sidebands have very different phase behaviour. A line drawn through the maxima of the red sidebands shows a small positive slope, while that through the blue sidebands show a negative slope. These results are in agreement with the expectations of the semi-classical model, and allow us to assign the red sidebands to short trajectories and the blue sidebands to long trajectories. However, this correlation between slope and shift is exactly the opposite of that observed in the experiment, which seems to show that the blue sideband corresponds to the short trajectories. It is clear that the simple single-atom explanation fails to explain the data.

Note that the pulse duration and peak intensity that we used in the single-atom response are different from the

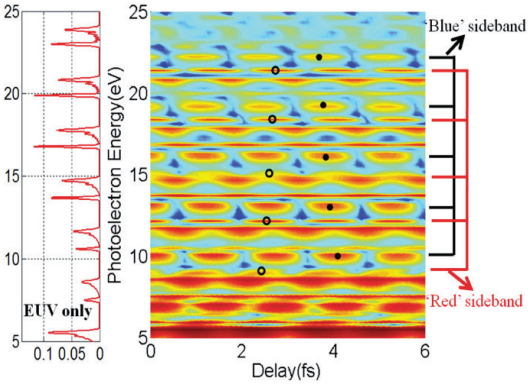

Figure 6. Left: the calculated photoelectron spectrum of argon when only EUV is present. Right: calculated EUV–IR cross-correlated traces. The HHG spectrum (figure 5(b)) used in the calculation is based on the single-atom response.

estimated experimental values. In the real experiment, the strong ionization of the medium by the laser will produce a considerable level of plasma. The dispersion of the plasma will tend to stretch the laser pulse and therefore reduce the peak intensity of the focused laser beam. Thus, it is reasonable to use a slightly longer pulse duration and lower peak intensity in the calculations to compare with the real experimental data.

4.2. Macroscopic effect

The disagreement between the single-atom response model and the experimental results shows the necessity of including propagation effects in the gas medium. These effects include three aspects in our case. The first is the phase matching coming from the phase velocity difference between the fundamental driving field and HHG field in the medium. The second is the plasma effect: because the laser intensity in our experiment is well above the saturation intensity of the gas, the plasma level could be appreciable. The nonlinearity of the plasma can induce distortion of the driving field in the time domain, which will eventually affect the HHG process. The third aspect is the absorption of the EUV in the gas medium.

The significant influence of the macroscopic effects for a long gas cell has been revealed by Ruchon *et al* [37]. All of these aspects can be taken into account by solving the coupled Maxwell equations in three dimensions. The details of the calculation can be found elsewhere [38–42]. We recall only the main equations here. The propagation of the fundamental field in an ionizing medium is described by

$$\nabla^2 E_1(r,z,t) - \frac{1}{c^2}\frac{\partial^2 E_1(r,z,t)}{\partial t^2} = \frac{\omega_0^2}{c^2}\left(1-\eta_{\text{eff}}^2\right)E_1(r,z,t), \quad (3)$$

where E_1 is the transverse electric field. The effective refractive index is

$$\eta_{\text{eff}}(r,z,r) = \eta_0(r,z,t) + \eta_2 I(r,z,t) - \frac{\omega_p^2(r,z,t)}{2\omega_0^2}. \quad (4)$$

The first two terms account for refraction, absorption and optical Kerr nonlinearity, and the third term describes the plasma effects with plasma frequency,

$$\omega_p = [e^2 n_e(t)/(\varepsilon_0 m_e)]^{1/2}, \quad (5)$$

where m_e and e are the mass and charge of an electron, respectively, and $n_e(t)$ is the density of free electrons. In the meanwhile, the propagation of the harmonic field is described by

$$\nabla^2 E_h(r,z,t) - \frac{1}{c^2}\frac{\partial^2 E_h(r,z,t)}{\partial t^2} = \mu_0 \frac{\partial^2 P(r,z,t)}{\partial t^2}. \quad (6)$$

The polarization $P(r, z, t)$ can be separated into linear and nonlinear components. The former one includes both linear dispersion and absorption effects of the HHG, and the latter one includes the so-called single-atom response and the remaining neutral atomic density. The single-atom response is calculated using the QRS theory [33–35]. Both equations (3) and (6) are solved by using the Crank–Nicholson routine in the frequency domain.

In the calculation [41], the on-axis propagation distance is 1.2 cm to mimic a semi-infinite gas cell. The real gas cell is 30 cm long and is much longer than the simulation length 1.2 cm. However, the laser does not see most of the gas cell in its optical path because only the very small focusing volume is the place where the laser distortion and HHG will take place. We used the region between the gas cell exit and 1.2 cm before the exit for the simulation. This is reasonable because outside this region, no appreciable flux will contribute due to the low laser intensity. According to the experimental conditions, the laser peak intensity, pulse duration and beam-waist in vacuum are 6×10^{14} W cm^{-2}, 50 fs and 25 μm, respectively. The focal position of the laser beam is set to be where the centre of the filamentation occurs. This position is approximately where the experimental focus is set for case III. However, this is not exact, since the laser beam in the medium can be self-focused and therefore the filamentation does not reflect the exact location of the focal point of the laser beam. The calculation is performed by integrating the differential equations from the very beginning to the end of the gas cell. At the exit of the gas cell, we will get the near-field EUV spectrum. In the experiment, the EUV will propagate in vacuum for 1 m before going through a 2 mm diameter hole mirror to combine with the IR probe beam. Thus, we perform a Hankel transformation on the calculated field to get the far-field distribution, and then an on-axis spatial filter is applied to select the HHG spectrum with a divergence less than 1 mrad to compare with the experimental data. Figure 7 shows the calculated far-field on-axis EUV spectrum. The splitting feature in the spectrum is well reproduced, similar to the single-atom response calculation. The IR-assisted photoionization spectrum was then calculated to extract the phase information of the calculated EUV spectrum (see figure 8). We can see that after including the propagation effect, the calculation shows that the blue sideband has the small positive slope, while the red sideband shows a negative slope, in agreement with the experimental data and exactly opposite to the single-atom response result. It is clear that taking propagation effects into account is essential to explain the phase behaviour of the observed spectral splitting.

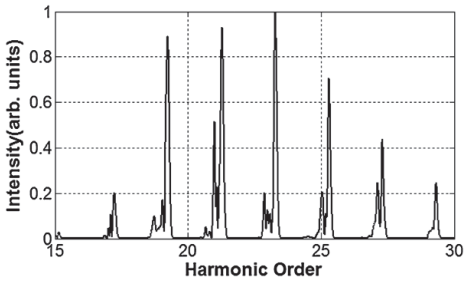

Figure 7. Calculated HHG spectrum at the far-field with divergence less than 1 mrad, the driving field is 50 fs with a peak intensity of 6×10^{14} W cm^{-2} and the focal point is in the middle of the 1.2 cm gas cell in vacuum.

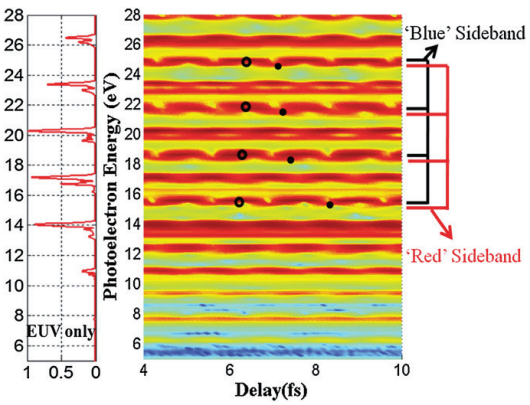

Figure 8. Left: the calculated photoelectron spectrum of argon when only EUV is present. Right: calculated EUV–IR cross-correlated traces. The HHG spectrum used in the calculation has included the propagation effect (see figure 7).

5. Discussion

The additional phase information available to us from the RABBITT scans presents strong evidence that the blue

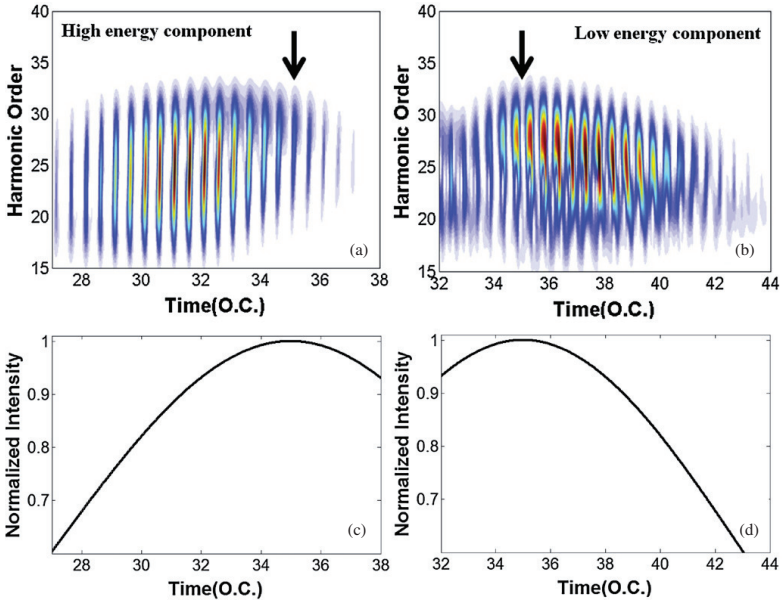

Figure 9. Time–frequency analysis of the HHG signal gated on the lower energy component (a) and the higher energy component (b) of the spectrum in figure 6. The black arrows indicate the location of the peak of the driving field. (c), (d) The normalized intensity profile of the laser in vacuum.

sideband in the split spectrum is due mainly to the short trajectories, not the long trajectories as might be expected on the basis of a single-atom response treatment. The full calculation including macroscopic effects is in agreement with the data. We now attempt to use this calculation to find why the short trajectory corresponds to the higher frequency component instead of the lower frequency component. While both absorption and plasma effects enter into the propagation calculation, the absorption of the gas medium typically only modifies the amplitude of the spectrum and has no contribution to the phase behaviour of the HHG. The phase matching issue is related to the coherent summation of XUV photons generated at different locations. It depends on the energy and space-dependent efficiency of harmonic generation, which is likely to be the major factor governing both the spectral splitting and the phase evolution of the HHG.

In order to probe more deeply the origin of the two harmonic side-peaks, an appropriate spectral gate was applied to select only one component of the double-peak harmonic signal. Then the time–frequency analysis was performed on the gated signal such that both frequency and timing information can be revealed simultaneously in a single spectrogram. Figure 9 shows the calculated spectrograms corresponding to different sub-peaks in the EUV spectrum of figure 7. The 'blue' or higher energy component for each harmonic order, which shows a reasonable positive chirp (lower frequency photons lead higher frequency photons), is generated at the leading edge close to the peak of the laser intensity profile. This indicates a clean short-trajectory group experiencing a small blue shift. On the other hand, the 'red' or lower energy component for each harmonic order is generated at the trailing edge of the laser pulse and therefore will experience a red shift in the frequency domain. It should be noted that in the experimental (figure 4) and simulated results (figure 8), the chirp of the sideband from the low-energy group is much larger than the expected one from the long-trajectory group alone. This is caused by the mixture of a weak short-trajectory signal with the long-trajectory group. The interference of the two groups will change the phase behaviour dramatically [43]. However, the long-trajectory behaviour is still dominating.

Why does the long trajectory favour the trailing edge of the laser pulse? One contributing factor comes from the evolution of the fundamental driving field. At a laser intensity close to or beyond the saturation intensity, free electrons can distort the fundamental field by introducing a nonlinear term into Maxwell's equations, which leads to a positive chirp in the carrier of the laser field after propagating for a certain distance. Based on the quantum mechanical theory under the SFA, the phase $\Phi(t)$ associated with each quantum trajectory or path is related to the intensity I and angular frequency ω of the driving field by approximately $\Phi(t) \propto \tau U_p \propto I\alpha/\omega^3$, where τ is the excursion time of the electronic trajectory. The larger the carrier frequency ω, the weaker the intensity dependence of the phase. Therefore, if the driving field is positively chirped (or the carrier frequency is increasing with time), high-order harmonics generated at the leading edge will experience a larger divergence than do those generated from the trailing edge of the laser field. Therefore, radiation from the long trajectory which is discriminated against by its larger angular divergence and small angular acceptance of the

experiment tends to escape this discrimination somewhat when it is generated on the trailing edge of the driving field. The short-trajectory radiation, which is characterized by a smaller angular divergence, has no need to await the higher driving frequency and can be generated efficiently on the leading edge of the driving field. Although the plasma-induced chirp on the fundamental field gives qualitative explanation, we do believe that this could be a much more complicated process including the plasma-induced dispersion, plasma-induced nonlinearity and the phase matching between the fundamental and HHG fields. Further studies are needed to fully understand the underlying mechanism.

6. Conclusion

The spectral splitting of HHG from a semi-infinite gas cell has been investigated experimentally. An EUV–IR cross-correlation (RABBITT) experiment has been carried out to characterize the phase behaviour (or to identify the quantum path) associated with each component of the split HHG. The result indicates that the high (low) energy component of each harmonic order is identified as a short (long) trajectory, which is counterintuitive and different from what the single-atom model predicts. By numerically solving the coupled Maxwell equations, the macroscopic effect of propagation through the medium is considered and a result is obtained in good agreement with the experiment. This agreement shows that a correct treatment of propagation effects such as the divergence of quantum paths of the HHG and the evolution of the fundamental field in the plasma is essential for a full understanding of the spectral splitting. Further investigations, including the use of pulse-shaping techniques and pulses with variable wavelengths, are among the potential applications of this interesting phenomenon.

Acknowledgments

This work was supported by Chemical Sciences, Geosciences and Biosciences Division, Office of Basic Energy Sciences, Office of Science, US Department of Energy; WC was supported by the National Science Foundation under grant no CHE-0822646. GL was supported by the US Army Research Office under grant no W911NF-07-1-0475.

References

[1] Hentschel M *et al* 2001 *Nature* **414** 509
[2] Paul P M *et al* 2001 *Science* **292** 1689
[3] Sansone G *et al* 2006 *Science* **314** 443
[4] Spielmann C *et al* 1997 *Science* **278** 661
[5] Chang Z *et al* 1997 *Phys. Rev. Lett.* **79** 2967
[6] Itatani J *et al* 2004 *Nature* **432** 867
[7] Li W *et al* 2008 *Science* **322** 1207
[8] Corkum P B 1993 *Phys. Rev. Lett.* **71** 1994
Krause J L, Schafer K J and Kulander K C 1992 *Phys. Rev. Lett.* **68** 3535
[9] Salières P *et al* 2001 *Science* **292** 902
[10] Lewenstein M, Salières P and L'Huillier A 1995 *Phys. Rev.* A **52** 4747
[11] López-Martens R *et al* 2005 *Phys. Rev. Lett.* **94** 033001
[12] Schafer K J *et al* 2004 *Phys. Rev. Lett.* **92** 023003
[13] Cao W *et al* 2007 *J. Phys. B: At. Mol. Opt. Phys.* **40** 869
[14] Brugnera L *et al* 2011 *Phys. Rev. Lett.* **107** 153902
[15] Zair A *et al* 2008 *Phys. Rev. Lett.* **100** 143902
[16] Schiessl K *et al* 2007 *Phys. Rev. Lett.* **99** 253903
[17] Wang Y, Liu Y, Yang X and Xu Z 2000 *Phys. Rev.* A **62** 063806
[18] Zhong F *et al* 2002 *Phys. Rev.* A **65** 033808
[19] Brunetti E, Issac R and Jaroszynski D A 2008 *Phys. Rev.* A **77** 023422
[20] Xu H, Xiong H, Zeng Z, Fu Y, Yao J, Li R, Cheng Y and Xu Z 2008 *Phys. Rev.* A **78** 033841
[21] He X *et al* 2009 *Phys. Rev.* A **79** 063829
[22] Véniard V, Taïeb R and Maquet A 1996 *Phys. Rev.* A **54** 721
[23] Paul P M, Toma E S, Breger P, Mullot G, Auge F, Balcou P, Muller H G and Agostini P 2001 *Science* **269** 1689
[24] Mairesse Y *et al* 2003 *Science* **302** 1540
[25] Mairesse Y and Quéré F 2005 *Phys. Rev.* A **71** 011401
[26] Steingrube D S *et al* 2009 *Phys. Rev.* A **80** 043819
[27] Ulrich J *et al* 1997 *J. Phys. B: At. Mol. Opt. Phys.* **30** 2917
[28] Dörner R *et al* 2000 *Phys. Rep.* **330** 95
[29] Antoine P, L' Huillier A and Lewenstein M 1996 *Phys. Rev. Lett.* **77** 1234
[30] Swoboda M *et al* 2009 *Laser Phys.* **19** 1591
[31] Gaarde M B *et al* 1999 *Phys. Rev.* A **59** 1367
[32] Lewenstein M *et al* 1994 *Phys. Rev.* A **49** 2117
[33] Ammesov M V, Delone N B and Krainov V P 1986 *Zh. Eksp. Teor. Fiz.* **64** 1191
[33a] Tong X M and Lin C D 2005 *J. Phys. B: At. Mol. Opt. Phys.* **38** 2593
[34] Lin C D, Le A T, Chen Z, Morishita T and Lucchese R R 2010 *J. Phys. B: At. Mol. Opt. Phys.* **43** 122001
[35] Morishita T, Le A T, Chen Z and Lin C D 2008 *Phys. Rev. Lett.* **100** 013903
[36] Le A T, Lucchese R R, Tonzani S, Morishita T and Lin C D 2009 *Phys. Rev.* A **80** 013401
[37] Ruchon T *et al* 2008 *New J. Phys.* **10** 025027
[38] Priori E *et al* 2000 *Phys. Rev.* A **61** 063801
[39] Gaarde M B, Tate J L and Schafer K J 2008 *J. Phys. B: At. Mol. Opt. Phys.* **41** 132001
[40] Tosa V, Kim H T, Kim I J and Nam C H 2005 *Phys. Rev.* A **71** 063807
[41] Jin C, Le A T and Lin C D 2011 *Phys. Rev.* A **83** 023411
[42] Jin C *et al* 2011 *J. Phys. B: At. Mol. Opt. Phys.* **44** 095601
[43] Kruse J E *et al* 2010 *Phys. Rev.* A **82** 021402
[44] Jin C, Le A T and Lin C D 2009 *Phys. Rev.* A **79** 053413

Chapter 6

Experimental method: pump-probe scheme with single harmonic

6.1 Motivation and method

In the previous chapters, we mainly emphasized the temporal structure of high order harmonics and its applications to time-resolved studies of ultra-fast dynamic processes in atoms and molecules. In this chapter we will focus on the frequency domain of HHG and its potential application to the pump-probe study of molecular systems.

A strong monochromatic driving field can generate a sequence of harmonics up to the soft x-ray region. The separation of consecutive harmonics is twice the fundamental field photon energy (3.1 eV for 800 nm laser), and the bandwidth of each harmonic is roughly on the same order as (typically broader than) the fundamental field bandwidth (50 meV for a 50 fs laser pulse). This unique feature of HHG indicates its second application: a superbroad light source with well defined step size and resolution covering the wavelength range from infrared to soft x-ray. Since the HHG source is coherent, a single harmonic still preserves a pulse duration of the order of femtoseconds [51–53]. By combining the HHG with a monochromator, a table-top tunable light source can be realized for spectroscopy and

dynamic studies. This brings up the motivation of this project with a single harmonic as the pump. If a harmonic sequence instead of a single harmonic is used as a pump pulse, multiple channels would be launched. The probabilities of different channels to be populated heavily depends on their photoexcitation or photoionization cross section. From the experimental point of view, the study in general is limited in general to the dominant channels. The major advantage of a single harmonic over a harmonic sequence is that a single harmonic can initiate a rather clean process. This is even more crucial in the case of molecules, where several degrees of freedom are involved. Such few body systems will benefit from the use of the monochromatic source for initial state preparation. This correspondingly enhances the experimental detection ability of specific pathways as well as simplifies the theoretical treatment of the problem. A good analogy to the single harmonic versus harmonic sequence case is the single attosecond pulse and the attosecond pulse train. The single attosecond pulse is preferred for launching a clean wavepacket in the time domain so that it provides the potential for direct sub-femtosecond dynamic study. On the other hand, the attosecond pulse train, which has superior photon energy resolution for each harmonic, launches multiple wavepackets sequentially and the interference effect is embedded into the final product.

Up to now, there are mainly three methods for spectral filtering of high order harmonics. The first one is based on the use of multi-layer dielectric mirrors [105, 106]. This mirror is manufactured such that it only reflects a certain wavelength range. By using a pair of such mirrors, the unwanted wavelengths can be suppressed dramatically and a single harmonic in the EUV or soft x-ray region can be selected. The second technique is based on transmission through metallic filters [53, 107]. The transmission spectrum of the filters depends on the material and thickness of the filter. By selecting different filters, different spectral ranges can be picked up. Both schemes have very limited choices of wavelength and thus suffer poor photon energy tunability. A third approach for single harmonic selection is based on the use of gratings [51, 108]. A grating can disperse the harmonics spatially, therefore by inserting a slit after the grating the wavelength of interest can be selected. It has great

tunability. However, there are disadvantages such as pulse stretching and low transmission. The stretching of the pulse can be compensated completely by using a second identical grating in a parallel configuration, while the lack of flux resulting from the low transmission can be overcome by selecting high harmonics with longer wavelength, which have a relatively higher conversion efficiency.

Our experimental setup is based on the grating scheme as shown in Fig. 6.1. After the HHG cell, an aperture with a variable size is placed in front of the grating for alignment and spatial filtering purposes. A first plano grating is used to disperse the high order harmonics spatially. A second identical grating is placed about 2 inches away from the first grating with the surfaces parallel to each other. In such a configuration, the outgoing beam after the grating pair will be parallel to the incoming beam before the grating pair, and therefore the toroidal mirror downstream can focus the dispersed beam properly. Another purpose of the second grating is to compensate the pulse stretching caused by the first grating. A slit is positioned right after the second grating (about 65 cm from the HHG source point). The size of the slit is fixed typically at 1 mm, which sets the upper limit of the divergence of the delivered beam at 1.5 mrad. The laser polarization is parallel to the groove lines, which is S-polarized in our setup, so that the efficiency of the diffracted light is maximized. After the slit, the filtered harmonic is focused by the toroidal mirror and recombined with the IR probe beam in the same way as introduced in chapter 3.

6.2 Temporal stretching of the pulse

As we mentioned earlier, the grating scheme for single harmonic selection can cause pulse stretching. This could be crucial when trying to study dynamic processes. It is worthwhile to discuss this issue quantitatively. In order to satisfy the constructive interference condition,

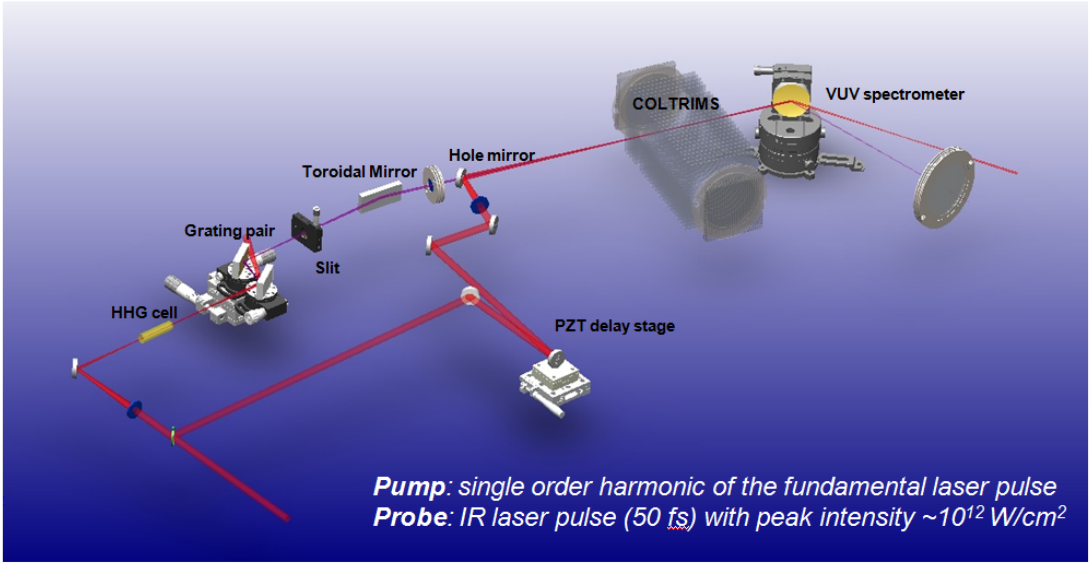

Figure 6.1: Schematics of the VUV-IR pump-probe experiment. Single harmonic VUV light selected with the grating pair acts as the pump beam.

the path difference between reflections from adjacent grooves in the grating is given by:

$$\Delta l = d(\sin\alpha + \sin\beta) = m\lambda, \tag{6.1}$$

where α and β represent the incident and diffracted angle, respectively. d and λ stand for the groove distance and wavelength of the light, and m is the diffraction order. The temporal dispersion in this case is given by $\tau = \dfrac{\Delta l}{c} = \dfrac{m\lambda}{c}$, with c the speed of light. The effective stretching of the light diffracted from a single grating is then given by $\Delta t = n\tau = n\dfrac{m\lambda}{c}$, where n is the number of grooves illuminated by the incident light. Now if we put a second identical grating with the surface parallel to that of the 1st grating, for the same diffraction order the optical path on the second grating retains the same geometry, but the light propagation direction is reversed. Thus the overall stretching of the pulse caused by the grating pair will be:

$$\Delta t_T = (n_1 - n_2)\frac{m\lambda}{c}, \tag{6.2}$$

where n_1 and n_2 indicate the number of grooves illuminated on the first and second grating, respectively. For a well collimated light source, $n_2 = n_1$, so there is no stretching in this configuration. However, stretching will occur if the beam is diverging, i.e. $n_2 > n_1$. The effective temporal stretch of the pulse is now proportional to the groove number difference instead of the number of grooves illuminated by the beam. The groove density of the grating used in our setup is 3600/mm. Considering a 1.5 mrad divergence beam placed 60 cm away from the first grating (5 cm separation between the 2 gratings), the groove number difference is 270 with 3240 as the number of grooves illuminated on the first grating. This indicates that the stretching effect is suppressed dramatically, and it could be improved by reducing the grating pair separation and the divergence angle of the laser beam. For a VUV light source with a wavelength of 80 nm, the pulse will be stretched by roughly 70 fs resulting in a pulse duration of about 90 fs in our setup (assuming the original pulse has a 20 fs Fourier transform limited pulse duration). This is comparable to the IR probe pulse duration (50 fs) and thus the pump-probe time resolution is slightly affected by the VUV pulse duration.

6.3 Efficiency of the grating pair

Another concern when using a grating-based monochromator is the low transmission efficiency, especially in the case of a double grating. Suppose a single grating gives 30% diffraction efficiency, it will drop to 9% if a second grating is applied. As a result, the experiment may suffer from a low counting rate and high noise level. A straightforward way to improve the high harmonics transmission is using blazed gratings. The sawtooth structure of the grooves on the blazed grating will concentrate the energy of the light towards the diffraction order of interest, and thus improve the diffraction efficiency. The total efficiency can be estimated using the Huygens-Fresnel equation under the scalar approximation. In this approximation both the polarization and absorption of the VUV light are neglected, but it can still provide preliminary guidance to determine the optical geometry. The Huygens-

Fresnel principle describes the light propagation as a coherent superposition of a series of secondary waves. This can be formulated as:

$$U(Q) = \frac{1}{j\lambda} \iint_S U(P) \frac{\exp(jkr_{PQ})}{r_{PQ}} K(\theta) dS. \tag{6.3}$$

In the equation above, $U(P)$ is the complex amplitude of the wave on the original surface S, while $U(Q)$ is the complex amplitude that we want to calculate on a reference plane R (see Fig. 6.2). r_{PQ} is the distance between P and Q, and $K(\theta)$ is the inclination factor.

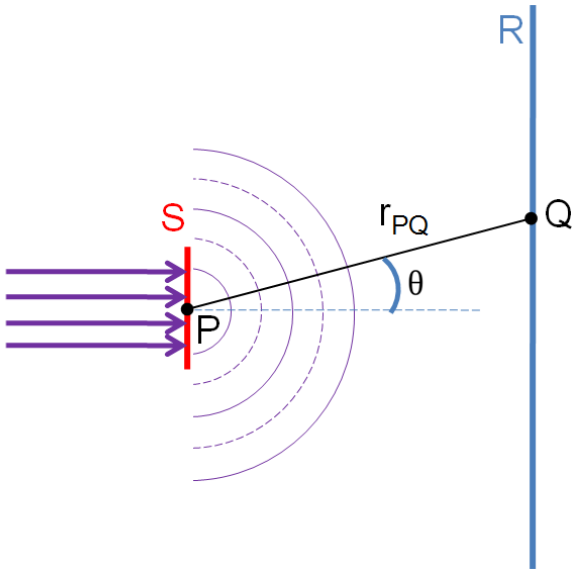

Figure 6.2: Geometric arrangement for Huygens-Fresnel principle

For simplicity, we consider a collimated incoming VUV beam, *i.e.* a plane wave. Figure 6.3 shows the typical arrangement of the grating pair and the associated optical path.

As long as the VUV beam reaches the first grating, the wave front will experience a periodic phase modulation because of the groove structure. We can set the grating surface as the original surface, then the complex amplitude of the beam is known if we know the groove density and the blaze angle. With equation 6.3, the diffracted wave pattern can be calculated. The efficiency of a specific diffraction order is calculated by taking the integral of

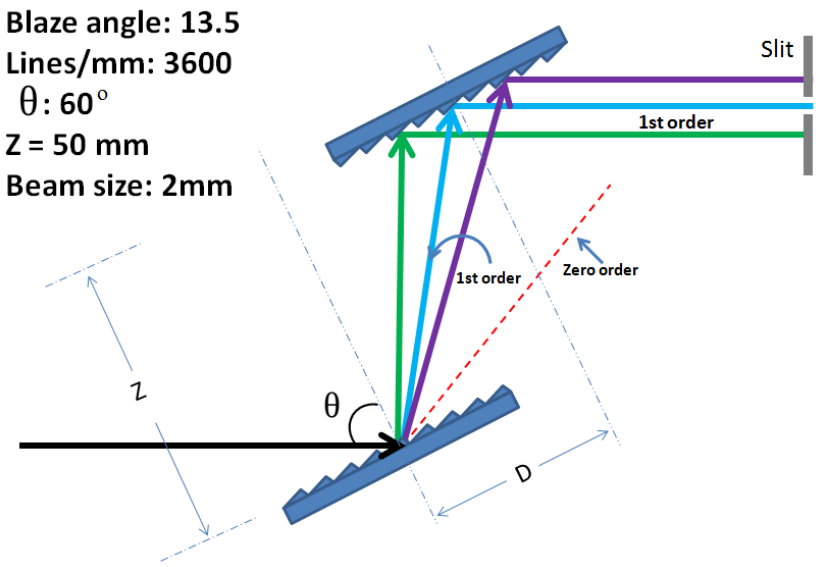

Figure 6.3: Arrangement of grating pair

the corresponding diffraction angle. Following the same method, the diffraction efficiency on the second grating can also be evaluated. Note that the incident angle on the second grating is equal to the diffraction angle on the first grating. A product of the efficiencies on the two gratings gives the total diffraction efficiency. Figure 6.4 shows the calculated efficiency of diffraction orders as a function of harmonic orders with the experimental parameters given. For the range starting from the 6th (133 nm) harmonic to the 11th (72.7 nm) harmonic, the total efficiency of the first diffraction order is above 50% while that of the higher diffraction orders is less than 2.5%.

Our experiments employ harmonics that are within this range for two purposes: (1) the VUV source is near-threshold high order harmonics and thus has a relatively higher conversion efficiency; (2) the higher diffraction order is suppressed, thus reducing the possible contamination of the VUV pump beam. For harmonic photon energies that are larger than the free spectral range (which is the largest wavelength range for a given diffraction order that does not overlap the same range in an adjacent order) the higher diffraction order will overlap with the lower order (e.g. 3rd diffraction order of 27th harmonic will overlap with the first diffraction order of the 9th harmonic). However, for an incident angle of

60° the absorption of the photons with energy above 30 eV becomes severe, and thus the transmission will be suppressed dramatically. The plane ruled reflectance gratings from Richardson Gratings are aluminum coated. Then the grating is overcoated with MgF_2 to prevent oxidization of the aluminum. The reflectivity on Al at 60° incident angle is less than 0.15 for photons above 30 eV. The loss on the second grating will be even worse since the incident angle will be about 30° resulting in a reflectivity of less than 0.006 for photons above 30 eV (the EUV reflectivity from a single layer coating is obtained from the x-ray database of Lawrence Berkeley National Laboratory). This yields a total reflectivity of no more than 0.1%. On the other hand, the reflectivity of photons on Al can remains 0.4 for a wavelength of 75 nm (16.5 eV) even at normal incident angle, which indicates a higher reflectivity under the general experimental condition(60° and about 30° incident angles on the first and second grating). Therefore, ideally the grating pair arrangement should provide a decent clean VUV source in the wavelength of interest, i.e. 72 nm to 90 nm ($\sim$ 13.8 eV to $\sim$ 17.2 eV).

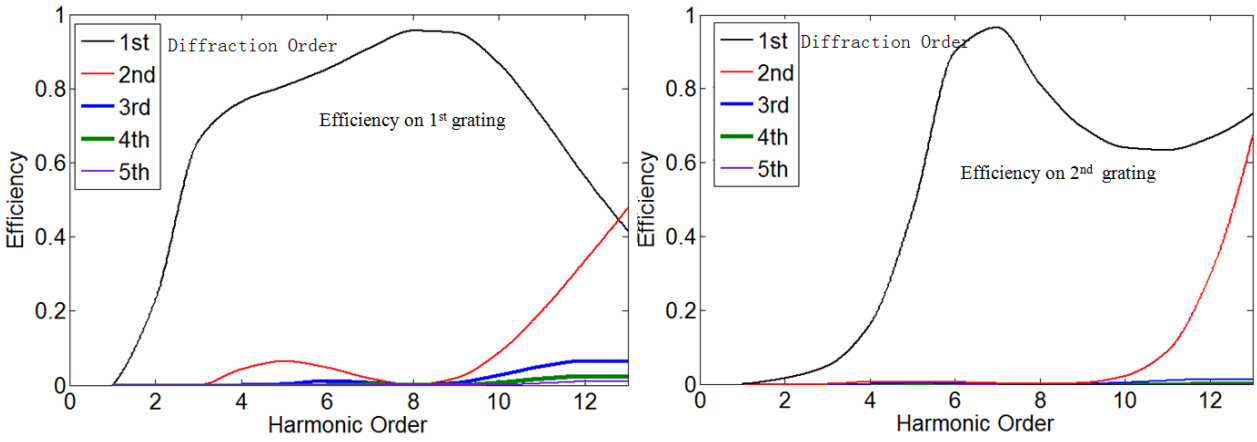

Figure 6.4: The diffraction efficiency on the first and second grating

6.4 The bandwidth of a single harmonic

In the high order harmonic generation process, the harmonic order gives roughly the number of fundamental photons involved in a non-linear process. For example, suppose the driving field has a Gaussian temporal profile with a pulse duration of $\tau = 50$ fs. The 9th harmonic indicates a 9-photon process, and thus its efficiency is roughly proportional to $I(t)^9$ where $I(t)$ is the intensity of the driving field. The FWHM duration of $I(t)^9$, is $\frac{\tau}{\sqrt{9}} = \frac{\tau}{3} =$ 17 fs. The uncertainty relationship between time and frequency for a Fourier transform limited Gaussian pulse is given as $\Delta t \times \Delta f = 0.44$. Thus a 17 fs pulse has a bandwidth of $\Delta\omega = 2\pi\frac{0.44}{\Delta t} = 0.107$ eV, which is the lower limit of the bandwidth of the 9th harmonic.

There are other sources that could broaden the bandwidth such as the phase-matching condition and over-saturation effect. The ratio of the long and short trajectory contribution of each harmonic will depend on the phase-matching condition as we discussed in chapter 3. For a driving pulse with finite pulse duration the frequency shifts of the long and short trajectories are different. If both short and long trajectories are present, the frequency broadening of the high order harmonics is expected. However, this broadening can be avoided by optimizing the phase-matching condition such that only one type of trajectory is dominating the HHG process. In the case of the over-saturation region, the peak intensity of the driving field is so high that the gas medium is completely ionized before the pulse reaches its peak intensity, and thus the HHG process is truncated in time (due to the termination of the recombination step). A shrinking of the pulse width in the time domain gives rise to a broadening of the signal in the frequency domain. Therefore, lower laser intensity is preferred to get a harmonic with a well-defined photon energy (i.e. narrow frequency bandwidth).

After the HHG generation cell, the VUV pulse will experience spatial dispersion from the grating pair. A following slit is then applied to select the frequency component of interest, i.e. select a single harmonic. Both the natural width of the harmonics from the generation cell and the optical monochromator geometry determine the effective bandwidth

of the VUV pulse in the pump-probe interaction region. The opening size of the slit is typically 1 mm in the current experimental setup. This corresponds to a 0.9 eV bandpass filter for the 9th harmonic in our double grating configuration. By reducing the slit size further a bandpass filter with a smaller bandwidth can be realized, however this will decrease the transmitted photon flux significantly. To summarize, the slit size (1 mm) is chosen to block the neighbouring harmonics without reducing the selected harmonic flux significantly. Under this condition, it is the natural bandwidth of the harmonic that mainly determines the effective spectral width of the VUV pump harmonic in our current setup. This depends sensitively on the phase-matching conditions of high harmonic generation.

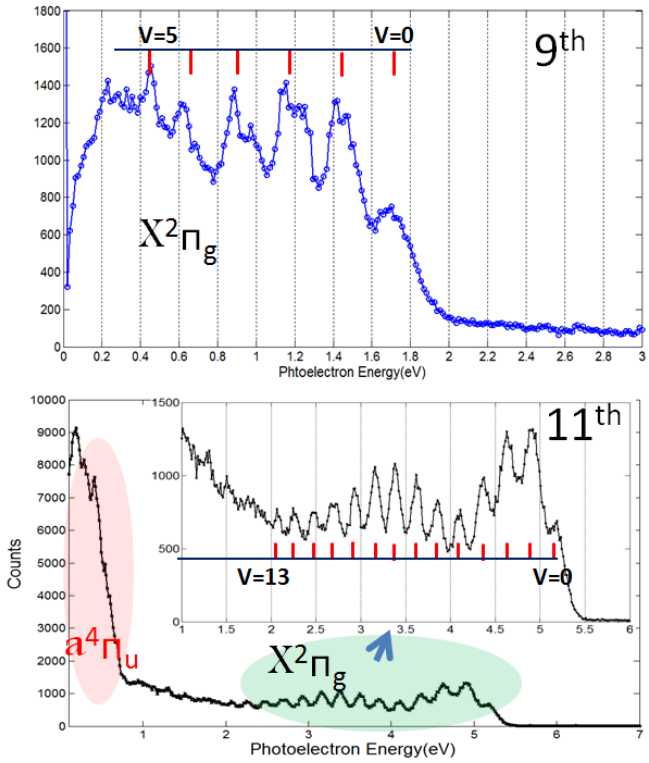

Figure 6.5: The photoelectron spectra of gas phase O_2

The very first experiment conducted on this setup demonstrated the spectral capabilities of the setup using a single harmonic delivered to an oxygen target. The argon gas is used to generate high order harmonics, and the 1 mm slit of the monochromator is positioned such that only the 9th or the 11th harmonic is delivered to interact with an O_2 target in

the COLTRIMS setup. Only the photoelectrons are detected under field free condition (i.e. the extraction electric field and static magnetic field are set to be zero) in order to optimize the energy resolution of the spectrometer for electrons. The detector is 8 cm in diameter and the distance between the interaction region and the detector is 21 cm, this corresponds to a 0.0448π solid angle of collection. Figure 6.5 shows the photoelectron spectra from gas phase O_2 ionized by the 9th or 11th harmonic. The fine structure in the spectra can be understood from the potential energy curves shown in Fig. 6.6.

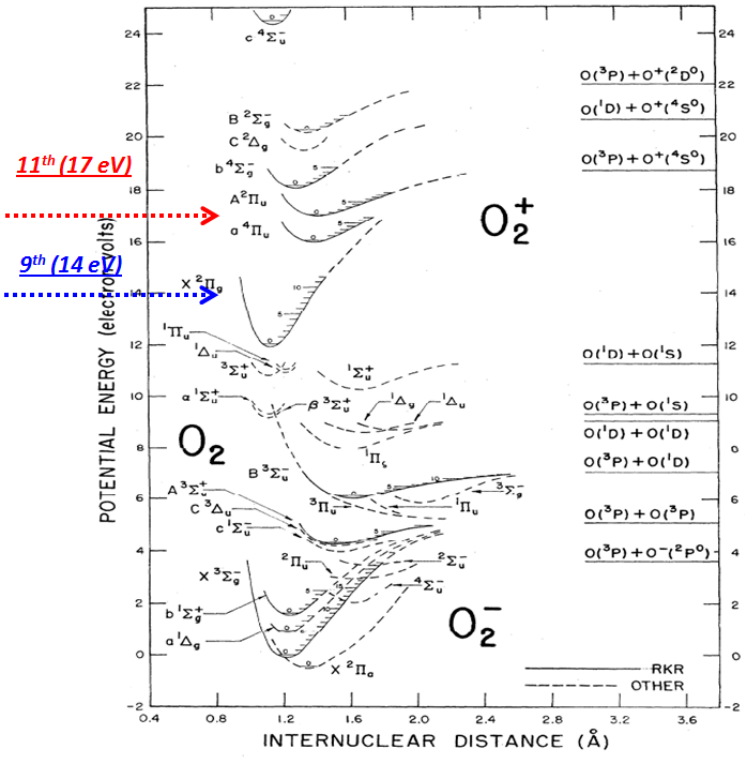

Figure 6.6: The relevant potential energy curves of O_2 and O_2^+, adapted from reference [109].

The O_2 cation state $X\ ^2\pi_g$ can be populated with the 9th harmonic via a single photon ionization process. The total photon energy is shared between the vibrational modes of the nuclei and the ionized electron. Thus the photoelectron energy images the vibrational structure of the $X\ ^2\pi_g$ cation state, and the amplitude follows the Franck-Condon principle. In the case of the 11th harmonic, both the $X\ ^2\pi_g$ and $a\ ^4\pi$ states can be populated leading to

two groups in the photoelectron spectrum. Higher vibrational states in the $X\ ^2\pi_g$ potential curve can be accessed resulting in rich structure in the photoelectron spectra. The bigger amplitude of the $a\ ^4\pi$ state group is likely due to the stronger dipole coupling from the neutral ground state of the O_2. The vibrational structure is well resolved in both the 9th and 11th harmonic cases. The energy separation between two adjacent vibrational states is roughly 200 meV, which indicates a bandwidth of 200 meV at most in the VUV light source. A Gaussian fit to the photoelectron spectra yields a bandwidth of about 200 meV for the VUV source.

This bandwidth is a result of the convolution of the natural width of VUV and the apparatus resolution. The apparatus resolution includes the momentum resolution parallel and perpendicular to the time-of-flight axis. Under field free conditions (no extraction field is applied across the spectrometer), the z-component velocity of the electron is : $v_\parallel = \frac{L}{t}$ where L is the flight distance of the electron parallel to the time-of-flight (TOF) axis, and t is the TOF of the ionized electron. The contribution to the kinetic energy of the electron along the TOF axis is thus $E_\parallel = \frac{m_e}{2} v_\parallel^2 = \frac{m_e L^2}{2t^2}$. The uncertainty of the electron energy along the TOF axis is caused by the TOF uncertainty $\delta t = 0.5$ ns (this is determined by the TDC used in our apparatus) and the fight distance uncertainty $\delta L = 100\ \mu$m (this is determined by the laser focusing geometry). The uncertainty associated with δt is: $\delta E_{\parallel_1} = m_e L^2 \frac{1}{t^3} \delta t = 40$ meV at $E = 3.5$ eV. The uncertainty associated with δL is given by: $\delta E_{\parallel 2} = \frac{L m_e}{t^2} \delta L = 3.5$ meV. Thus $\delta E_\parallel = \sqrt{{\delta E_{\parallel 1}}^2 + {\delta E_{\parallel 2}}^2} = 40.15$ meV. For momentum perpendicular to the TOF axis, $v_\perp = \frac{r}{t}$, where r is the transverse distance that the electron travels. The energy resolution is related to the MCP position sensitivity which is $\delta r = 250\ \mu$m. The corresponding energy uncertainty is $\delta E_\perp = \frac{m_e}{t^2} r \delta r$. $\delta E_\perp = 0.0088$ meV for $r = 2$ cm and $E_\parallel = 3.5$ eV. Thus the total apparatus energy resolution with photonelectron energy around 3.5 eV is $\delta E_{apparatus} = \sqrt{{\delta E_\parallel}^2 + {\delta E_\perp}^2} \sim 40.2$ meV. This indicates that the bandwidth extracted from Fig. 6.5 is pretty close to the natural bandwidth of the VUV light source. To our knowledge this is the highest resolution photoelectron spectrum ever recorded using a HHG source of VUV

radiation.

6.5 Synchronization of IR probe and VUV harmonic pump

The previous discussion showed the characteristics of the VUV light source coming out of the home-built VUV monochromator. The next step involves the synchronization of the IR probe to the VUV pump and the demonstration of two-color pump probe experiments with the current setup. Our grating-based monochromator removes the IR driving field from the VUV path completely in the double-grating system. Thus, the residual driving field is no longer a reference beam to overlap the pump and probe as described in chapter 3. The synchronization includes spatial and temporal overlap between the VUV and IR pulses. To achieve spatial overlap, a retractable VUV beam viewer is installed close to the interaction region (2 inches after the jet location) in the COLTRIMS chamber. The home-built beam viewer consists of a matched MCP set in a chevron configuration and a phosphor screen. The coarse spatial overlap can be obtained by carefully observing the image of both IR and VUV beams on the phosphor screen (Fig. 6.7 shows typical images of VUV and IR beams on the beam viewer).

The temporal overlap is the non-trivial part, which is carried out in two steps. In the first step, a grating pair with line density of 400/mm is used instead of the 3600/mm grating pair. With the lower line density, the first diffraction order of the fundamental driving field will follow exactly the same optical path as that of the 9th harmonic with the 3600/mm grating. Since we have a visible driving field in the pump arm as a reference now, we can use the same strategy as described in chapter 3 to find the temporal overlap between the pump and probe, i.e. by looking at the interference pattern of the two visible beams from both arms of the interferometer. Then we can carefully switch back the 3600/mm grating pair, and the first diffraction order of the 9th harmonic will overlap with the IR probe pulse.

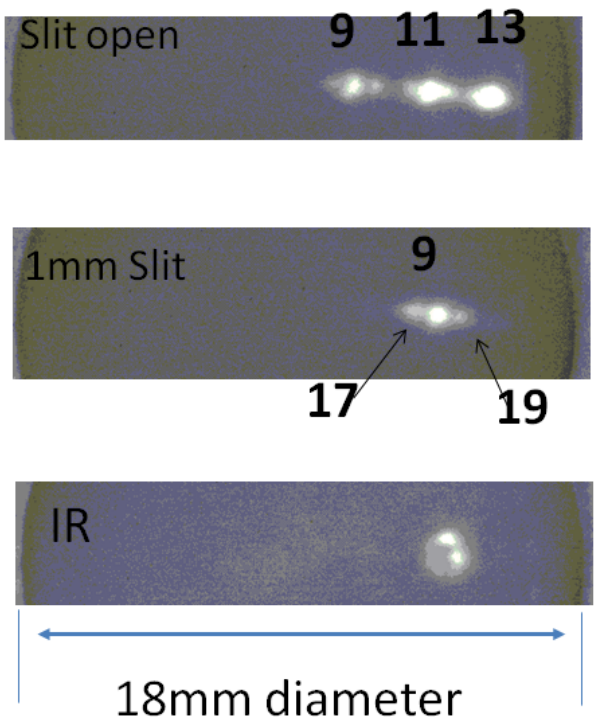

Figure 6.7: The images of VUV and IR beams on the beam viewer recorded by a CCD camera. Multiple harmonics are observed when the slit is open (top). Single harmonic (9th) can be selected by narrowing the slit down to about 1 mm (middle). The weak wings sitting on both sides of the 9th harmonic are coming from the second diffraction order of the 17th and 19th harmonic. They can be further suppressed by tuning the phase matching conditions of HHG. The wings have no contribution in a pump-probe experiment since they have no spatial overlap with the IR probe. The coarse spatial overlap is implemented by carefully moving the images of the IR (bottom) and VUV (middle) on top of each other.

This is just a coarse overlap as even a slight change in the alignment while switching from one grating pair to the other may cause significant mismatch. In the second step, a physics process that requires the presence of both VUV and IR beam is needed for fine tuning of the spatial and temporal overlap. The D_2 molecule is a candidate that can be used to check and fine tune the overlap.

Figure 6.8 shows the time-of-flight spectrum of D^+ and D_2^+ as a function of delay between the IR and the 9th harmonic. The enhancement of D^+ and D_2^+ counts around 120 fs corresponds to an overlap of the IR and VUV pulses. The physics process corresponds to

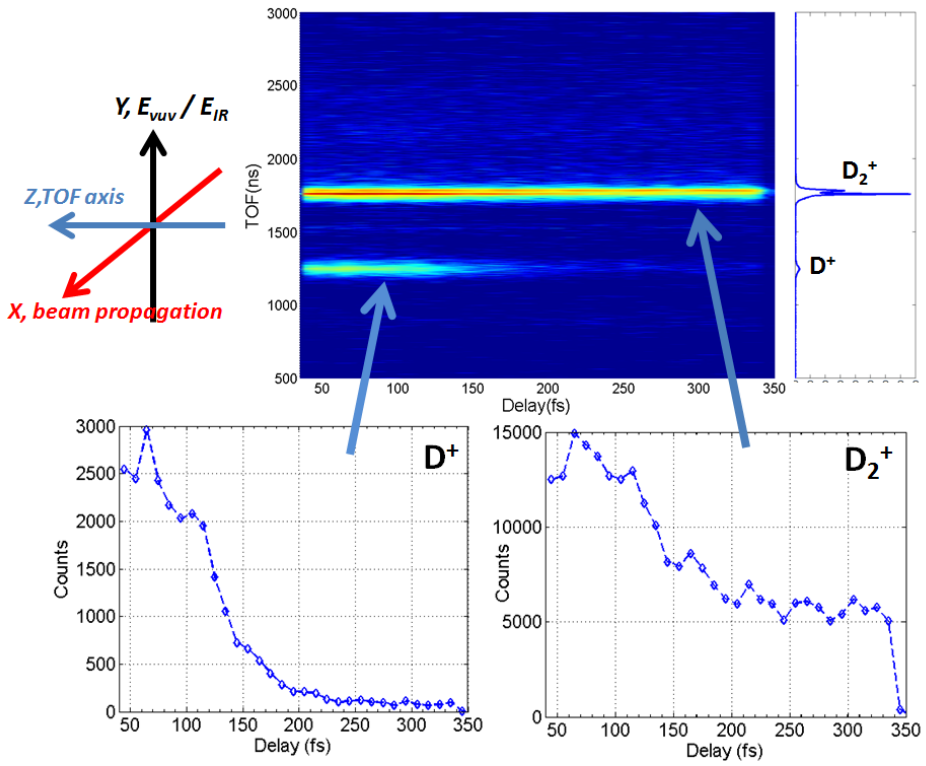

Figure 6.8: Time-of-flight spectra of D^+ and D_2^+ in the presence of IR probe and 9th harmonic pump.

the excitation of D_2 by the 9th harmonic followed by the ionization of D_2 by the IR probe pulse. By maximizing the counting rate of the total ion signal, the spatial and temporal overlap can be optimized. Up to now, we have just shown how to find and synchronize the IR probe pulse and the 9th harmonic pump pulse. In order to use a different harmonic order as a pump, the delay stage of the grating is translated accordingly as shown in Fig. 6.9.

Although the translation of the delay stage does not influence the spatial overlap in the interaction region, it results in different optical path lengths for different harmonics. The delay between the 11th and 9th harmonics in our geometry can be as much as 9000 fs. Since the 11th harmonic has a photon energy of 17 eV which is above the 1st ionization threshold of D_2, a different physics process will be required to check the temporal overlap. In the 11th harmonic case, we use argon gas as the candidate target for checking the temporal overlap. Figure 6.10 shows the photoelectron spectrum of argon as a function of the IR-11th harmonic

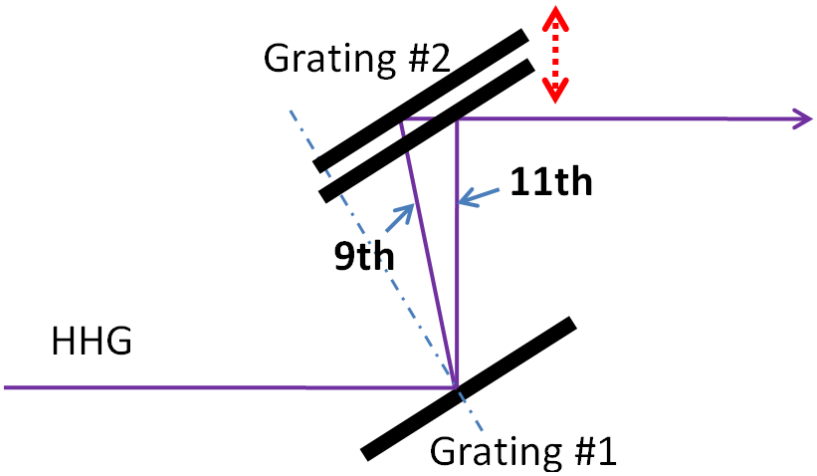

Figure 6.9: The optical path of the high order harmonics.

delay. The major band with photoelectron energy around 1.1 eV corresponds to ionization by a single 11th harmonic photon. The weaker sideband around 2.6 eV involves a two-photon process, where the 11th harmonic and an IR photon are absorbed simultaneously. The sideband requires the presence of both VUV and IR beams and thus provides the temporal overlap information between the two beams. It should be noted that not only the relative pump-probe delay but also the upper bound of the VUV pulse duration can be deduced from Fig. 6.8 for the 9th harmonic and Fig. 6.10 for the 11th harmonic. The time-dependent integral of a Gaussian function can be used to fit the delay-dependent enhancement of D^+ counts in Fig. 6.8(b). A Gaussian function can be used to fit the projected delay-dependent sideband signal intensity in Fig. 6.10. The full width at half maximum of each Gaussian function gives the upper bound of the corresponding VUV pulse duration, which is roughly 100 fs for both the 9th and 11th harmonics in the data presented. These values are consistent with the estimate made in section 6.3.

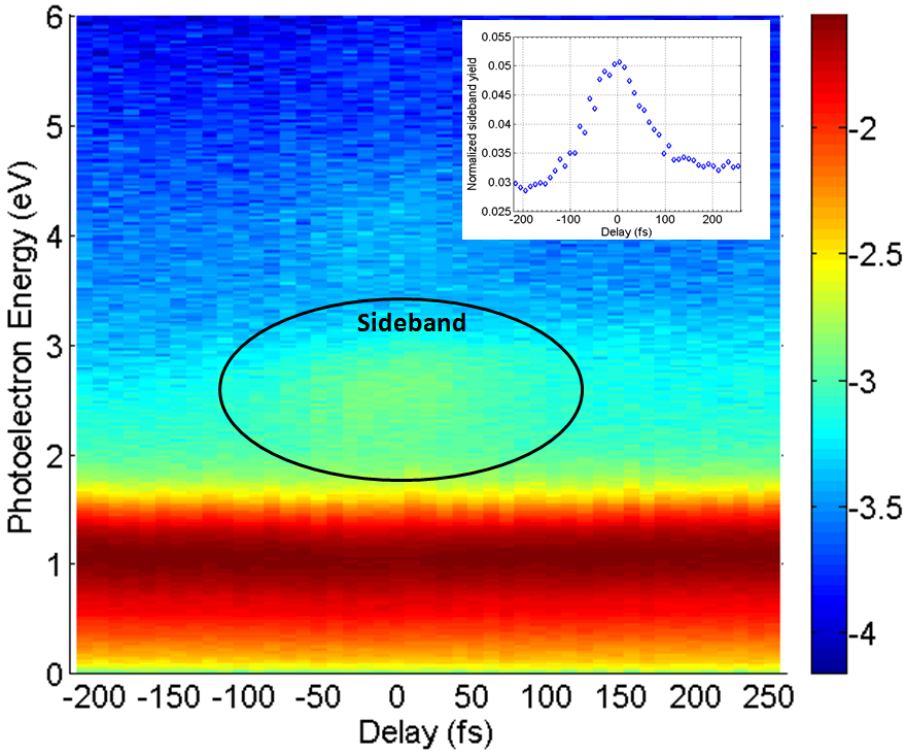

Figure 6.10: The photoelectron spectrum of argon versus IR-11th harmonic delay (logarithmic scale). The inset shows the sideband yield versus delay and its full width at half maximum is about 100 fs.

6.6 Dispersion and spatial chirp of the VUV pump

The grating based monochromator can inevitably introduce effects such as dispersion (i.e. different frequency components of the VUV travel different optical path lengths) and spatial chirp (different frequency components are focused at different locations on the focal plane). These effects are sketched out in Fig. 6.11.

As described in section 6.4, the bandwidth of a single harmonic in the VUV region can be as much as 200 meV depending on the phase-matching condition of HHG. This finite bandwidth will lead to the spatial separation of different wavelengths along the direction perpendicular to the propagation vector inside the diffraction plane. The beam profile of the VUV pulse at the focal point (interaction region) is therefore an ellipse instead of a circle. Additionally, due to the fact that different wavelengths will travel different optical

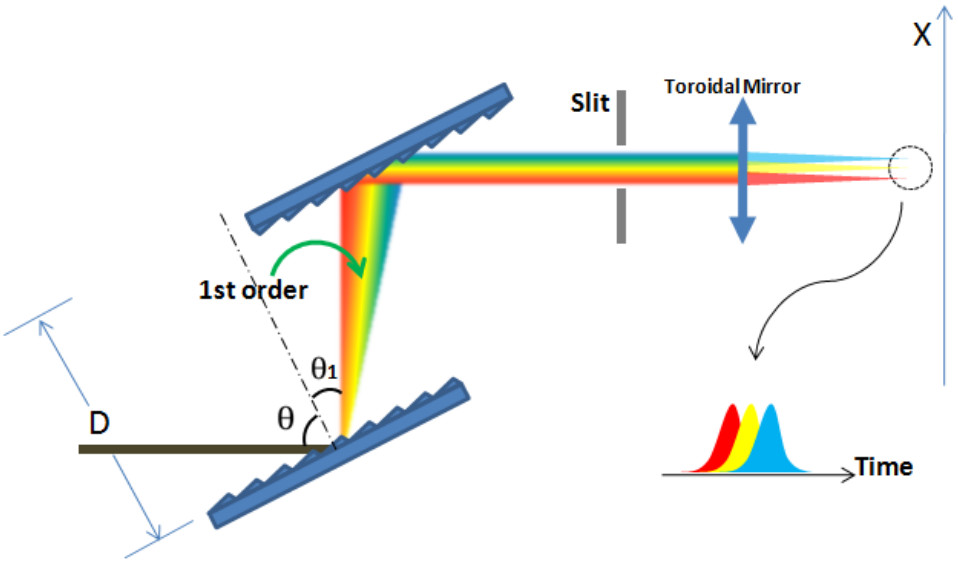

Figure 6.11: The schematic illustration of the dispersion and spatial chirp introduced by the grating pair.

paths, a temporal dispersion between different frequency components is expected. Based on the grating equation for the first diffraction order (this is the diffraction order used in our experiment), the difference in optical path introduced by the grating pair for wavelength λ is :

$$L_\lambda = \frac{D}{\cos(\theta_1)} \times (1 + \cos(\theta + \theta_1)), \tag{6.4}$$

The timing can be converted as: $t = \frac{L_\lambda}{800nm} \times 2.667fs$. The transverse position (along the x axis in Fig. 6.11) is: $X_\lambda = \frac{D \times \sin(\theta + \theta_1)}{\cos(\theta_1)}$, with D, θ, and θ_1 representing the separation of the gratings, the incidence angle and the diffraction angle, respectively. The calculated results as a function of the photon energy around the 11th harmonic are plotted in Fig. 6.12.

According to the first principle calculation in Fig. 6.12, the grating induced dispersion is ∼1000 fs/eV, and the spatial chirp along the transverse direction is ∼0.6 mm/eV. The beamsize of the VUV can easily be stretched to a few hundreds of μm due to the spatial chirp. This could potentially increase the interaction volume and degrade the system resolution.

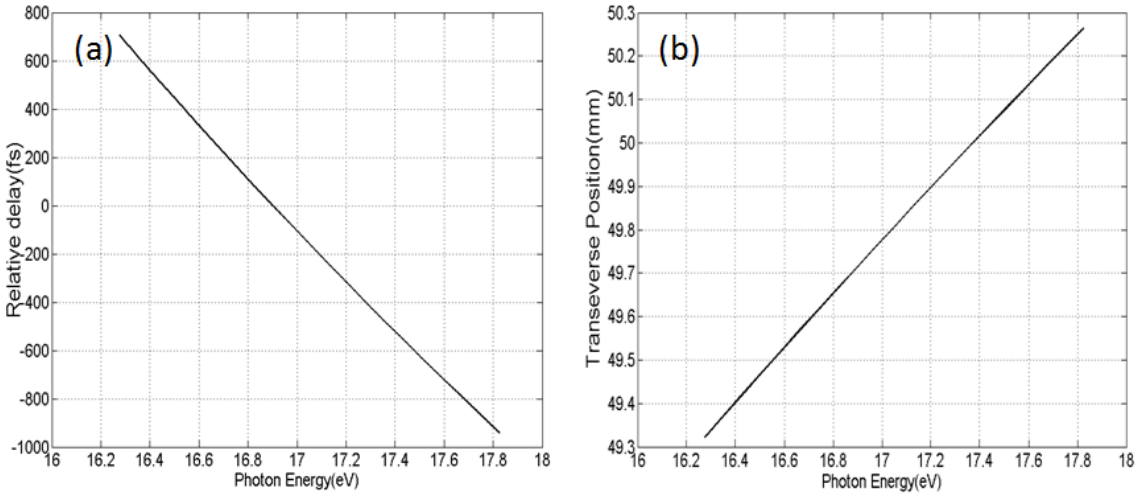

Figure 6.12: Calculated dispersion and spatial chirp introduced by the grating pair. (a)The relative timing of VUV beam arriving at the focal point as a function of photon energy. (b) The relative transverse position as a function of photon energy. The parameters in the calculation are consistent with our experimental setup. $D = 40$ mm, the groove density is 3600/mm, and incident angle is $\theta = 60°$.

Fortunately, this effective interaction volume can be reduced if we introduce an IR probe to perform a pump-probe experiment. The very small beam size of the IR in the interaction region (80 μm diameter) effectively serves as a slit, limiting the size of the VUV pump that can be synchronized with the IR probe pulse. Then the upper limit of the VUV bandwidth participating in the pump-probe experiment will be set by the IR beam size. With the spatial chirp of $\sim$0.6 mm/eV the effective bandwidth of the VUV in the pump-probe experiment is about 130 meV. This synchronized bandwidth corresponds to 130 fs dispersion from the shorter wavelength side to the longer wavelength side of the VUV pump pulse. This dispersion effect will broaden the effective temporal width of the VUV pulse. Additionally, if the VUV and IR are overlapping in time, the frequency component of the VUV that coincides with the peak of the IR will be delay dependent. Therefore the major frequency component of the VUV pump participating in the reaction will be shifted within the bandwidth of the VUV pump if the VUV-IR delay is changed. Although we used a specific grating pair arrangement for the D_2 experiments, it is rather straightforward to use

different combinations of grating parameters to optimize harmonics of interest for conducting different experiments. The estimated harmonics properties (spectral and temporal width) for different grating pair configurations can be found in appendix C as preliminary guidance for future experiments.

Chapter 7

Experiments with a single filtered harmonic

7.1 Introduction

With the synchronization of the VUV pump and IR probe implemented, experiments with a monochromatic VUV source can be conducted on targets of interest. In this chapter we will demonstrate experiments on the gas phase D_2 molecule using a single harmonic as the pump pulse.

The hydrogen atom is the simplest element in nature, consisting of one electron and one proton. The study of the hydrogen atom is essentially the foundation of quantum mechanics. It reveals the quantization of observables such as energy and angular momentum on the atomic scale. Since the non-relativistic Schrödinger equation of this two body system can be solved exactly, by comparison with experimental results, the validity of quantum mechanics can be checked at a precision level where the relativistic effects can be neglected. By adding an electron we move to the next system, the helium atom, which consists of two electrons and one helium nucleus. This is the simplest system in nature where the electron-electron correlation is included. An understanding of the helium atom can be a crucial starting point

for studying the solid state where electron correlation is a fundamental and common phenomenon. The next more complicated system is the hydrogen molecule, a four body system consisting of two electrons and two protons. The motion of the two protons introduces extra degrees of freedom. The total energy and total angular momentum of the system is now shared between electrons and two protons. It is this sharing that determines the chemical properties of matter. The study of the hydrogen molecule provides important information to understand the underlying mechanisms of chemical reactions, which is the major motivation of this project. We utilize our table-top vacuum ultraviolet light source to activate the valence electron of the simplest molecule D_2 via photo-excitation or photo-ionization. The VUV-light source retains temporal coherence (∼100 fs) and narrow bandwidth (∼200 meV) allowing dynamic and spectroscopic study of small molecules with the pump-probe method. The twofold simplicity of the project, namely the simple molecular target and the compact VUV light source, can essentially provide guidance for photochemical reaction studies for bigger molecules with more sophisticated experimental techniques in future. In the following experiments, a single order harmonic with photon energy near the first ionization threshold of D_2 (15.4 eV) is combined with a delay adjusted IR beam for a pump-probe study of the neutral deuterium molecule. We mainly focus on the dissociative ionization channel, which corresponds to the bond breaking process: $D_2 + \hbar\omega \rightarrow D{+}D^+ + e^-$.

7.2 Dissociative ionization study of the D_2 molecule with the 11th harmonic as a pump

7.2.1 Experimental result

Figure 7.1 shows the photoelectron spectra of an argon target exposed to the 11th harmonics at two different focal positions. In principle, the photon energy of the normal 11th harmonic is: 11×1.54 eV $= 16.94$ eV. The central wavelength of fundamental laser field is calibrated

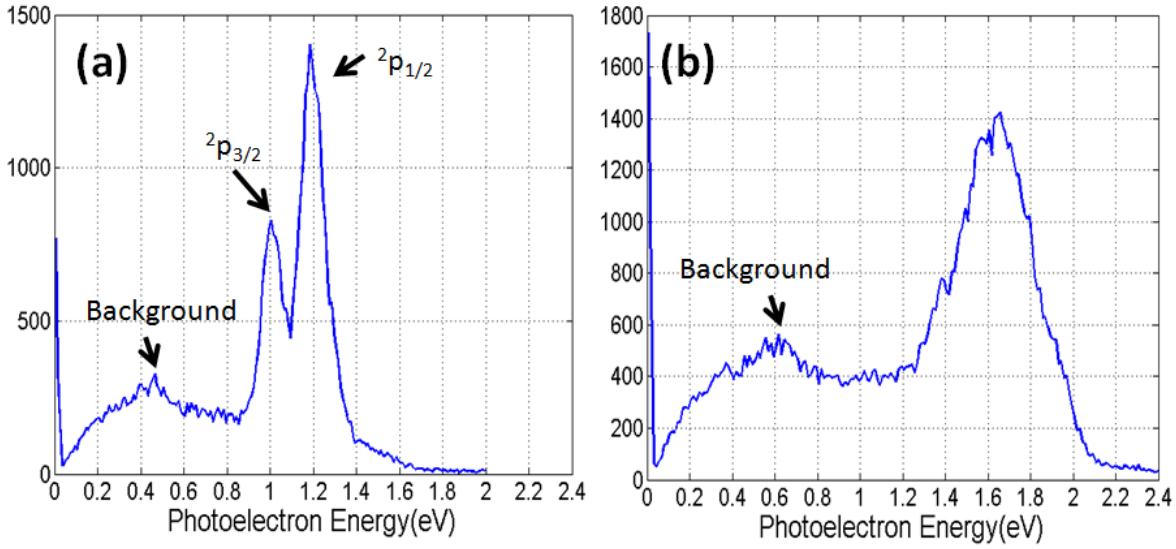

Figure 7.1: Photoelectron spectrum of argon from the 11th harmonic. (a)Driving laser focal position is outside the gas cell, (b)driving laser focal position is inside the gas cell. The signals underneath the major peaks are mainly background.

as 802 nm, this is implemented by monitoring the central wavelength of the second harmonic signal generated by focusing the fundamental field onto a barium borate oxide (BBO) crystal. However, as demonstrated in chapter 4, high order harmonics photon energies can be tuned by changing the optical geometry of the driving laser pulse such as the focal position with respect to the exit of the semi-infinite gas cell, and the size of the aperture used before the entrance of the cell (i.e. clipping the laser beam). When the focus of the driving laser is outside of the cell (indicating a weak intensity region) the high harmonic has a lower photon energy (shown in Fig. 7.1(a)). The double peak structure is due to the spin-orbit splitting of the ionic state $Ar^+ {}^2P_{1/2}$ ($I_P = 15.76$ eV) and $Ar^+ {}^2P_{3/2}$ ($I_P = 15.93$ eV). The 11th harmonic in this case possesses a photon energy of 16.95 eV with a bandwidth of about 100 meV. Under this condition, the high harmonic generation favours the short trajectory. When the focal position is moved inside the cell, the high order harmonic photon energy is shifted to shorter wavelengths with a mean photon energy of about 17.45 eV as shown in Fig. 7.1(b). The bandwidth of the harmonic is broadened such that the spin-orbit splitting structure is not resolvable any more. This is due to the fact that the phase matching condition for a

single electron trajectory of HHG can not be fulfilled because of the increased interaction length, and the higher effective laser intensity induces significant plasma-driven non-linear effects. Therefore, a mixture of both long and short trajectories of HHG as well as frequency shifting and broadening are expected. We thus demonstrate a monochromatic VUV source with tunable photon energy from 17.0 eV to 17.5 eV (which are actually the lower and upper limits under our experimental conditions, respectively). Although the blueshifted 11th harmonic shows a rather broad bandwidth (∼300 meV), in a pump-probe experiment where both VUV and IR are required the size of the IR focus limits the effective bandwidth of VUV participating in the interaction. As mentioned in chapter 6.6, the spatial chirp of the VUV introduced by the grating pair is 0.6 mm/eV. This indicates that the VUV focal spot with 300 meV bandwidth can be stretched to 0.18 mm. However, the size of the IR is less than 0.1 mm at the focus, thus limiting the effective bandwidth of the VUV in a pump-probe experiment to be no more than 170 meV.

The 11th harmonic VUV photon alone is sufficient to singly ionize the D_2 molecule (I_P = 15.4 eV) producing D_2^+, however it cannot produce the D^+ fragments because it is energetically forbidden (the D(1s)+D^+ dissociation limit is 18.15 eV). In order to open the dissociative ionization channel in the D_2 molecule, additional IR photon(s) will be required to surpass the dissociation limit of 18.15 eV. We thus introduce an IR pulse (802 nm) combined with the 11th harmonic VUV pump to investigate the dissociative ionization process in D_2. The IR probe intensity is attenuated by a neutral density filter to $< 2 \times 10^{12}$ W/cm^2, so that the IR alone can hardly produce D^+ fragments, ruling out the possibility of dissociative ionization induced by the IR probe beam. We first let the IR arrive after the VUV pulse (∼9000 fs), and use both the VUV photon energy and the polarization of the IR as knobs to alter the dissociative ionization process. Figure 7.2 shows the momentum distribution of D^+ using the lower energy VUV photon (17.0 eV) as the pump. Two polarization configurations are utilized, i.e. the parallel and perpendicular configurations, which correspond to the IR polarization direction parallel and perpendicular to that of the VUV beam, respectively.

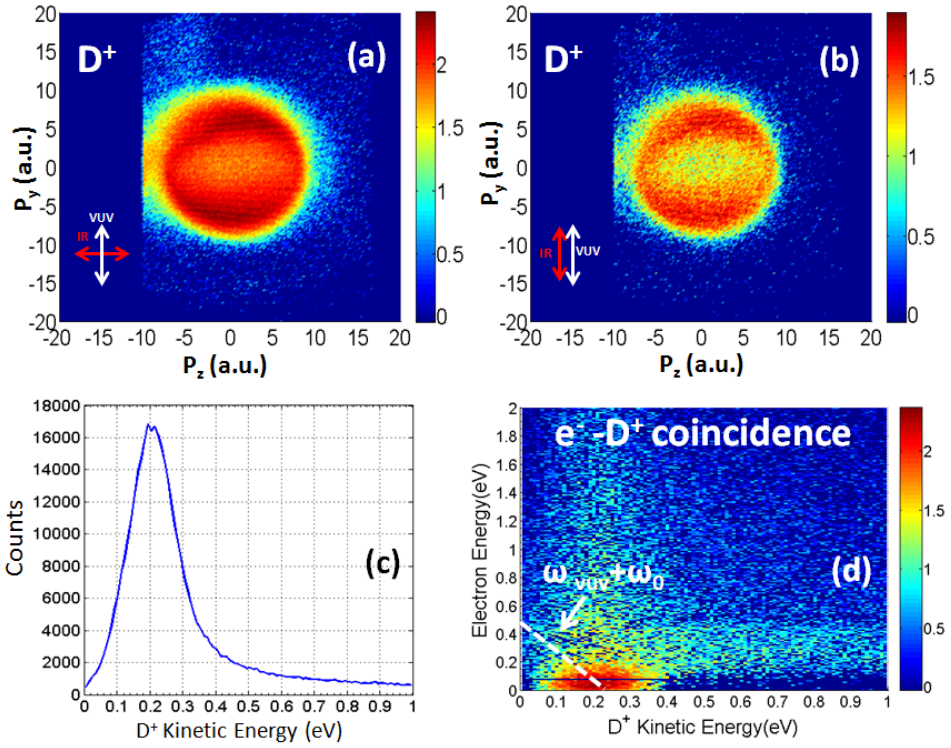

Figure 7.2: Dissociative ionization measurement with the 11th harmonic source in Fig. 7.1 (a) (17.0 eV) as the pump . (a) D^+ momentum distribution with the IR polarization direction parallel to the VUV polarization direction (logarithmic scale). (b) D^+ momentum distribution with the IR polarization direction perpendicular to the VUV polarization direction (logarithmic scale). (c) Kinetic energy of D^+ fragments. (d) D^+ and e^- energy correlation map (logarithmic scale). Note that the kinetic energy spectrum of D^+ and the D^+ and e^- energy correlation map are almost identical for the two polarization configurations. We choose only the perpendicular polarization configuration case to plot out (c) and (d).

The two dimensional momentum distribution of D^+ under two different polarization configurations shows almost identical patterns: a hollow shell structure with most of the signals concentrated along the VUV polarization direction. Thus we conclude that the dissociation direction is independent of the direction of polarization of the IR probe. The D^+–e^- coincidence measurement is also performed where both the electron and D^+ from the same D_2 molecule are recorded simultaneously (check appendix B for detailed procedure of data analysis). The energy correlation map between D^+ and an electron is plotted in Fig. 7.2(d).

The IR-assisted dissociative photoionization of D_2 by the 11th harmonic can be written

as: $D_2 + \hbar\omega_{11} + N\hbar\omega_0 \rightarrow D + D^+ + e^-$, where N is the number of IR photons involved in this process. The energy conservation law indicates that: $E_{e^-} + E_D + E_{D^+} = \hbar\omega_{11} + N\hbar\omega_0 - E_{diss} = constant$, where $E_{diss} = 18.15$ eV is the dissociation limit into $D(1s) + D^+$. The experimental data shows only the $N = 1$ channel with the electron carrying almost zero energy.

We then applied the blueshifted 11th harmonic (17.45 eV) to perform a similar experiment. The measurements are shown in Fig. 7.3. Surprisingly, two channels are observed in the momentum distribution of D^+: an outer shell with dissociation events concentrated along the IR polarization direction and an inner shell that solely follows the VUV polarization direction. The D^+ and e^- energy correlation map (Fig. 7.3(d)) proves that both channels absorb one VUV photon and one IR photon.

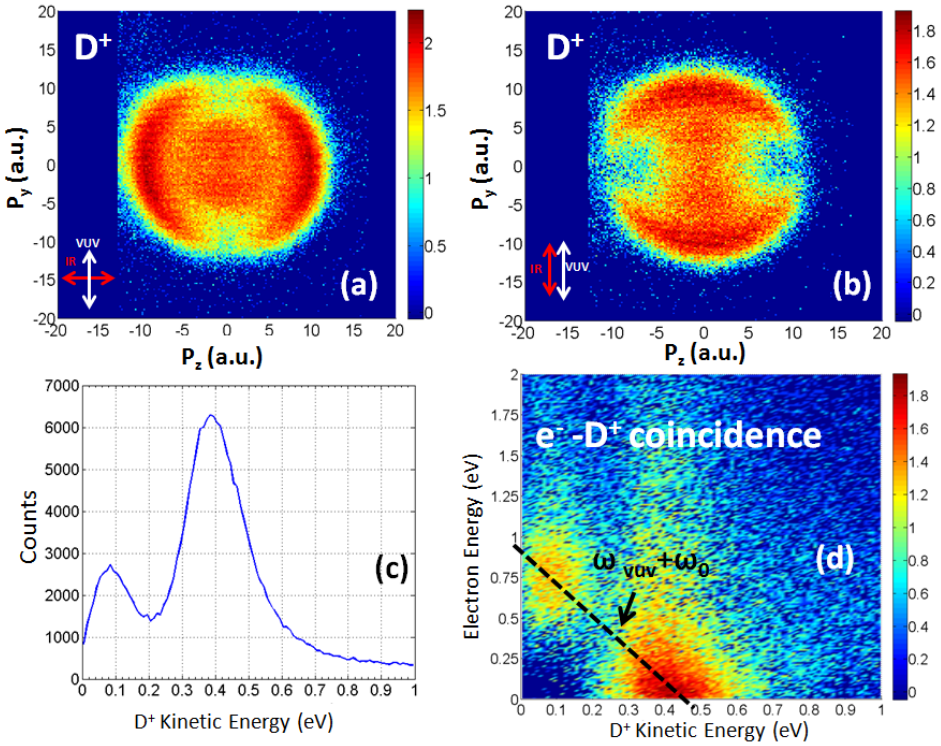

Figure 7.3: Same as Fig.7.2 but with the 11th harmonic source in Fig. 7.1(b) (17.45 eV) as the pump.

7.2.2 Interpretation

Since the VUV and IR pulses are well separated in time, the whole reaction can be treated as a two step process–the absorption of a single VUV photon followed by the absorption of a single IR photon. We need to determine the states that can be involved in this process.

First, lets consider the initial state of D_2 molecules in our experiment. The translational temperature of the effusive gas jet used in the experiment can be measured by fitting the velocity distribution of the center of mass (CM) of D_2^+ with the Boltzmann distribution. The typical CM velocity is associated with a temperature of a few tens of Kelvins along the jet direction (a few Kelvin perpendicular to the jet direction). We assume that the vibrational and rotational temperatures of the molecule (D_2 in this case) are in equilibrium with the translational temperature. At 30 Kelvin the thermal energy is only 2.5 meV, which is rather small compared to the vibrational level spacing (about 0.3 eV) on the ground electronic state of D_2. Therefore, higher vibrational states are not accessible. As for the rotational part, the rotational energy levels is $E_J = B(J+1)J$ with $B = 29.9$ cm^{-1} denoting the rotational constant, where J is the rotational quantum number. The deuterium contains one proton and one neutron, and possesses a spin of 1 (boson). This indicates the total nuclear spin of D_2 molecule can be I = 0, 1, 2. The total wavefunction is symmetric under the nuclear exchange in D_2 molecule. For symmetric nuclear spin wavefunction associated with $I = 0$, 2 (*ortho*-D_2), the rotational wavefunction with even J are required. Similarly, for antisymmetry spin states with $I = 1$ (*para*-D_2), odd J will be required. According to the nuclear spin multiplicity, we assume that the deuterium molecule is composed of 2/3 *ortho*-D_2 and 1/3 *para*-D_2. Then the statistical distribution of rotational energy levels following the Boltzmann distribution $P = \exp -\frac{E_J}{kT}$ can be calculated as: 97.3% for $J = 0$, and 2.7% for $J = 1$. Therefore under our experimental condition the deuterium molecule is initially on the ground electronic state, $X^1\Sigma_g^+$, with $v = 0, J = 0$, where v represents the vibrational quantum number.

Next we consider the intermediate states. The symmetries of these states promoted by

the VUV photon can be determined by the electric dipole selection rules:

(1) electronic parity will change because the electric dipole operator has odd parity $g(u) \rightarrow u(g)$.

(2) total electron spin remains the same since the electric field does not couple different spin states $\Delta S = 0$.

(3) the total angular momentum is conserved with photon carrying one unit of angular momentum. Therefore $\Delta\Lambda = 0, \pm 1$, $\Delta J = 0, \pm 1$, but $J = 0 \nrightarrow J = 0$, where Λ is the projection of the total electronic orbital angular momentum onto the molecular axis.

(4) for $\Delta\Lambda = 0$, additional selection rules apply for a $\Sigma \rightarrow \Sigma$ transition: $+/- \rightarrow +/-$, where $+/-$ refers to the reflection symmetry of the electronic wavefunction about the plane including the molecular axis.

By absorbing a single VUV photon, electronic states with $^1\Sigma_u^+$ and $^1\Pi_u$ symmetry can be populated. Partial related potential energy curves (PECs) for D_2 and D_2^+ are shown in Fig. 7.4. According to the PECs a single VUV photon with photon energy of 17.0 eV (Fig. 7.2) can directly ionize the molecule into the $1s\sigma_g$ cation state, or excite the molecule onto states of the neutral molecule which correlate to the Rydberg series $D(1s) + D(4l)$ (dissociation limit is 17.3 eV) with odd parity. In the latter case, the excited states are lying above the ionization threshold of D_2 (15.4 eV), thus are termed as the super-excited states first introduced by Platzman [110]. Therefore, there are two possible dissociative ionization pathways after introducing a second IR photon, namely dissociative ionization via direct ionization [discussed in section 7.2.2 (a)] and dissociative ionization via super-excitation [presented in section 7.2.2 (b)].

a) Dissociative ionization via direct ionization

A very straightforward dissociative ionization pathway is that the VUV photon can directly access the ground electronic state $1s\sigma_g$ of D_2^+, then an additional IR photon can fragment the cation energetically. The VUV and IR are well separated in time; the dissociation along

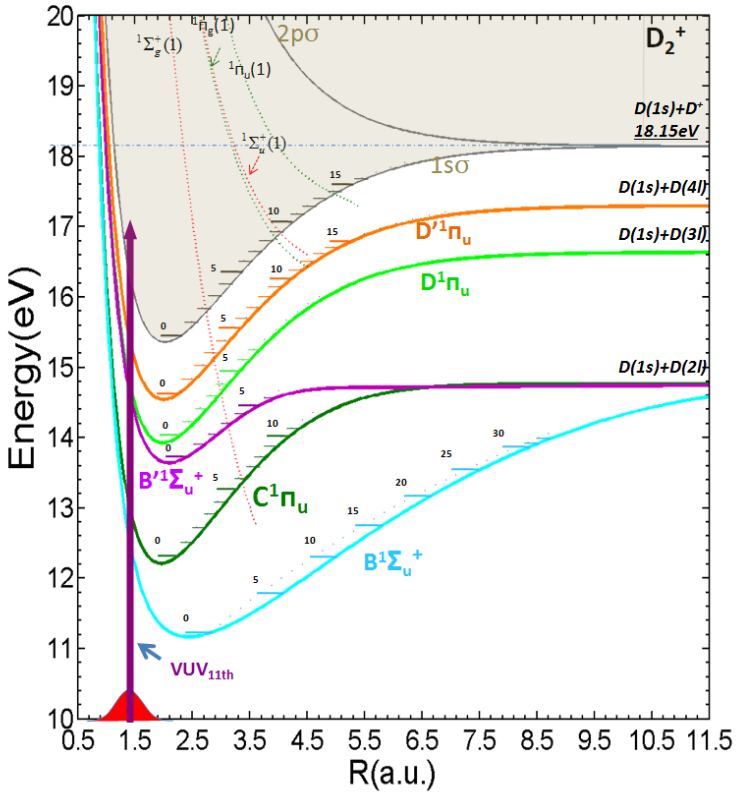

Figure 7.4: D_2^+ and D_2 potential energy curves. The purple arrow indicates the 11th harmonic photon energy. The dotted lines represent the lowest doubly excited states of the corresponding symmetry. The single excited states potential energy curves are adapted from [111] and references therein. The doubly excited states potential energy curves are adapted from [112].

the $1s\sigma_g$ state is almost impossible since a $1s\sigma_g$ to $1s\sigma_g$ transition is dipole forbidden. Thus, we conclude that the dissociation can only occur by electronic excitation onto the repulsive $2p\sigma_u$ curve, which is the so-called bond-softening (BS) process [113, 114]. The dissociation dynamics of the BS process can be well depicted by the dressed state Floquet picture [115], where the potential energy curves are shifted up and down by different numbers of photons to take into account the time-dependent interaction between the molecule and electric field.

Figure 7.5 shows the calculated diabatic and adiabatic dressed state PECs of D_2^+ for a net one photon process. The diabatic Floquet picture (blue line in Fig. 7.5) corresponds to the weak field limit (laser intensity $I \to 0$). It indicates that the dissociation will most

likely take place at the crossing point between the two dressed states where $v = 13$ for $1s\sigma_g$. However, in reality the laser field has a high intensity that will couple channels dressed by different photon numbers together. The adiabatic Floquet picture (red lines in Fig. 7.5) is required to represent the dissociation process properly. The adiabatic potential curves are calculated by diagonalizing the Floquet D matrix, which leads to the avoided crossing if the diabatic potential curves are coupled at the crossing point.

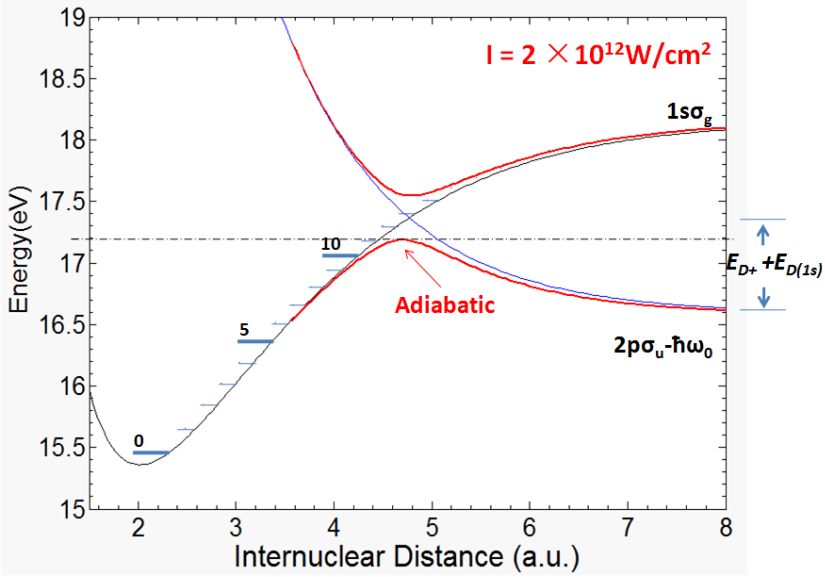

Figure 7.5: The photon dressed potential energy curves of D_2^+. Both the diabatic and adiabatic PECs are shown for comparison. Laser central wavelength $\lambda_0 = 802$ nm.

In order to ensure that dissociation occurs the vibrational wavefunction energy has to surpass the barrier formed by the avoided crossing of the adiabatic PECs. The lowest dissociative vibrational state is $v = 11$ (17.2 eV) when the IR intensity is 2×10^{12} W/cm^2 (this value is the upper limit of the laser intensity since it is calculated from the geometrical parameters of the laser and is overestimated as discussed in chapter 3). The corresponding kinetic energy of D^+ will be $E_{D^+} = 0.3$ eV, which is the lower limit of kinetic energy of D^+. The upper limit of E_{D^+} is 0.45 eV. Thus the BS mechanism requires a minimum photon energy of 17.2 eV and the corresponding kinetic energy of D^+ is 0.3 eV to 0.45 eV. Another feature of the BS process is that the dissociation is preferentially along the IR polarization

direction [114], where the effective intensity applied to the Floquet picture is maximum resulting in a larger dissociation probability.

Based on the arguments above, we can conclude that in the case of lower VUV photon energy (Fig. 7.2) no dissociative ionization occurs via the direct-ionization mechanism since it is energetically forbidden. A different mechanism has to be invoked to interpret the observed D^+ signal which follows the VUV polarization direction with very low kinetic energy. In the case of the higher VUV photon energy (Fig. 7.3), the BS channel is energetically opened. The outer ring in the D^+ momentum spectrum corresponds to a kinetic energy of ∼0.38 eV, and this dissociation channel follows the IR polarization direction under both polarization configurations. Thus we interpret the outer momentum shell for the 17.5 eV photon case to be due to the BS process. As for the inner part in the D^+ momentum distribution shown in Fig. 7.3, the dissociation of the very slow fragments ($E_{D^+} = 0.2$ eV) follows the VUV polarization direction regardless of the IR polarization direction. This behavior is similar to the case shown in Fig. 7.2 and thus is likely caused by a similar mechanism.

b) Dissociative ionization via super-excitation

While the molecule is exposed to photons with photon energies greater than the first ionization threshold, the molecule is not necessarily ionized directly. Other processes can compete with the direct ionization mechanism. For instance, singly excited Rydberg states of D_2 can be populated through electronic excitation. These states are termed as super-excited states as suggeseted by Platzman [110] and have been studied extensively [116–123]. If the photon energy is large enough, doubly excited states (DES) are directly accessible. The molecule can either dissociate into two neutral atoms or auto-ionize into the singly charged ionic states [124–127]. However, with a photon energy of 17.0–17.5 eV in our experiment, the DES can not be populated from the ground electronic state of D_2. Thus we only focus on the dissociative ionization products with the super-excited states as the intermediate states.

The predissociation of super-excited states in the hydrogen molecule induced by nonadiabatic coupling has been reported previously [116, 119]. With a photon energy of 17.0 eV, the singly excited electronic states corresponding to $\mathrm{D}(n=1)+\mathrm{D}(n=4)$ dissociation limit can be resonantly populated into a vibrationally excited state on the $4p\pi D'\ ^1\Pi_u$ PEC. These states can be coupled onto the continuum of the series associated with the $\mathrm{D}(n=1)+\mathrm{D}(n=3)$ dissociation limit ($D\ ^1\Pi_u$ for instance), and then predissociate into two separated atoms: $\mathrm{D}(n=1)+\mathrm{D}(n=3)$. If an IR photon is introduced at a later time, the excited $\mathrm{D}(n=3)$ atom can be photoionized producing D^+. Since the predissociation process is irrelevant to the IR pulse, the dissociation direction is expected to be independent of the IR polarization, which is consistent with our experimental observation in Fig. 7.2. Furthermore, the binding energy of the $\mathrm{D}(n=3)$ atom is 1.51 eV. If the predissociation mechanism is correct, the kinetic energy of the associated electron for a 802 nm photon will be $E_{e^-} = 1.54 - 1.51 = 0.03$ eV, which is consistent with the experimental result in Fig. 7.2(d) within the system resolution. Thus, the dissociative ionization with lower photon energy (17.0 eV) is likely due to the predissociation of the super-excited state. A similar argument can be applied to the higher VUV photon energy (17.5 eV) case in Fig. 7.3. With photon energy of 17.5 eV, the vibrationally excited states in PECs with $\mathrm{D}(n=1)+\mathrm{D}(n=5)$ dissociation limit can now be populated. These states can be coupled onto the continuum of the series associated with the $\mathrm{D}(n=1)+\mathrm{D}(n=4)$ dissociation limit. The $\mathrm{D}(n=4)$ atom has a binding energy of 0.85 eV, so the released electron will carry a kinetic energy of $E_e = 1.54 - 0.85 = 0.69$ eV after absorbing an IR photon. The measured electron kinetic energy has a mean value of 0.75 eV (Fig. 7.3(d)). The small discrepancy might come from the system resolution due to the fact that the calibration of the electron energy is very sensitive to the potential applied on the effusive jet needle. To confirm the validity of the predissociation mechanism, we used a slightly different VUV photon energy (17.4 eV) to perform the same experiment. Figure 7.6 shows the D^+ and e^- energy correlation map using the VUV with this intermediate photon energy (17.4 eV). Compared with Fig. 7.3,

the lower kinetic energy peak feature of D^+ is shifted down to 0.05 eV and becomes almost structureless. However, the associated electron energy remains at the same mean value (0.75 eV). This indicates that the electron is indeed coming from an atomic fragment.

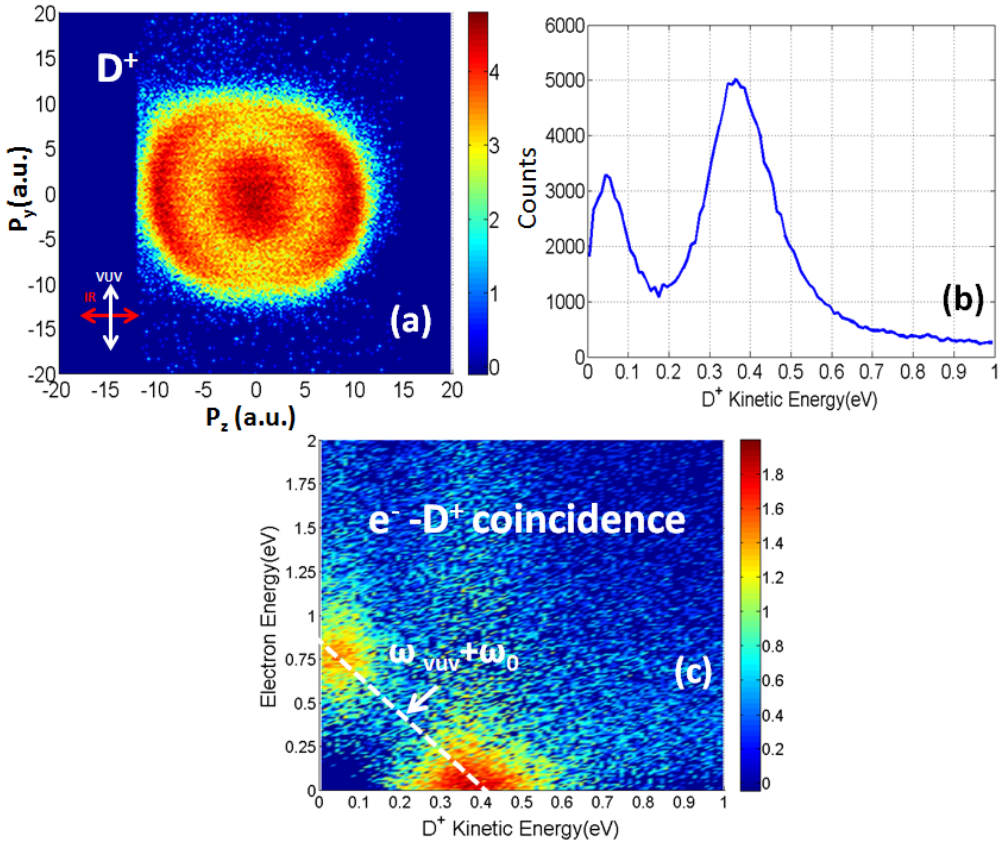

Figure 7.6: Dissociative ionization measurement with 11th harmonic (17.4 eV) as the pump. (a) D^+ momentum distribution with IR polarization direction perpendicular to VUV polarization direction (logarithmic scale). (b) Kinetic energy of D^+ fragment. (c) D^+ and e^- energy correlation map (logarithmic scale).

The experimental results show that the dissociation direction associated with the super-excited states is mainly along the VUV polarization direction. This suggests that, the VUV photon excitation is predominantly by a parallel transition, where $\Delta\Lambda = 0$. The intermediate super-excited state should therefore possess a $^1\Sigma_u^+$ symmetry. In the photon energy range used in our experiement (17.0 – 17.5 eV), many Rydberg series $np\sigma^1\Sigma_u^+$ with $n > 4$ are overlapping, which makes it very complicated to identify the dominant channel(s)

contributing to the predissociation process.

Another aspect of predissociation is the lifetime of the corresponding excited state promoted by the 11th harmonic pulse. It is worthwhile to investigate how long it takes for the resonantly excited states of the neutral to predissociate into one ground state atom and one excited atom. Figure 7.7 shows the delay-dependent D^+/D_2 ratio. This ratio shows an enhancement when the IR pulse arrives after the VUV pulse, and it saturates at about 2000 fs delay when most of the super-excited state population has predissociated. By fitting the curve with a Gaussian integral, the lifetime of the predissociation is estimated to be about 1080 fs. The predissociation yield and natural linewidth from selected super-excited states of H_2 are well documented [119,128]. The corresponding dissociative lifetime is associated with the linewidth by the uncertainty principle: $\frac{\Delta t \Delta \omega}{2\pi} = 0.44$ (assuming a Gaussian line shape). The lifetime of different excited states that decay via predissociation can be very different. For instance, the D' $4p\pi^1\Pi_u^+$ state has a typical lifetime of 1500 fs (10 cm^{-1} linewidth) for $v > 9$ in H_2, the lifetime of $5p\sigma^1\Sigma_u^+$ is as long as 25 ps (0.6 cm^{-1} linewidth) for $v = 9$ in H_2 but is only 60 fs (250 cm^{-1} linewidth) for $v = 10$. However, these known states are not good candidates to match our experimental results. Further spectroscopic measurements with high resolution and sophisticated theoretical calculation will be required to identify the participating channels.

7.2.3 Conclusion

The dissociative ionization of the D_2 molecule has been studied with a monochromatic VUV source around 17 eV (11th harmonic) as the pump and a weak IR laser pulse as the probe. Two distinct dissociation mechanisms have been observed via the VUV+IR two photon process. One involves the so-called bond-softening mechanism. Specifically, a singly charged ionic state $1s\sigma_g$ with vibrational quantum number $v \geq 11$ is populated by the VUV photon followed by electronic excitation onto the repulsive $2p\sigma_u$ curve. This channel can be opened with VUV photon energy greater than 17.2 eV, and the dissociation direction

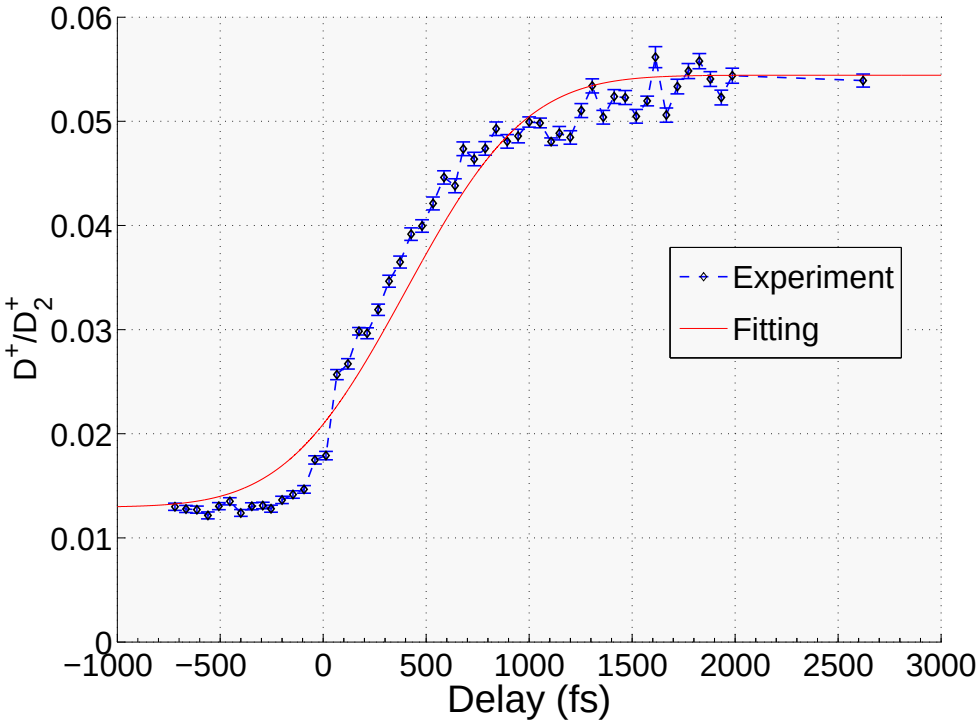

Figure 7.7: D^+/D_2 ratio as a function of the VUV-IR delay. Zero delay means VUV and IR are overlapping with each other. Positive delay means VUV is preceding the IR pulse. The red curve is a fitting with the integral of a Gaussian function : $\int_{-\infty}^{\tau} dtA\exp(\frac{(t-\tau_0)^2}{T^2})$+B, where A and T are the amplitude and width of the Gaussian function, τ is the VUV-IR delay, and B, τ_0 are offsets along the vertical and horizontal axis. T is 650 fs in the fitting.

is along the IR polarization direction. The second dissociation mechanism is caused by the predissociation of super-excited states. Depending on the VUV photon energy, singly excited states above different dissociation limits D($n = 1$)+D($n = 3, 4$) can predissociate via nonadiabatic couplings producing one ground state D(1s) and one excited D($n = 3, 4$) atom. A delayed IR pulse can then photoionize the excited atom. The dissociation of this channel follows the VUV polarization indicating a parallel transition induced by the VUV. However, due to the complicated mixture of different Rydberg series at this photon energy we can not yet identify the dominant state(s) that are contributing to the process. This experiment demonstrates the modification of dissociative ionization channels using the VUV

photon energy and the polarization of the IR as control knobs.

7.3 Dissociative ionization study of D_2 molecule with the 9th harmonic as a pump

7.3.1 Experimental result

In the next experiment, we choose the 9th harmonic as the pump beam to interact with hydrogen molecules. The 9th harmonic has a photon energy close to 14 eV, which is lower than the first ionization potential of most rare gas atoms. Therefore, the photoelectron spectrum (PES) is not directly available for the VUV spectrum characterization. Instead, we took the PES of its neighboring order, the 11th harmonic, to deduce the 9th harmonic spectrum indirectly. It is based on the assumption that the adjacent harmonics have very similar bandwidth and are separated by 3.08 eV for an 802 nm driving laser. Figure 7.8 is the typical PES of argon gas from the 11th harmonic. The two peaks correspond to the spin-orbit splitting of the ionic state $Ar^+ \ ^2P_{1/2}$ ($I_P = 15.76$ eV) and $Ar^+ \ ^2P_{3/2}$ ($I_P = 15.93$ eV). The 11th harmonic has a photon energy of 17.0 eV with a bandwidth less than 200 meV, which indicates that the 9th harmonic is centred around 13.92 eV with a bandwidth smaller than 200 meV. Note that in a pump-probe experiment, the effective bandwidth of the VUV will be limited by the beam size of the IR probe at the focus. For an IR probe with diameter of $\sim$100 μm the VUV bandwidth synchronized with IR will be 170 meV.

The deuterium molecule is in its ground electronic state $X \ ^1\Sigma_g^+$ with initial quantum numbers $v = 0, J = 0$, following the same argument as in the previous section. The excited state will be a singlet state with u symmetry. Figure 7.9 shows the adiabatic potential curves of D_2 that are involved, where zero energy is defined as the energy of the lowest vibrational state of $X \ ^1\Sigma_g^+$ of D_2.

For the 9th harmonic with a photon energy close to 14 eV, the molecule can only be

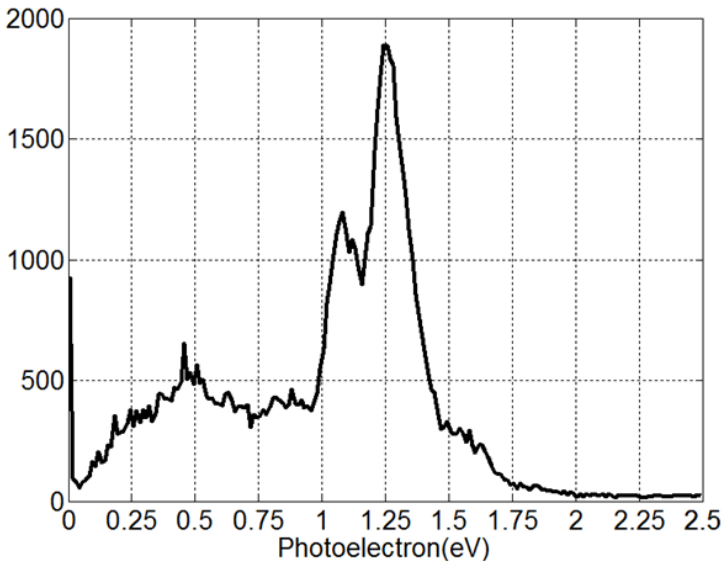

Figure 7.8: Photoelectron spectrum of argon ionized by the 11th harmonic. The signals underneath the major peaks are mainly background.

excited via a electronic excitation to the singlet B, C and B' states. D_2^+ and D^+ ion fragments can barely be detected with only the 9th VUV pump present. In the next step, a weak IR probe (with an intensity below 2×10^{12} W/cm^2) will be introduced to fragment the molecule prepared by the VUV pump. Figure 7.10 is a typical time of flight spectrum of deuterium ions collected under the condition, where IR and the 9th harmonic are both present. The production of D_2^+ signal corresponds to the excitation of D_2 followed by single ionization by the IR probe pulse. Although the IR alone can hardly ionize the D_2 from the $X\ ^1\Sigma_g^+$ ground state with a first ionization potential $I_P = 15.4$ eV, it is a rather intense field experienced by the excited electron on the B, C and B' states ($I_P = 1.5$ eV) and can easily strip the excited electron. This is a very dominant channel since one additional IR photon can liberate the excited electron and leave the system on the $1s\sigma_g$ cation state. The D^+ fragments are most likely from dissociative ionization as double ionization of D_2 is very unlikely due to the requirement of too many IR photons to reach the dication curve. A minimum of three IR photon absorption is needed to reach above the D^++D dissociation limit (18.15 eV), and thus dissociative ionization becomes energetically accessible. Since more photons are

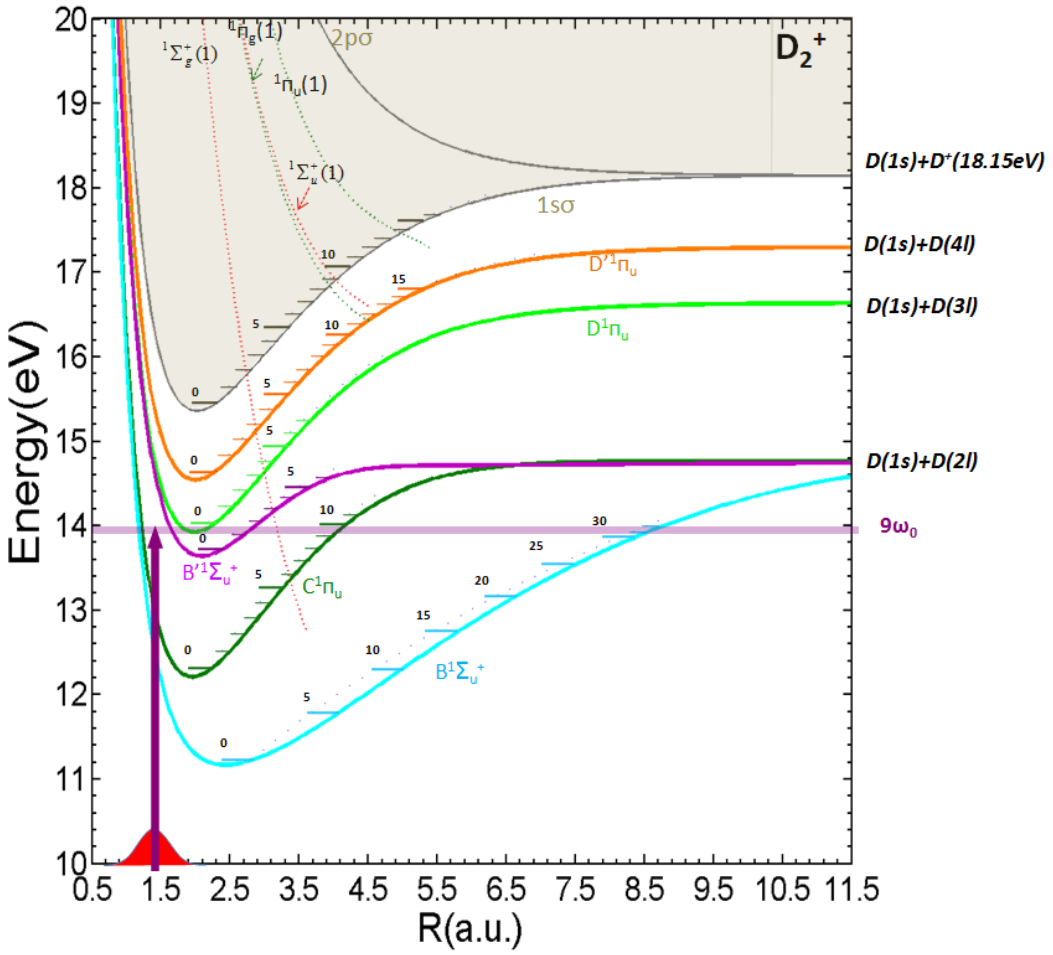

Figure 7.9: D_2^+ and D_2 potential energy curves. The purple arrow indicates the 9th harmonic photon energy. The dotted lines represent the lowest doubly excited states of the corresponding symmetry. The single excited states potential energy curves are adopted from [111] and references therein, The doubly excited states potential energy curves are adopted from [112].

required, dissociative ionization (D^+) is much weaker than direct ionization (D_2^+). Note that the D_2^+ signal has a broad background underneath the main peak. This includes the D_2^+ generated by the second diffraction order of 17th and 19th harmonic photons. The intensity of the second diffraction order of the 17th or 19th harmonic beam is more than an order of magnitude lower than that of the 9th harmonic beam. Furthermore, the 17th and 19th harmonics are not overlapping with the IR probe pulse spatially. Thus, their contributions to the D^+ signal is negligible.

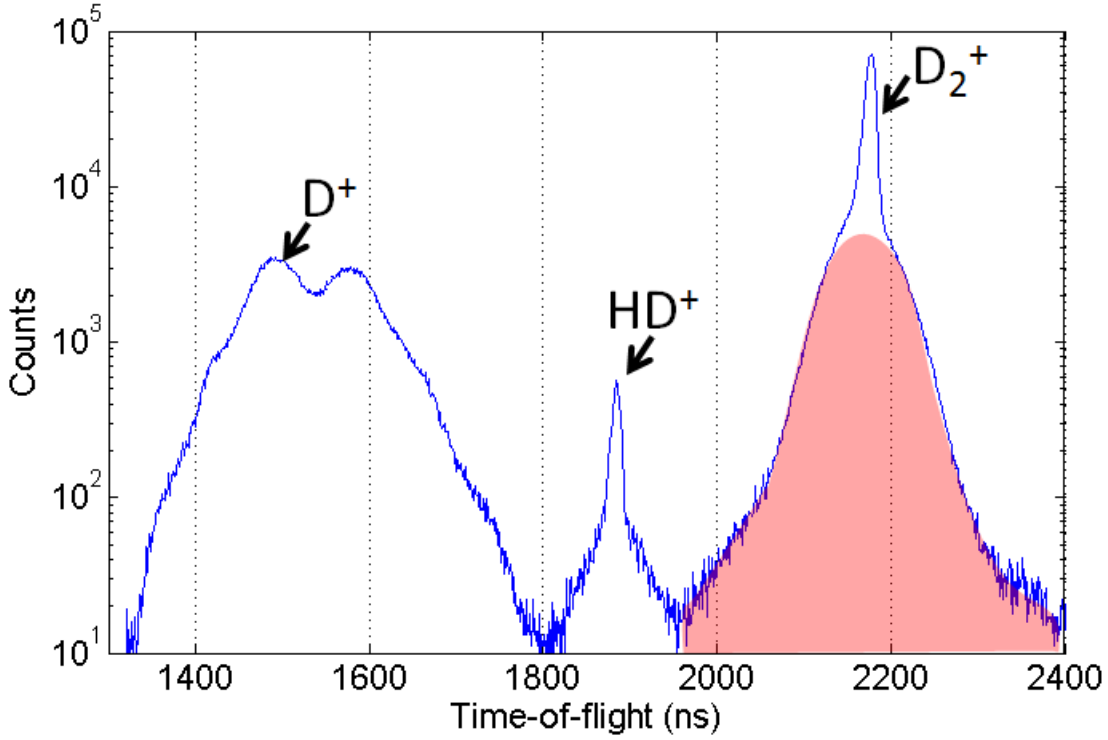

Figure 7.10: Time-of-flight spectrum of the deuterium ion with both IR and the 9th harmonic present. The broad red shading includes D_2^+ generated by the second diffraction order of the 17th and 19th harmonic photons.

A VUV-IR delay-dependent study of the IR-assisted VUV photoionization of D_2 is performed to provide dynamic information, and demonstrate the modification of the dissociative ionization process. Since the whole process can be treated as a VUV-exciting IR-ionizing two-step process, an orthogonal polarization configuration (i.e. the polarization of VUV is perpendicular to that of the IR pulse) is adapted on purpose to emphasize the impact of the IR probe on the process.

The two-dimensional momentum distribution, the associated kinetic energy of D^+ and the D^+/D_2^+ ratio are plotted as a function of VUV-IR delay are shown in Fig. 7.11. Since the delay stage has a travel range of 500 fs, we combined two sets of data (panels $t_0 - t_9$ and $b_0 - b6$, respectively.) to cover the whole time dependent reaction (∼800 fs). Negative delay indicates that the VUV is preceding the IR pulse. There are three aspects of the data

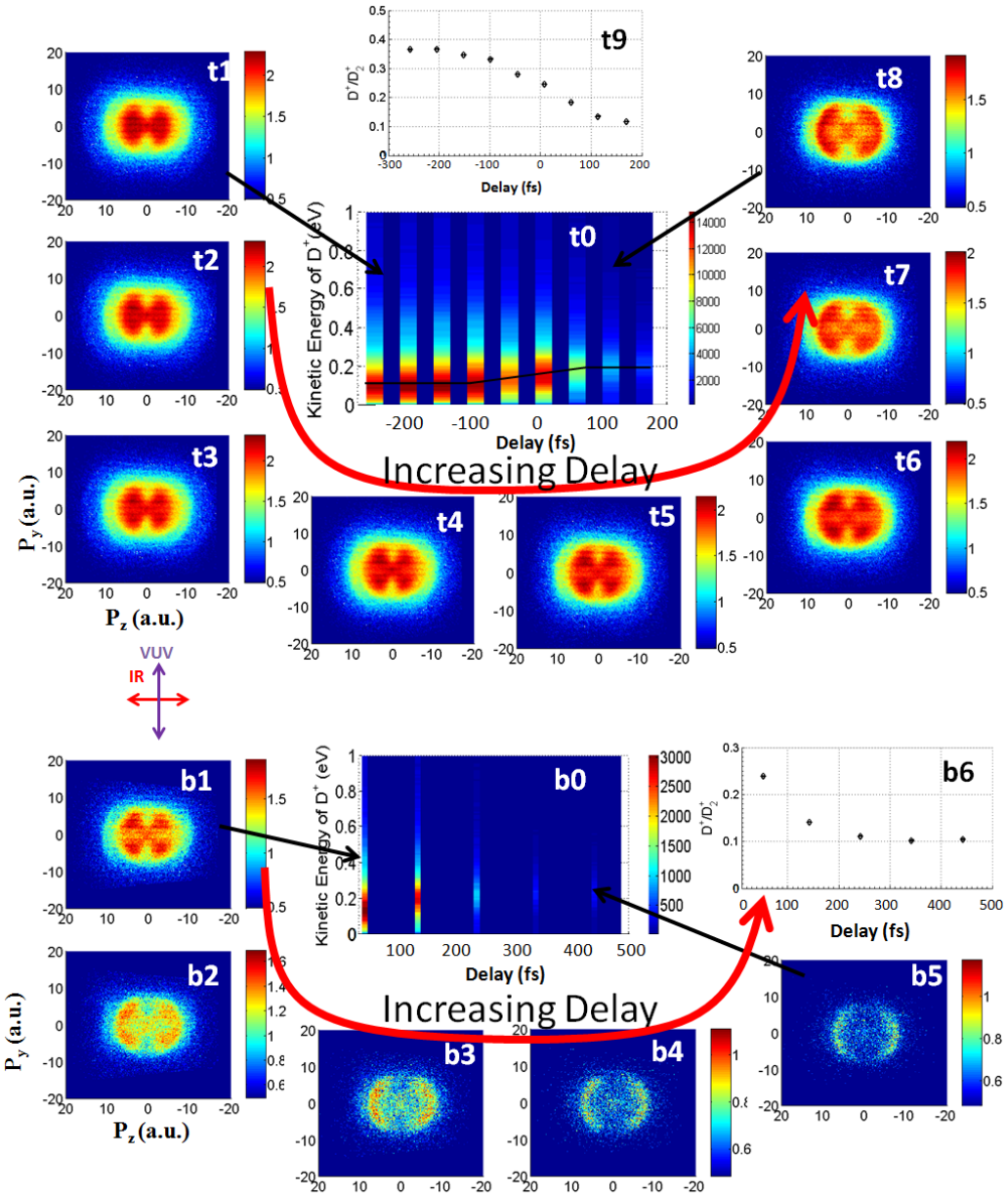

Figure 7.11: 2D momentum snapshots of D^+ (logarithmic scale) for different VUV-IR delays (t1–t8 and b1–b5). The big red arrows indicate the direction of the increase of the delay while the snapshots are taken. The top and bottom plots correspond to two different scans. The bottom scan is an extension of the top scan with the IR probe leading the VUV pump further. The central plots of both scans (t0 and b0) are kinetic energy distributions of D^+ as a function of delay (linear scale). The two 1-D plots correspond to the D^+/D_2^+ ratio as a function of delay for the two scans (t9 and b6). The polarization direction of IR and VUV pulses is also indicated.

that show delay-dependence.

Firstly, as the VUV pump is catching up with the IR probe (delay is increasing), the D^+/D_2^+ ratio is almost constant at earlier delays and then decreases rapidly like a step function with the step response smeared (Fig. 7.11(t9) and (b6)). The maximum D^+/D_2^+ ratio corresponds to an IR pulse following the VUV pulse, while the step response takes place when the VUV and IR are overlapping with each other. Since the step response is a convolution between the VUV (FWHM $\sim$ 100 fs) and IR (FWHM $\sim$ 50 fs) pulses, the D^+/D_2^+ ratio will change across a large delay range (a few hundred femtoseconds).

Secondly, a careful check of the kinetic energy of D^+ shows that the mean kinetic energy of D^+ is increasing from $\sim$0.1 eV to $\sim$0.2 eV as the delay is increasing [Fig. 7.11(t0) and (b0)]. The black solid line on top of the kinetic energy spectrum in Fig. 7.11(t0) shows the tendency of the delay-dependent change. It shows that the increase of the D^+ kinetic energy takes place with a 200 fs delay range, corresponding to a slope of 0.5 eV/1000 fs. Considering that the total kinetic energy release (KER) is twice the D^+ kinetic energy, the slope for KER change with delay is 1 eV/1000 fs. This is consistent with the dispersion of the VUV (1000 fs/eV) introduced by the grating pair (see section 6.6). Since the VUV pulse is chirped (longer wavelength is preceding the shorter wavelength), when the IR is swept across the temporal profile of the VUV pulse, the VUV frequency component that is synchronized with the peak of the IR will change. If the dissociative ionization process occurs when IR and VUV overlap, the photon energy of the VUV absorbed by the molecule changes with the delay, leading to an increase in KER of the $D+D^+$ fragmentation according to energy conservation. This effect can only take place as the IR and VUV have spatio-temporal overlap, and therefore the zero delay can be roughly defined at the time when the D^+ kinetic energy is 0.15 eV.

Lastly, the momentum distribution of D^+ shows three different patterns as the delay changes [Fig. 7.11(t1)–(t8) and (b1)–(b5)]. At small delays, the D^+ reveals a dumbbell structure aligned along the laser polarization direction. As the delay increases to the region

where VUV and IR are overlapping in time (where the KER change takes place), a horizontal nodal line shows up and the D^+ momentum evolves into a butterfly structure. As the delay is further increased, the butterfly pattern starts fading out and gets replaced by a dipole pattern.

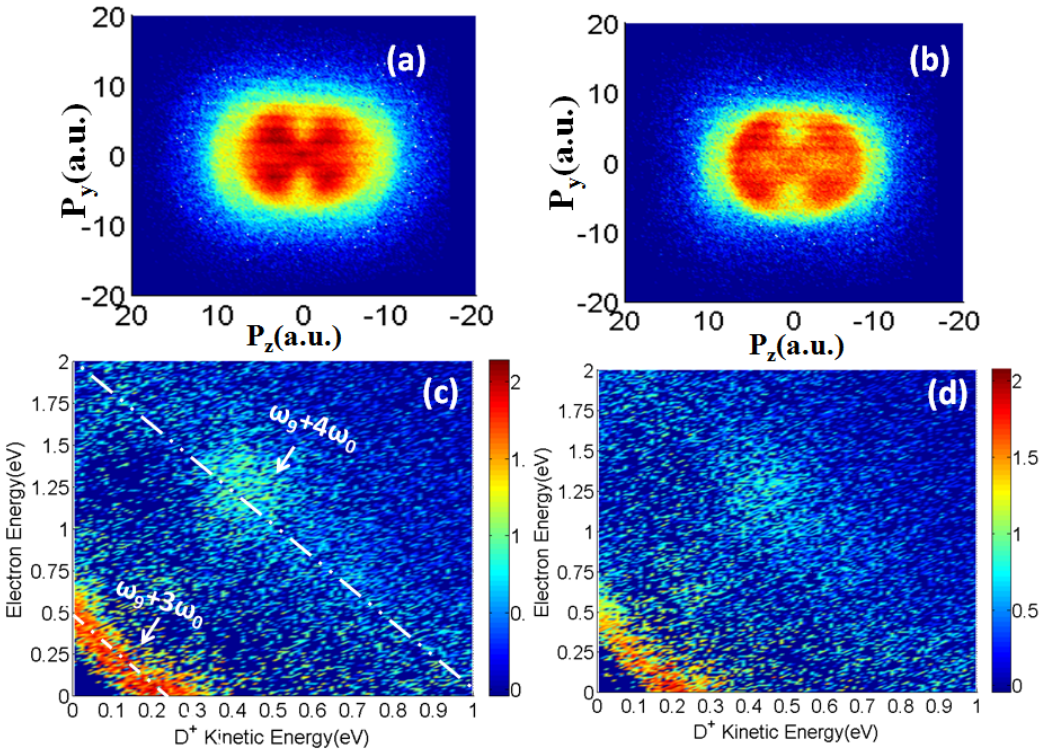

Figure 7.12: The e^- and D^+ energy correlation maps for two different delay regions (c and d), and the corresponding typical momentum distributions of D^+ (a and b).

The e^- and D^+ coincidence measurement is then performed to help identify the number of photons that participate in the process. Both the e^-–D^+ from the same D_2 molecule are measured simultaneously. For statistical reasons, we binned the data for a certain delay window together. Two e^- and D^+ correlation plots are shown in Fig. 7.12 corresponding to IR preceding VUV (Fig. 7.12(c)) and the time overlap region (Fig. 7.12(d)). The IR-assisted VUV photoionization has the process: $D_2 + \hbar\omega_9 + N\hbar\omega_0 \rightarrow D_2^+ \rightarrow D + D^+ + e^-$, where N is the number of IR photons involved in this process. The energy conservation law indicates that: $E_{e^-} + E_D + E_{D^+} = E_{e^-} + 2E_{D^+} = \hbar\omega_9 + N\hbar\omega_0 - E_{diss} = constant$, where $E_{diss} = 18.15$

eV is the $D(1s) + D^+$ dissociation limit. The experimental data shows that the majority group follows the $N = 3$ energy conservation line, namely $E_{e^-} + 2E_{D^+} = 0.45$ eV. There is also a minority group following the $N = 4$ energy conservation line, $E_{e^-} + 2E_{D^+} = 2$ eV with the D^+ kinetic energy of 0.4 eV. Note that there is a redistribution along the energy conservation line of the main group as the delay changes. However the main feature of the e^- and D^+ correlation plot, i.e the positions of the major and minor groups, does not depend on the delay. Thus the major action across the entire delay range involves a single VUV photon plus three IR photons.

7.3.2 Interpretation

In order to understand the delay-dependent momentum distribution of D^+ shown in Fig. 7.11, we first invoke possible mechanisms for producing D^+ with low kinetic energy <0.4 eV. As shown in Fig. 7.13, after excitation by the 9th harmonic (purple arrow) into a vibrational state on one of the PECs of the neutral discussed above, this state can be further ionized or excited by the IR probe beam (red arrows). Several pathways for this second step can lead to the dissociation into D^++D.

(1) The IR can promote the excited system to the continuum of the $1s\sigma_g$ state of D_2^+ followed by dissociation along the $1s\sigma_g$ potential curve. This is known as ground state dissociation (GSD) [129–131] and it requires a minimum of 3 IR photons.

(2) A doubly excited state (DES) with the allowed parity can be directly populated with 3 IR photons, and the doubly excited molecule can auto-ionize into the $1s\sigma_g$ cation state: $D_2^* + 3\hbar\omega_0 \rightarrow D_2^{**} \rightarrow D_2^+ + e^-$. producing vibrationally excited D_2^+, or leading to direct fragmentation of D_2^+ if the nuclei carries enough energy [132].

(3) The electron can be removed from the singly excited molecular state by IR probes, launching the molecule on a vibrationally excited state of the molecular ion on the $1s\sigma_g$ PEC. An additional IR photon can populate the $2p\sigma_u$ state via electronic excitation at the outer turning point of the $1s\sigma_g$ curve. The D_2^+ then fragments along the antibonding $2p\sigma_u$

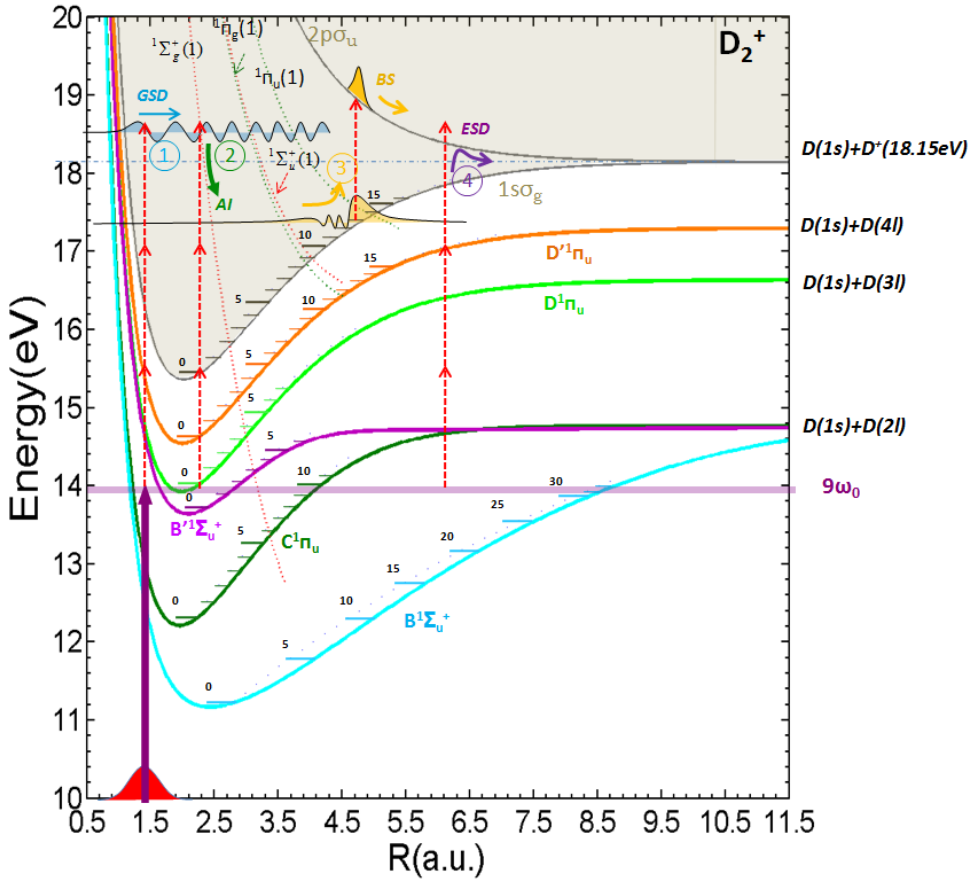

Figure 7.13: The four possible pathways of the dissociative ionization of D_2. (1) Ground state dissociation (GSD). (2) Auto-ionization (AI) from the doubly excited state. (3) Single ionization onto the $1s\sigma_g$ state followed by electronic excitation, i.e. the bond-softening (BS) channel. (4) Direct population of the excited electronic state of D_2^+ at large R from the $B^1\Sigma_u^+$ state, termed as excited state dissociation (ESD). The dotted lines indicate the lowest doubly excited states of D_2 with the corresponding symmetries.

curve producing D^+ and $D(1s)$. This corresponds to the bond softening (BS) process.

(4) The 9th harmonic VUV photon can resonantly populate the $v = 32$ or nearby vibrational states of the $B^1\Sigma_u^+$ electronic state. The wavefunction can extend to large internuclear distance $R = 8.5\ a.u.$ Thus the direct population of the repulsive $2p\sigma_u$ curve is energetically allowed by absorbing 3 IR photons (at $R > 5.5\ a.u$), the following fragmentation of D_2^+ produces D^+. We call this process the excited state dissociation (ESD).

The major action involves three IR photons according to the e^-–D^+ coincidence measurement shown in Fig. 7.12, thus pathways 1, 2, 4 are possible candidates. The minimum number of IR photons required for pathway 3, namely the bond-softening process, can be deduced from the dressed state Floquet picture, where the potential energy curves are shifted up and down by different numbers of photons to represent dissociation dynamics. Figure 7.14 shows the calculated adiabatic dressed state PECs of D_2^+ for the one photon process. The IR peak intensity has an upper limit of 2×10^{12} W/cm^2 in the experiment. The barrier of the avoided crossing is 17.2 eV, which indicates that the lowest dissociative vibrational state is $v = 11$ at this intensity. This results in a kinetic energy no less than 0.3 eV for the D^+ fragments. In order to let the BS channel take place, a minimum of three IR photons is required to populate $v > 10$ of $1s\sigma_g$ followed by absorbing an additional IR photon for electronic excitation to the $2p\sigma_u$ state. Therefore, a total of four IR photons is required to open the BS channel. The contribution of the BS process to the main action in the pump-probe measurement can therefore be excluded.

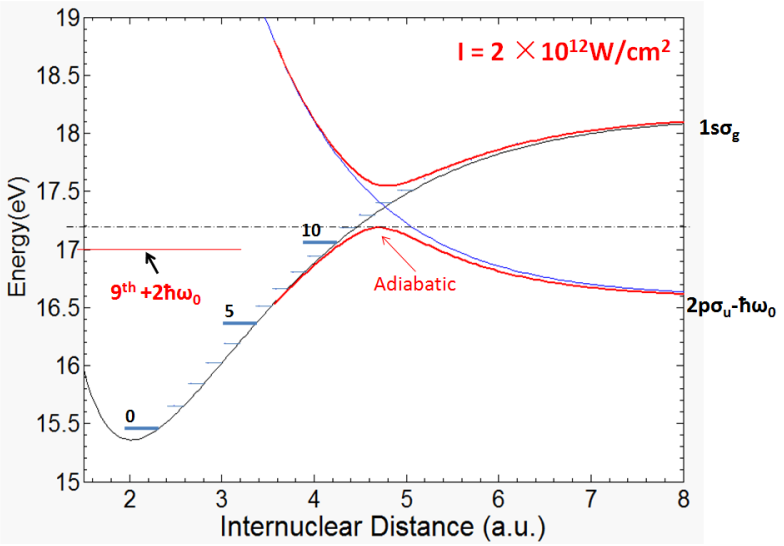

Figure 7.14: The photon-dressed potential energy curves of D_2^+. Both the diabatic and adiabatic PECs are shown for comparison. Laser central wavelength $\lambda_0 = 802$ nm.

The GSD channel involves a direct transition from the ground electronic state of D_2 to

the continuum of the ground electronic state of D_2^+. In this dissociative ionization process the electron takes most of the excess energy leaving the ion carrying almost zero kinetic energy [130, 131]. In our experimental results, we do see D^+ with zero momentum at delays when the D^+ momentum distribution shows dumbbell and butterfly structures. This part seems likely to be associated with the GSD process. Nevertheless, the D^+ energy distribution is peaking at finite kinetic energy (0.1 eV at small delay and 0.2 eV at large delay), thus the main dissociation yield is attributed to other processes.

The autoionization rate of DES is generally monotonically increasing with the internuclear distance up to the crossing point between the DES and the singly charged ionic state [133]. This means that the ion fragments prefer to take most of the kinetic energy in the process of dissociation via the doubly excited state. Thus the DES channel is a reasonable candidate contributing to the non-zero kinetic energy peaks of D^+. The ESD is also possible candidate since the $2p\sigma_u$ state of D_2^+ has a repulsive character.

The delay-dependent angular distribution of D^+ remains a puzzle at the time this thesis is being written. The 9th harmonic can populate a few electronic states (B, B', C) simultaneously within the VUV bandwidth. Then the IR probe feeds three photons into the system to dissociate the molecule. As the energy is approaching the ionization threshold, numerous Rydberg series $np^1\Sigma$, $np^1\Pi$ $(n > 2)$ are mixed together. It is therefore very likely that each IR photon absorption can be resonant leading to either a parallel or perpendicular transition. It is these resonant processes that complicate the elucidation of the experimental data. However, the delay dependent momentum distribution of D^+ indicates that the VUV-IR delay is a promising knob to trigger different dissociation pathways. Further experiments and theoretical calculations are needed to understand the underlying mechanism.

7.4 Summary

We have so far demonstrated two pump-probe experiments on the D_2 molecule using a high-order harmonic based monochromatic VUV source. When the 11th harmonic is serving as the pump, single excitation and single ionization are two competing processes leading to dissociative ionization. The two dissociation channels can be altered by tuning the VUV photon energy, the polarization direction of the IR probe and the delay between the VUV and IR pulses. When the 9th harmonic is serving as the pump, dissociative ionization is mainly triggered by feeding 3 IR photons. The momentum distribution of the final product D^+ shows strong delay-dependent patterns. Possible mechanisms including the autoionization of DES and dissociation along the electronic excited state have been invoked to interpret part of the experimental observations. The reason for the delay-dependent angular distribution of D^+ remains unknown due to the complicated four photon process. These two experiments prove the feasibility of pump-probe studies of molecules with excited neutrals as the intermediate states with the current set-up, thus providing valuable guides and hints for future experiments associated with photochemistry.

Chapter 8

Summary

The pump-probe technique is a powerful tool for revealing transient phenomena in atoms, molecules and even more complex systems. The time resolution of this technique is limited by the temporal duration of both pump and probe pulses. Currently, the pump-probe technique is in a transition from femtosecond time resolution to attosecond time resolution. The IR-pump IR-probe technique has been successfully used to study the dynamic evolution of chemical reactions such as the breakage and formation of chemical bonds [14, 15]. Since the lower limit of the pulse duration of a commercially available ultrafast laser at 800 nm is 2.67 fs, subfemtosecond dynamic information is not accessible with the traditional IR-pump IR-probe approach. The possibility of observing subfemtosecond (attosecond) dynamic evolution has been opened up by the discovery of attosecond extreme ultraviolet (EUV) light sources based on High Harmonic Generation (HHG) [4,5]. However, the very low conversion efficiency of HHG (on the order of 10^{-6} or less with 800 nm driving pulses) [134, 135] precludes its direct application for EUV-pump EUV-probe experiments. Instead, the more intense IR laser pulse is applied to probe (alter) the system's evolution initiated by the EUV attosecond pulses. This EUV-pump IR-probe technique has attracted broad interest nowadays due to its twofold character:

(1) Although strictly speaking it is not direct attosecond pump-probe technique, dynamic

processes with attosecond resolution can still be accessed by locking the EUV attosecond pulse to the carrier of the IR probe. Thus a two-color multi-photon process is triggered, mainly emphasizing the control of this process by altering the relative phase between EUV pulse and IR carrier (attaining subfemtosecond resolution) [2, 34, 37–40].

(2) The EUV photon has the ability to interact with inner shell electrons in a multi-electron system. Thus, an excited state can be populated by absorbing an EUV photon. Then, the unstable excited system may decay via different pathways including autoionization, shake-up process *etc.* [47, 48]. This offers unique way to conduct time-resolved studies of electron correlation.

This dissertation is devoted to the development of table-top EUV (VUV) light sources based on HHG and applying the HHG sources to perform EUV(VUV)-IR pump-probe experiments on atoms and small molecules. The major work of my dissertation is divided into two main themes, which are:

(1) Experimental method with several harmonics as the pump pulse

In this part, high harmonics with photon energies spanning from 20 eV (13th harmonic) to 48 eV (31st harmonic) are generated from a semi-infinite gas cell providing a relatively high photon flux. This type of harmonics forms an attosecond pulse train (APT) if the phase-matching of HHG is properly tuned. A Mach-Zehnder interferometer is used to synchronize this APT with an IR probe pulse, allowing pump-probe studies with femtosecond and attosecond time resolution. A cold target recoil ion momentum spectroscopy (COLTRIMS) apparatus is employed for momentum imaging of the charged reaction products. Specifically, we demonstrate that:

(a) the auto-ionization process triggered by the EUV in carbon-monoxide and oxygen cation molecules can be modified by scanning the EUV-IR delay (see chapter 4).

(b) the phase information of the quantum trajectories in bifurcated HHG can be extracted by performing an EUV-IR cross-correlation experiment with attosecond resolution, thus displaying the macroscopic quantum control in HHG (see chapter 5).

(2) Experimental method with a single harmonic as the pump pulse

In this part, a home-made grating-based monochromator is used to filter a single harmonic in the VUV regime, specifically 10 eV (7th) to 20 eV (13th), which serves as the pump pulse. This type of VUV source preserves relatively short temporal duration (∼100 fs) and narrow bandwidth (<200 meV), thus allowing time-resolved studies of specific quantum state(s) populated by the monochromatic VUV source. Experiments on D_2 molecules have been conducted using the 9th or the 11th harmonic as the pump pulse.

In the case of the 11th harmonic, two competing dissociative ionization mechanisms induced by the combination of one VUV photon and one IR photon are observed. These mechanisms are identified as dissociation via direct ionization and dissociation via super-excited state. By tuning the pump photon energy and changing the VUV-IR delay, it is possible to control these two dissociation processes.

In the case of the 9th harmonic, one VUV photon and three IR photons are identified as the major dissociative ionization mechanism. We demonstrate that the D^+ momentum distribution can be altered by changing the EUV-IR delay, indicating that different dissociation pathways are initiated. Since four photons are involved in the whole process, further experiments and theoretical calculations will be needed to understand the underlying mechanisms in detail.

These two experiments, namely the 11th harmonic as a pump and the 9th harmonic as a pump, suggest the potential ability of the current set-up for time-resolved studies and control of photochemistry processes.

Bibliography

[1] E Goulielmakis, M Schultze, M Hofstetter, VS Yakovlev, J Gagnon, M Uiberacker, AL Aquila, EM Gullikson, DT Attwood, R Kienberger, et al. Single-cycle nonlinear optics. *Science*, 320(5883):1614–1617, 2008.

[2] Adrian L Cavalieri, E Goulielmakis, B Horvath, W Helml, M Schultze, M Fieß, V Pervak, L Veisz, VS Yakovlev, M Uiberacker, et al. Intense 1.5-cycle near infrared laser waveforms and their use for the generation of ultra-broadband soft-x-ray harmonic continua. *New Journal of Physics*, 9(7):242, 2007.

[3] E Goulielmakis, VS Yakovlev, AL Cavalieri, M Uiberacker, V Pervak, A Apolonski, R Kienberger, U Kleineberg, and F Krausz. Attosecond control and measurement: lightwave electronics. *Science*, 317(5839):769–775, 2007.

[4] M Hentschel, R Kienberger, Ch Spielmann, GA Reider, N Milosevic, Thomas Brabec, Paul Corkum, Ulrich Heinzmann, Markus Drescher, and F Krausz. Attosecond metrology. *Nature*, 414(6863):509–513, 2001.

[5] P M Paul, ES Toma, P Breger, Genevive Mullot, F Augé, Ph Balcou, HG Muller, and P Agostini. Observation of a train of attosecond pulses from high harmonic generation. *Science*, 292(5522):1689–1692, 2001.

[6] Ferenc Krausz and Misha Ivanov. Attosecond physics. *Reviews of Modern Physics*, 81(1):163, 2009.

[7] Norman B Colthup, Lawrence H Daly, and Stephen E Wiberley. *Introduction to infrared and Raman spectroscopy*. Elsevier, 1990.

[8] Wolfgang Demtröder. *Laser spectroscopy: basic concepts and instrumentation*. Number 2674. Springer, 2003.

[9] Marcus Frederick Charles Ladd and Rex Alfred Palmer. *Structure determination by X-ray crystallography*. Springer, 1985.

[10] Henry N Chapman. X-ray imaging beyond the limits. *Nature Materials*, 8(4):299–301, 2009.

[11] Ahmed H Zewail. Four-dimensional electron microscopy. *Science*, 328(5975):187–193, 2010.

[12] C Altucci, R Velotta, and JP Marangos. Ultra-fast dynamic imaging: an overview of current techniques, their capabilities and future prospects. *Journal of Modern Optics*, 57(11):916–952, 2010.

[13] Cosmin I Blaga, Junliang Xu, Anthony D DiChiara, Emily Sistrunk, Kaikai Zhang, Pierre Agostini, Terry A Miller, Louis F DiMauro, and CD Lin. Imaging ultrafast molecular dynamics with laser-induced electron diffraction. *Nature*, 483(7388):194–197, 2012.

[14] Ahmed H Zewail. *Femtochemistry: ultrafast dynamics of the chemical bond*, volume 1. World Scientific, 1994.

[15] Ahmed H Zewail. Femtochemistry: Atomic-scale dynamics of the chemical bond. *The Journal of Physical Chemistry A*, 104(24):5660–5694, 2000.

[16] Armin Scrinzi, M Yu Ivanov, Reinhard Kienberger, and David M Villeneuve. Attosecond physics. *Journal of Physics B: Atomic, Molecular and Optical Physics*, 39(1):R1, 2006.

[17] PB Corkum and Ferenc Krausz. Attosecond science. *Nature Physics*, 3(6):381–387, 2007.

[18] XF Li, A L'Huillier, M Ferray, LA Lompré, and G Mainfray. Multiple-harmonic generation in rare gases at high laser intensity. *Physical Review A*, 39(11):5751, 1989.

[19] Anne L'Huillier and Ph Balcou. High-order harmonic generation in rare gases with a 1-ps 1053-nm laser. *Physical review letters*, 70(6):774, 1993.

[20] J J Macklin, JD Kmetec, and CL Gordon III. High-order harmonic generation using intense femtosecond pulses. *Physical review letters*, 70(6):766, 1993.

[21] J Itatani, D Zeidler, J Levesque, Michael Spanner, DM Villeneuve, and PB Corkum. Controlling high harmonic generation with molecular wave packets. *Physical review letters*, 94(12):123902, 2005.

[22] Ivan P Christov, Margaret M Murnane, and Henry C Kapteyn. High-harmonic generation of attosecond pulses in the single-cycle regime. *Physical Review Letters*, 78(7):1251, 1997.

[23] Philippe Antoine, Anne L'huillier, and Maciej Lewenstein. Attosecond pulse trains using high-order harmonics. *Physical Review Letters*, 77(7):1234–1237, 1996.

[24] T Baumert, M Grosser, R Thalweiser, and G Gerber. Femtosecond time-resolved molecular multiphoton ionization: The Na_2 system. *Physical review letters*, 67(27):3753, 1991.

[25] M Dantus, MHM Janssen, and AH Zewail. Femtosecond probing of molecular dynamics by mass-spectrometry in a molecular beam. *Chemical physics letters*, 181(4):281–287, 1991.

[26] R de Vivie-Riedle, B Reischl, S Rutz, and E Schreiber. Femtosecond study of multiphoton ionization processes in K_2 at moderate laser intensities. *The Journal of Physical Chemistry*, 99(46):16829–16834, 1995.

[27] Th Ergler, A Rudenko, B Feuerstein, K Zrost, CD Schröter, R Moshammer, and J Ullrich. Spatiotemporal imaging of ultrafast molecular motion: collapse and revival of the D_2^+ nuclear wave packet. *Physical review letters*, 97(19):193001, 2006.

[28] S De, Maia Magrakvelidze, IA Bocharova, D Ray, W Cao, I Znakovskaya, H Li, Z Wang, G Laurent, U Thumm, et al. Following dynamic nuclear wave packets in N_2, O_2, and CO with few-cycle infrared pulses. *Physical Review A*, 84(4):043410, 2011.

[29] S De, IA Bocharova, Maia Magrakvelidze, D Ray, W Cao, B Bergues, U Thumm, Matthias F Kling, IV Litvinyuk, and Charles L Cocke. Tracking nuclear wave-packet dynamics in molecular oxygen ions with few-cycle infrared laser pulses. *Physical Review A*, 82(1):013408, 2010.

[30] NN Choi, TF Jiang, T Morishita, M-H Lee, and CD Lin. Theory of probing attosecond electron wave packets via two-path interference of angle-resolved photoelectrons. *Physical Review A*, 82(1):013409, 2010.

[31] Johan Mauritsson, Thomas Remetter, Marko Swoboda, Kathrin Klünder, Anne L'Huillier, KJ Schafer, Omair Ghafur, F Kelkensberg, W Siu, Per Johnsson, et al. Attosecond electron spectroscopy using a novel interferometric pump-probe technique. *Physical review letters*, 105(5):053001, 2010.

[32] J Itatani, F Quéré, Gennady L Yudin, Misha Yu Ivanov, Ferenc Krausz, and Paul B Corkum. Attosecond streak camera. *Physical review letters*, 88(17):173903–173903, 2002.

[33] E Goulielmakis, VS Yakovlev, AL Cavalieri, M Uiberacker, V Pervak, A Apolonski, R Kienberger, U Kleineberg, and F Krausz. Attosecond control and measurement: lightwave electronics. *Science*, 317(5839):769–775, 2007.

[34] Martin Schultze, M Fieß, N Karpowicz, J Gagnon, M Korbman, M Hofstetter, S Neppl, AL Cavalieri, Y Komninos, Th Mercouris, et al. Delay in photoemission. *Science*, 328(5986):1658–1662, 2010.

[35] Y Mairesse, A De Bohan, LJ Frasinski, H Merdji, LC Dinu, P Monchicourt, P Breger, M Kovačev, R Taïeb, B Carré, et al. Attosecond synchronization of high-harmonic soft x-rays. *Science*, 302(5650):1540–1543, 2003.

[36] Valérie Véniard, Richard Taïeb, and Alfred Maquet. Phase dependence of (N+1)-color (N>1) IR-UV photoionization of atoms with higher harmonics. *Physical Review A*, 54(1):721, 1996.

[37] Markus Drescher, Michael Hentschel, R Kienberger, Matthias Uiberacker, Vladislav Yakovlev, Armin Scrinzi, Th Westerwalbesloh, U Kleineberg, Ulrich Heinzmann, and Ferenc Krausz. Time-resolved atomic inner-shell spectroscopy. *Nature*, 419(6909):803–807, 2002.

[38] Reinhard Kienberger, Eleftherios Goulielmakis, Matthias Uiberacker, Andrius Baltuska, Vladislav Yakovlev, Ferdinand Bammer, Armin Scrinzi, Th Westerwalbesloh, Ulf Kleineberg, Ulrich Heinzmann, et al. Atomic transient recorder. *Nature*, 427(6977):817–821, 2004.

[39] Matthias Uiberacker, Th Uphues, Martin Schultze, Aart J Verhoef, Vladislav Yakovlev, Matthias F Kling, Jens Rauschenberger, Nicolai M Kabachnik, Hartmut Schröder, Matthias Lezius, et al. Attosecond real-time observation of electron tunnelling in atoms. *Nature*, 446(7136):627–632, 2007.

[40] Eleftherios Goulielmakis, Zhi-Heng Loh, Adrian Wirth, Robin Santra, Nina Rohringer, Vladislav S Yakovlev, Sergey Zherebtsov, Thomas Pfeifer, Abdallah M Azzeer, Matthias F Kling, et al. Real-time observation of valence electron motion. *Nature*, 466(7307):739–743, 2010.

[41] Raimund Feifel, JHD Eland, and David Edvardsson. Valence double ionization of O_2 at photon energies below and above the molecular double ionization threshold. *The Journal of chemical physics*, 122(14):144308, 2005.

[42] SD Price and JHD Eland. Single photon double ionization of the oxygen molecule. *Journal of Physics B: Atomic, Molecular and Optical Physics*, 24(20):4379, 1991.

[43] S Hsieh and JHD Eland. Direct and indirect dissociative double photoionization of diatomic molecules. *Journal of Physics B: Atomic, Molecular and Optical Physics*, 29(23):5795, 1996.

[44] Timur Osipov, Th Weber, Thomas N Rescigno, SY Lee, AE Orel, M Schöffler, FP Sturm, S Schössler, U Lenz, T Havermeier, et al. Formation of inner-shell autoionizing CO^+ states below the CO^{2+} threshold. *Physical Review A*, 81(1):011402, 2010.

[45] G Sansone, F Kelkensberg, JF Pérez-Torres, F Morales, MF Kling, W Siu, Omair Ghafur, Per Johnsson, Marko Swoboda, E Benedetti, et al. Electron localization following attosecond molecular photoionization. *Nature*, 465(7299):763–766, 2010.

[46] Markus Drescher, Michael Hentschel, R Kienberger, Matthias Uiberacker, Vladislav Yakovlev, Armin Scrinzi, Th Westerwalbesloh, U Kleineberg, Ulrich Heinzmann, and Ferenc Krausz. Time-resolved atomic inner-shell spectroscopy. *Nature*, 419(6909):803–807, 2002.

[47] Etienne Gagnon, Predrag Ranitovic, Xiao-Min Tong, C Lewis Cocke, Margaret M Murnane, Henry C Kapteyn, and Arvinder S Sandhu. Soft x-ray-driven femtosecond molecular dynamics. *Science*, 317(5843):1374–1378, 2007.

[48] Arvinder S Sandhu, Etienne Gagnon, Robin Santra, Vandana Sharma, Wen Li, Phay Ho, Predrag Ranitovic, C Lewis Cocke, Margaret M Murnane, and Henry C Kapteyn.

Observing the creation of electronic feshbach resonances in soft x-ray–induced O_2 dissociation. *Science*, 322(5904):1081–1085, 2008.

[49] X Zhou, P Ranitovic, CW Hogle, JHD Eland, HC Kapteyn, and MM Murnane. Probing and controlling non-born-oppenheimer dynamics in highly excited molecular ions. *Nature Physics*, 8(3):232–237, 2012.

[50] Lora Nugent-Glandorf, Michael Scheer, David A Samuels, Anneliese M Mulhisen, Edward R Grant, Xueming Yang, Veronica M Bierbaum, and Stephen R Leone. Ultrafast time-resolved soft x-ray photoelectron spectroscopy of dissociating Br_2. *Physical review letters*, 87(19):193002, 2001.

[51] Philippe Wernet, Jérôme Gaudin, Kai Godehusen, Olaf Schwarzkopf, and Wolfgang Eberhardt. Femtosecond time-resolved photoelectron spectroscopy with a vacuum-ultraviolet photon source based on laser high-order harmonic generation. *Review of Scientific Instruments*, 82(6):063114, 2011.

[52] Mizuho Fushitani, Akitaka Matsuda, and Akiyoshi Hishikawa. Euv and soft x-ray photoelectron spectroscopy of isolated atoms and molecules using single-order laser high-harmonics at 42ev and 91ev. *Journal of Electron Spectroscopy and Related Phenomena*, 184(11):561–568, 2012.

[53] TK Allison, TW Wright, AM Stooke, Champak Khurmi, Jeroen van Tilborg, Yanwei Liu, RW Falcone, and Ali Belkacem. Femtosecond spectroscopy with vacuum ultraviolet pulse pairs. *Optics letters*, 35(21):3664–3666, 2010.

[54] SL Sorensen, O Björneholm, I Hjelte, T Kihlgren, G Öhrwall, S Sundin, S Svensson, S Buil, D Descamps, A L?Huillier, et al. Femtosecond pump–probe photoelectron spectroscopy of predissociative rydberg states in acetylene. *The Journal of Chemical Physics*, 112(18):8038–8042, 2000.

[55] Ph Wernet, M Odelius, K Godehusen, J Gaudin, O Schwarzkopf, and W Eberhardt. Real-time evolution of the valence electronic structure in a dissociating molecule. *Physical review letters*, 103(1):013001, 2009.

[56] T Ditmire, ET Gumbrell, RA Smith, JWG Tisch, DD Meyerhofer, and MHR Hutchinson. Spatial coherence measurement of soft x-ray radiation produced by high order harmonic generation. *Physical review letters*, 77(23):4756, 1996.

[57] M Bellini, C Lyngå, A Tozzi, MB Gaarde, TW Hänsch, Anne L'Huillier, and C-G Wahlström. Temporal coherence of ultrashort high-order harmonic pulses. *Physical review letters*, 81(2):297, 1998.

[58] C Lyngå, MB Gaarde, C Delfin, M Bellini, TW Hänsch, Anne L?Huillier, and C-G Wahlström. Temporal coherence of high-order harmonics. *Physical Review A*, 60(6):4823, 1999.

[59] Randy A Bartels, Ariel Paul, Hans Green, Henry C Kapteyn, Margaret M Murnane, Sterling Backus, Ivan P Christov, Yanwei Liu, David Attwood, and Chris Jacobsen. Generation of spatially coherent light at extreme ultraviolet wavelengths. *Science*, 297(5580):376–378, 2002.

[60] DG Lee, JJ Park, JH Sung, and CH Nam. Wave-front phase measurements of high-order harmonic beams by use of point-diffraction interferometry. *Optics letters*, 28(6):480–482, 2003.

[61] Paul B Corkum. Plasma perspective on strong field multiphoton ionization. *Physical Review Letters*, 71(13):1994, 1993.

[62] KC Kulander, KJ Schafer, and JL Krause. Proceedings of the workshop, super intense laser atom physics (silap) iii, 1993.

[63] M Lewenstein, Ph Balcou, M Yu Ivanov, Anne L?huillier, and Paul B Corkum. Theory of high-harmonic generation by low-frequency laser fields. *Physical Review A*, 49(3):2117, 1994.

[64] Pascal Salières, B Carré, L Le Déroff, F Grasbon, GG Paulus, H Walther, R Kopold, W Becker, DB Milošević, A Sanpera, et al. Feynman's path-integral approach for intense-laser-atom interactions. *Science*, 292(5518):902–905, 2001.

[65] Maxim V Ammosov, Nikolai B Delone, and Vladimir P Krainov. Tunnel ionization of complex atoms and atomic ions in electromagnetic field. In *1986 Quebec Symposium*, pages 138–141. International Society for Optics and Photonics, 1986.

[66] XM Tong and CD Lin. Empirical formula for static field ionization rates of atoms and molecules by lasers in the barrier-suppression regime. *Journal of Physics B: Atomic, Molecular and Optical Physics*, 38(15):2593, 2005.

[67] Toru Morishita, Anh-Thu Le, Zhangjin Chen, and CD Lin. Accurate retrieval of structural information from laser-induced photoelectron and high-order harmonic spectra by few-cycle laser pulses. *Physical review letters*, 100(1):013903, 2008.

[68] CD Lin, Anh-Thu Le, Zhangjin Chen, Toru Morishita, and Robert Lucchese. Strong-field rescattering physics: self-imaging of a molecule by its own electrons. *Journal of Physics B: Atomic, Molecular and Optical Physics*, 43(12):122001, 2010.

[69] Anh-Thu Le, RR Lucchese, S Tonzani, T Morishita, and CD Lin. Quantitative rescattering theory for high-order harmonic generation from molecules. *Physical Review A*, 80(1):013401, 2009.

[70] Cheng Jin, Anh-Thu Le, and CD Lin. Retrieval of target photorecombination cross sections from high-order harmonics generated in a macroscopic medium. *Physical Review A*, 79(5):053413, 2009.

[71] Cheng Jin, Hans Jakob Wörner, V Tosa, Anh-Thu Le, Julien B Bertrand, RR Lucchese, PB Corkum, DM Villeneuve, and CD Lin. Separation of target structure and medium propagation effects in high-harmonic generation. *Journal of Physics B: Atomic, Molecular and Optical Physics*, 44(9):095601, 2011.

[72] Pascal Salieres, Anne L'Huillier, and Maciej Lewenstein. Coherence control of high-order harmonics. *Physical Review Letters-Moving Physics Forward*, 74(19):3776–3779, 1995.

[73] Sophie Kazamias, D Douillet, Frederick Weihe, C Valentin, Antoine Rousse, Stéphane Sebban, G Grillon, F Augé, D Hulin, and Ph Balcou. Global optimization of high harmonic generation. *Physical review letters*, 90(19):193901, 2003.

[74] E Constant, D Garzella, P Breger, E Mével, Ch Dorrer, C Le Blanc, F Salin, and P Agostini. Optimizing high harmonic generation in absorbing gases: Model and experiment. *Physical Review Letters*, 82(8):1668, 1999.

[75] E Priori, G Cerullo, M Nisoli, S Stagira, S De Silvestri, P Villoresi, L Poletto, P Ceccherini, C Altucci, R Bruzzese, et al. Nonadiabatic three-dimensional model of high-order harmonic generation in the few-optical-cycle regime. *Physical Review A*, 61(6):063801, 2000.

[76] Mette B Gaarde, Jennifer L Tate, and Kenneth J Schafer. Macroscopic aspects of attosecond pulse generation. *Journal of Physics B: Atomic, Molecular and Optical Physics*, 41(13):132001, 2008.

[77] Johan Mauritsson, Per Johnsson, E Gustafsson, Anne L'Huillier, KJ Schafer, and MB Gaarde. Attosecond pulse trains generated using two color laser fields. *Physical review letters*, 97(1):013001, 2006.

[78] Guillaume Laurent, Wei Cao, H Li, Zhenhua Wang, Itzhak Ben-Itzhak, and Charles L Cocke. Attosecond control of orbital parity mix interferences and the relative phase

of even and odd harmonics in an attosecond pulse train. *Physical review letters*, 109(8):083001, 2012.

[79] G Sansone, E Benedetti, F Calegari, C Vozzi, L Avaldi, R Flammini, L Poletto, P Villoresi, C Altucci, R Velotta, et al. Isolated single-cycle attosecond pulses. *Science*, 314(5798):443–446, 2006.

[80] VT Platonenko and VV Strelkov. Single attosecond soft-x-ray pulse generated with a limited laser beam. *JOSA B*, 16(3):435–440, 1999.

[81] Zenghu Chang. Chirp of the single attosecond pulse generated by a polarization gating. *Physical Review A*, 71(2):023813, 2005.

[82] Wei Cao, Peixiang Lu, Pengfei Lan, Xinlin Wang, and Guang Yang. Single-attosecond pulse generation with an intense multicycle driving pulse. *Physical Review A*, 74(6):063821, 2006.

[83] F Ferrari, F Calegari, M Lucchini, C Vozzi, S Stagira, G Sansone, and M Nisoli. High-energy isolated attosecond pulses generated by above-saturation few-cycle fields. *Nature Photonics*, 4(12):875–879, 2010.

[84] Thomas Pfeifer, AurÚlie Jullien, Mark J Abel, Phillip M Nagel, Lukas Gallmann, Daniel M Neumark, and Stephen R Leone. Generating coherent broadband continuum soft-x-ray radiation by attosecond ionization gating. *Optics express*, 15(25):17120–17128, 2007.

[85] Mette Borg Gaarde, F Salin, E Constant, Ph Balcou, KJ Schafer, KC Kulander, and L'Huillier Anne. Spatiotemporal separation of high harmonic radiation into two quantum path components. *Physical Review A*, 59(2):1367, 1999.

[86] Donna Strickland and Gerard Mourou. Compression of amplified chirped optical pulses. *Optics Communications*, 55(6):447–449, 1985.

[87] Rick Trebino, Kenneth W DeLong, David N Fittinghoff, John N Sweetser, Marco A Krumbügel, Bruce A Richman, and Daniel J Kane. Measuring ultrashort laser pulses in the time-frequency domain using frequency-resolved optical gating. *Review of Scientific Instruments*, 68(9):3277–3295, 1997.

[88] Rick Trebino. *Frequency-resolved optical gating: the measurement of ultrashort laser pulses*, volume 1. Springer, 2000.

[89] DB Milošević, GG Paulus, D Bauer, and W Becker. Above-threshold ionization by few-cycle pulses. *Journal of Physics B: Atomic, Molecular and Optical Physics*, 39(14):R203, 2006.

[90] AS Alnaser, XM Tong, T Osipov, S Voss, CM Maharjan, B Shan, Z Chang, and CL Cocke. Laser-peak-intensity calibration using recoil-ion momentum imaging. *Physical Review A*, 70(2):023413, 2004.

[91] E Goulielmakis, M Uiberacker, R Kienberger, A Baltuska, V Yakovlev, A Scrinzi, Th Westerwalbesloh, U Kleineberg, Ulrich Heinzmann, Markus Drescher, et al. Direct measurement of light waves. *Science*, 305(5688):1267–1269, 2004.

[92] J Itatani, F Quéré, Gennady L Yudin, Misha Yu Ivanov, Ferenc Krausz, and Paul B Corkum. Attosecond streak camera. *Physical review letters*, 88(17):173903–173903, 2002.

[93] Markus Kitzler, Nenad Milosevic, Armin Scrinzi, Ferenc Krausz, and Thomas Brabec. Quantum theory of attosecond xuv pulse measurement by laser dressed photoionization. *Physical review letters*, 88(17):173904, 2002.

[94] Ximao Feng, Steve Gilbertson, Hiroki Mashiko, He Wang, Sabih D Khan, Michael Chini, Yi Wu, Kun Zhao, and Zenghu Chang. Generation of isolated attosecond pulses with 20 to 28 femtosecond lasers. *Physical review letters*, 103(18):183901, 2009.

[95] Etienne Gagnon, Arvinder S Sandhu, Ariel Paul, Kim Hagen, Achim Czasch, Till Jahnke, Predrag Ranitovic, C Lewis Cocke, Barry Walker, Margaret M Murnane, et al. Time-resolved momentum imaging system for molecular dynamics studies using a tabletop ultrafast extreme-ultraviolet light source. *Review of Scientific Instruments*, 79(6):063102, 2008.

[96] Daniel S Steingrube, Tobias Vockerodt, Emilia Schulz, Uwe Morgner, and Milutin Kovačev. Phase matching of high-order harmonics in a semi-infinite gas cell. *Physical Review A*, 80(4):043819, 2009.

[97] Julia Sutherland, E Christensen, N Powers, S Rhynard, J Painter, and J Peatross. High harmonic generation in a semi-infinite gas cell. *Optics express*, 12(19):4430–4436, 2004.

[98] John C Painter, Mark Adams, Nicole Brimhall, Eric Christensen, Gavin Giraud, Nathan Powers, Matthew Turner, Michael Ware, and Justin Peatross. Direct observation of laser filamentation in high-order harmonic generation. *Optics letters*, 31(23):3471–3473, 2006.

[99] J Ullrich, R Moshammer, A Dorn, R Dörner, L Ph H Schmidt, and H Schmidt-Böcking. Recoil-ion and electron momentum spectroscopy: reaction-microscopes. *Reports on Progress in Physics*, 66(9):1463, 2003.

[100] Reinhard Dörner, Volker Mergel, Ottmar Jagutzki, Lutz Spielberger, Joachim Ullrich, Robert Moshammer, and Horst Schmidt-Böcking. Cold target recoil ion momentum spectroscopy: a *momentummicroscope* to view atomic collision dynamics. *Physics Reports*, 330(2):95–192, 2000.

[101] P Jardin, A Cassimi, JP Grandin, D Hennecart, and JP Lemoigne. Dynamics of Xe^{44+}(6.7 MeV/A)+ Ar and He collisions. *Nuclear Instruments and Methods in*

Physics Research Section B: Beam Interactions with Materials and Atoms, 107(1):41–46, 1996.

[102] CL Cocke and Ronald E Olson. Recoil ions. *Physics reports*, 205(4):153–219, 1991.

[103] http://www.hamamatsu.com/resources/pdf/etd/MCPassy_TMCP0001E10.pdf.

[104] Matthias Uiberacker, Th Uphues, Martin Schultze, Aart J Verhoef, Vladislav Yakovlev, Matthias F Kling, Jens Rauschenberger, Nicolai M Kabachnik, Hartmut Schröder, Matthias Lezius, et al. Attosecond real-time observation of electron tunnelling in atoms. *Nature*, 446(7136):627–632, 2007.

[105] Eiji J Takahashi, Yasuo Nabekawa, and Katsumi Midorikawa. Low-divergence coherent soft x-ray source at 13 nm by high-order harmonics. *Applied physics letters*, 84(1):4–6, 2003.

[106] P Siffalovic, Markus Drescher, M Spieweck, T Wiesenthal, YC Lim, R Weidner, A Elizarov, and Ulrich Heinzmann. Laser-based apparatus for extended ultraviolet femtosecond time-resolved photoemission spectroscopy. *Review of Scientific Instruments*, 72(1):30–35, 2001.

[107] Mizuho Fushitani, Akitaka Matsuda, and Akiyoshi Hishikawa. Time-resolved euv photoelectron spectroscopy of dissociating I_2 by laser harmonics at 80 nm. *Optics express*, 19(10):9600–9606, 2011.

[108] Luca Poletto, Paolo Villoresi, Enrico Benedetti, Federico Ferrari, Salvatore Stagira, Giuseppe Sansone, and Mauro Nisoli. Intense femtosecond extreme ultraviolet pulses by using a time-delay-compensated monochromator. *Optics letters*, 32(19):2897–2899, 2007.

[109] Forrest R Gilmore. Potential energy curves for N_2, NO, O_2 and corresponding ions. *Journal of Quantitative Spectroscopy and Radiative Transfer*, 5(2):369–IN3, 1965.

[110] Robert L Platzman. Superexcited states of molecules. *Radiation Research*, 17(3):419–425, 1962.

[111] U Fantz and D Wünderlich. Franck–condon factors, transition probabilities, and radiative lifetimes for hydrogen molecules and their isotopomeres. *Atomic Data and Nuclear Data Tables*, 92(6):853–973, 2006.

[112] Steven L Guberman. The doubly excited autoionizing states of H_2. *The Journal of Chemical Physics*, 78(3):1404–1413, 1983.

[113] Phil H Bucksbaum, Anton Zavriyev, Harm G Muller, and Douglass W Schumacher. Softening of the H_2^+ molecular bond in intense laser fields. *Physical review letters*, 64(16):1883, 1990.

[114] Annick Giusti-Suzor, Xin He, Osman Atabek, and Frederic H Mies. Above-threshold dissociation of H_2^+ in intense laser fields. *Physical review letters*, 64(5):515, 1990.

[115] Annick Giusti-Suzor, Frederic H Mies, Louis F DiMauro, Eric Charron, and Baorui Yang. Dynamics of H_2^+ in intense laser fields. *Journal of Physics B: Atomic, Molecular and Optical Physics*, 28(3):309, 1995.

[116] M Glass-Maujean, J Breton, and PM Guyon. Accidental predissociation of the $4p\ \pi\ ^1\Pi_u^+$ State of H_2. *Physical Review Letters*, 40(3):181, 1978.

[117] Yoshihiko Hatano. Interaction of vacuum ultraviolet photons with molecules. formation and dissociation dynamics of molecular superexcited states. *Physics reports*, 313(3):109–169, 1999.

[118] Noriyuki Kouchi, Masatoshi Ukai, and Yoshihiko Hatano. Dissociation dynamics of superexcited molecular hydrogen. *Journal of Physics B: Atomic, Molecular and Optical Physics*, 30(10):2319, 1997.

[119] M Glass-Maujean, S Klumpp, L Werner, A Ehresmann, and H Schmoranzer. The study of the D'$^1\Pi_u$ state of H_2: Transition probabilities from the ground state, predissociation yields, and natural linewidths. *The Journal of chemical physics*, 128(9):094312, 2008.

[120] M Glass-Maujean, Ch Jungen, H Schmoranzer, A Knie, I Haar, R Hentges, W Kielich, K Jänkälä, and A Ehresmann. H_2 superexcited states: Experimental and Theoretical Characterization of their Competing Decay-Channel Fluorescence, Dissociation, and Ionization. *Physical review letters*, 104(18):183002, 2010.

[121] M Glass-Maujean, Ch Jungen, G Reichardt, A Balzer, H Schmoranzer, A Ehresmann, I Haar, and P Reiss. Competing decay-channel fluorescence, dissociation, and ionization in superexcited levels of H_2. *Physical Review A*, 82(6):062511, 2010.

[122] A Azarm, D Song, K Liu, S Hosseini, Y Teranishi, SH Lin, A Xia, F Kong, and SL Chin. Neutral dissociation of hydrogen molecules in a strong laser field through superexcited states. *Journal of Physics B: Atomic, Molecular and Optical Physics*, 44(8):085601, 2011.

[123] Molly A Taylor, Jordan M Pio, Wytze E van der Veer, and Kenneth C Janda. Competition between electronic and vibrational predissociation dynamics of the $HeBr_2$ and $NeBr_2$ van der waals molecules. *The Journal of chemical physics*, 132(10):104309, 2010.

[124] S Strathdee and R Browning. Dissociative photoionization of H_2 at 26.9 ev. *Journal of Physics B: Atomic and Molecular Physics*, 9(16):L505, 1976.

[125] M Glass-Maujean. Photodissociation of doubly excited states of H_2: Emission of Balmer lines. *The Journal of chemical physics*, 89(5):2839–2843, 1988.

[126] F Martín, J Fernández, T Havermeier, L Foucar, Th Weber, K Kreidi, M Schöffler, L Schmidt, T Jahnke, O Jagutzki, et al. Single photon-induced symmetry breaking of H_2 dissociation. *Science*, 315(5812):629–633, 2007.

[127] William A Chupka. Photoionization of molecular Rydberg states: H_2, $C^1\Pi_u$ and its doubly excited states. *The Journal of chemical physics*, 87(3):1488–1498, 1987.

[128] M Glass-Maujean, S Klumpp, L Werner, A Ehresmann, and H Schmoranzer. The study of the fifth state ($5p\sigma$) of H_2: transition probabilities from the ground state, natural line widths and predissociation yields. *Journal of Molecular Spectroscopy*, 249(1):51–59, 2008.

[129] R Browning and J Fryar. Dissociative photoionization of H_2 and D_2 through the $1s\sigma g$ ionic state. *Journal of Physics B: Atomic and Molecular Physics*, 6(2):364, 1973.

[130] S Strathdee and R Browning. Dissociative photoionisation of H_2: proton kinetic energy spectra. *Journal of Physics B: Atomic and Molecular Physics*, 12(11):1789, 1979.

[131] Kenji Ito, Richard I Hall, and Masatoshi Ukai. Dissociative photoionization of H_2 and D_2 in the energy region of 25–45 ev. *The Journal of chemical physics*, 104(21):8449–8457, 1996.

[132] S Strathdee and R Browning. Dissociative photoionisation of H_2: proton kinetic energy spectra. *Journal of Physics B: Atomic and Molecular Physics*, 12(11):1789, 1979.

[133] I Sánchez and F Martín. The doubly excited states of the H_2 molecule. *The Journal of chemical physics*, 106(18):7720–7730, 1997.

[134] J Tate, T Auguste, HG Muller, P Salieres, P Agostini, and LF DiMauro. Scaling of wave-packet dynamics in an intense midinfrared field. *Physical review letters*, 98(1):013901, 2007.

[135] Andy Rundquist, Charles G Durfee, Zenghu Chang, Catherine Herne, Sterling Backus, Margaret M Murnane, and Henry C Kapteyn. Phase-matched generation of coherent soft x-rays. *Science*, 280(5368):1412–1415, 1998.

[136] B Brehm, J Grosser, T Ruscheinski, and M Zimmer. Absolute detection efficiencies of a microchannel plate detector for ions. *Measurement science and Technology*, 6(7):953, 1995.

Appendix A

Calibrations in COLTRIMS measurements

In a COLTRIMS experiment, precise reconstruction of the momentum vectors of charged particles requires the predetermination of a few experimental constants. Since both the electric field (E) and the magnetic field (B) are along the spectrometer axis of symmetry (z) (see Fig. 3.8 in chapter 3 for axes convention), the charged particle experiences a linear acceleration along z induced by the E field and a circular motion (counter clockwise in our case) in the plane perpendicular to z induced by the B field. Figure A.1 shows the trajectory of the particle with initial velocity v_0 in the plane perpendicular to the z axis.

Once the distance of the detector from the interaction region (L), the initial time (t_0) and the initial position (x_0, y_0) are known precisely, then the three components of momentum of a charged particle can be calculated:

$$P_z = \frac{mL}{t - t_0} - \frac{Eq(t - t_0)}{2}, \tag{A.1}$$

$$P_x = \frac{m\omega}{2}[(x - x_0)\cot(\frac{m\omega}{2}) + (y - y_0)], \tag{A.2}$$

$$P_y = \frac{m\omega}{2}[(y - y_0)\cot(\frac{m\omega}{2}) - (x - x_0)], \tag{A.3}$$

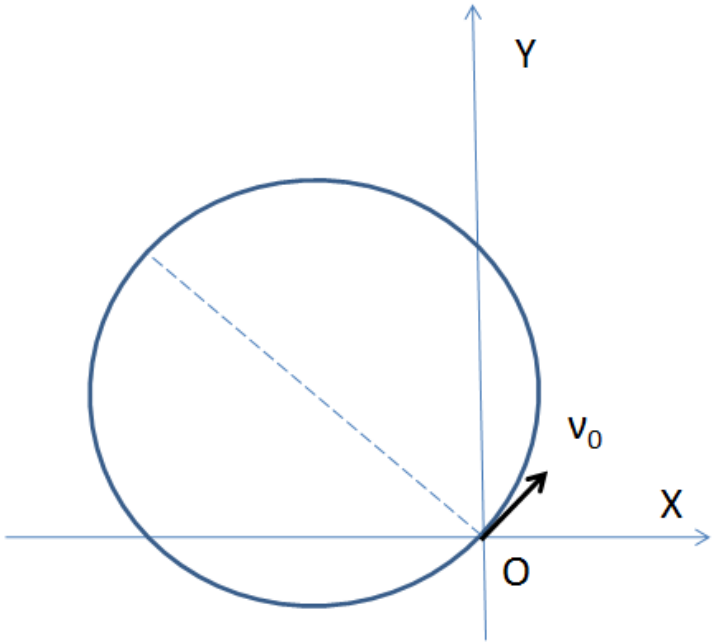

Figure A.1: The trajectory of the charged particle driven by the magnetic field B is a circle tangent to its initial velocity v_0.

where m, q are the mass and charge of the particle, respectively, t is the measured TOF, and $\omega = \frac{Bq}{m}$ stands for the cyclotron frequency.

In principle, all parameters in the above equations (i.e. L, t_0, x_0, y_0, E and B) could be predetermined if the whole system was designed and measured very carefully. However, any change of the set-up, e.g. the optical alignment, the electronics, the location of the gas jet, could change the values of these constants, which can increase the system error of the measurement. This problem is solvable thanks to the fact that the COLTRIMS is a self-calibrated system. Most of the parameters can be calibrated from the raw data itself, and thus accurate data analysis will be guaranteed.

Calibration for ions: The initial time (t_0), which is the difference between the time when the interaction occurs and the time registered by the TDC, is on the order of a few nanoseconds (ns). For ions, each peak in the TOF spectrum corresponds to a mass/charge ratio, $\frac{m}{q}$, and the peak location means $P_z = 0$. Based on equation A.1, $\frac{m}{q}$ will be a parabolic

function of time $t - t_0$ if $P_z = 0$. Thus t_0 can be calibrated by fitting the $\sqrt{\frac{m}{q}}$ versus $(t - t_0)$ curve with a linear function. The TOF of ions is typically on the order of a few thousand ns, therefore the effect of t_0 on the momentum construction of ions is negligible and the calibration of t_0 for ions is usually not necessary.

The calibration of the initial position in the XY plane, x_0 and y_0, is trivial. The position image on the detector (i.e. the coordinates of ions in the XY plane) is localized around the jet position due to the fact that the ions are heavy particles. The most intense spot on the ion detector image generally corresponds to atomic ions or non-dissociative molecular ions with zero transverse momentum. Thus the x_0, y_0 can be directly obtained from the position of this intense spot on the detector.

Calibration for electrons: An electron has a mass that is more than three orders of magnitude less than the ion mass. Thus electrons have very short TOF (on the order of a few tens to a few hundreds of ns). t_0 calibration is rather essential for electron momentum construction. The calibration of t_0, x_0, y_0 and magnetic field strength B can all be executed together from the position versus TOF 2-D images of electrons. Figure A.2 shows the position of the electron as a function of the measured TOF. The electron revisits the origin at a frequency of $f = \frac{\omega}{2\pi}$ according to Fig. A.1. This gives rise to multiple nodes in position—time-of-flight plots shown in Fig. A.2. Thus the initial position (x_0 and y_0) of the interaction is the node coordinate in the XY plane, which can be directly obtained from Fig. A.2(b) and Fig. A.2(c). The TOF difference between consecutive nodes is equal to the cyclotron period of an electron in the magnetic field, $T = \frac{2\pi}{\omega}$. Thus the TOF of the Nth node can be expressed as: $t_N = NT + t_0$. Then t_0 can be retrieved by fitting t_N versus N curve with a straight line as shown in Fig. A.3. The magnetic field strength can be deduced from the cyclotron period T, $B = \frac{2\pi m}{Tq}$. From the data shown in Fig. A.3, the calibrated parameters are: $t_0 = 4.5$ ns, $B = 1.7$ Gauss, $x_0 = 0$, $y_0 = 2.5$ mm.

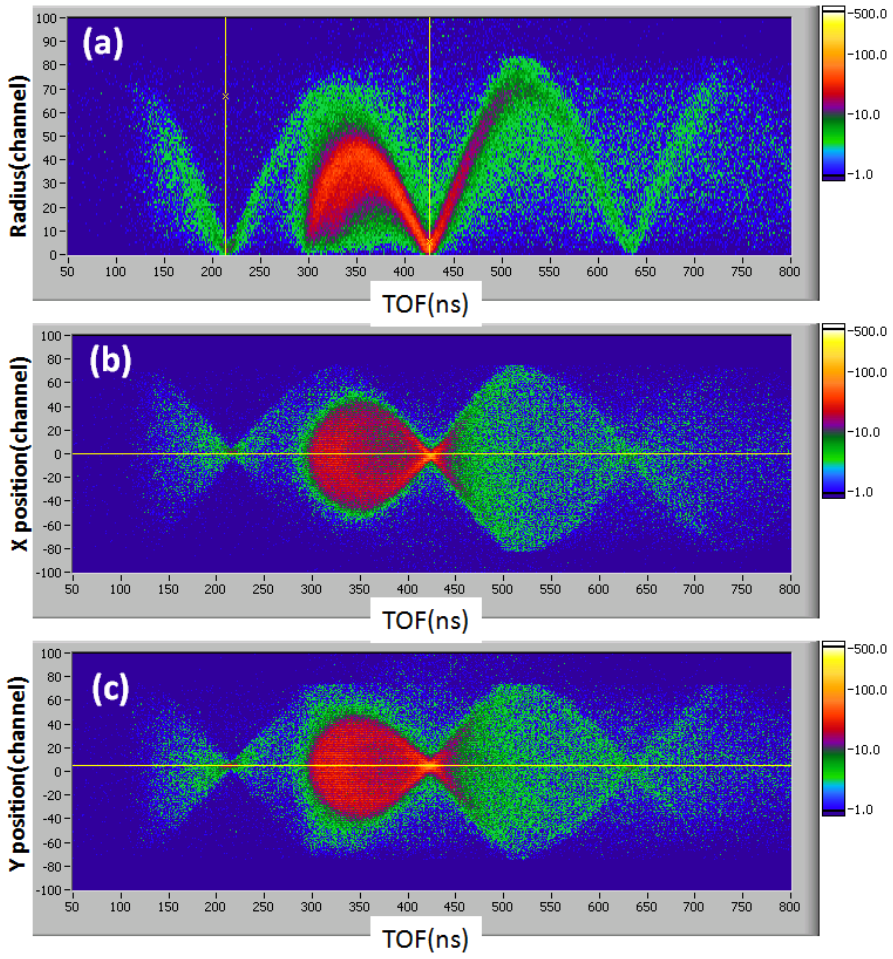

Figure A.2: (a) The hit distance from the center of the detector (radius) as a function of TOF of electrons. (b) X position as a function of TOF. (c) Y position as a function of TOF. The electrons are generated by irradiating the argon gas with the 11th harmonic (17 eV). The extraction electric field across the spectrometer is $E = 0$. The three node positions are $t_1 = 214.5$ ns, $t_2 = 425$ ns and $t_3 = 634.5$ ns, respectively. The coordinates of the nodes are $x_0 = 0$ (from panel b) and $y_0 = 5$ channel (from panel c). The channel—distance conversion is 0.5 mm/channel.

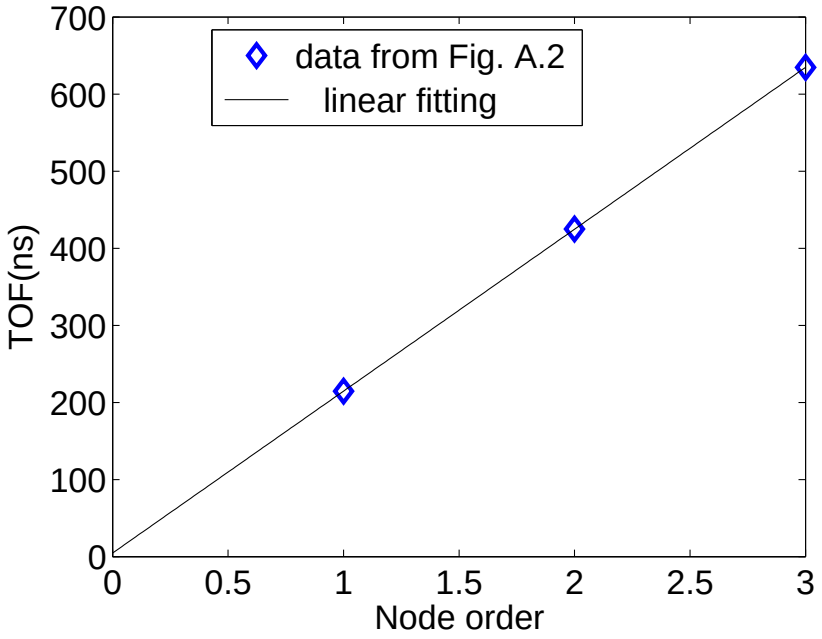

Figure A.3: Linear fit of the node TOF versus the node order taken from Fig. A.2. From the fit we determined $t_0 = 4.5$ ns. The slope of the line corresponds to the cyclotron period, $T = 210$ ns, from which the magnetic field strength B is evaluated (see text).

Appendix B

Subtraction of random coincidences in electron-ion coincidence measurement

In the coincidence measurement demonstrated in chapter 7, both the electron and the D^+ from the dissociative ionization process, $D_2 + \hbar\omega_{VUV} + N\hbar\omega_0 \rightarrow D{+}D^{+}{+}e^{-}$, are recorded. Here one VUV photon $\hbar\omega_{VUV}$ and N IR photons $\hbar\omega_0$ are absorbed. The electric field E across the COLTRIMS spectrometer is 4 V/cm and no magnetic field is applied. Under these conditions, the slow electrons of interest (≤ 0.8 eV) can be collected with 4π solid angle. The corresponding energy resolution along the TOF axis is calculated as: $\delta E = \frac{dE}{dt}\delta t = \frac{p}{m_e}\frac{dp}{dt}\delta t$, with m_e and p representing the electron mass and momentum component along z. The TDC time resolution is $\delta t = 0.5$ ns. The calibration for $\frac{dp}{dt}$ is 0.04 atomic unit/ns considering a 20 cm acceleration length for electrons. Thus a reasonable energy resolution, $\delta E = 0.148$ eV for 1 eV electron, is attained.

The experiment is conducted with a detection rate of 0.7/laser-shot on the electron detector, and 0.5/laser-shot on the ion detector. The real interaction rate can be estimated according to the MCP detection efficiency for ions. The MCP front plate of the ion detector has a potential of -2000 V, and the jet needle has a potential of about -100 V. Thus the ion gains a kinetic energy of 1900 eV before it impacts the MCP. The detection efficiency

at this energy for D_2^+ is typically $Q = 30\%$ [136]. The real interaction rate is: 0.5/Q = 1.67/laser-shot. That means that the number of D_2 molecules n interacting with each laser pulse follows a statistical distribution $f(n)$ with a peak of $n = 1.67$. For n molecules interacting with a single laser pulse, there are n^2 different combinations of e^-–D^+ pairs, among which n of them are from the same molecule. We assume that $f(n)$ is a Poisson distribution $f(n) = \frac{\lambda^n e^{-\lambda}}{n!}$ with $\lambda = 1.67$ in our case, the real coincidence fraction is thus estimated to be $\sum_{n>0} \frac{f(n)}{n} / \sum_{n>0} f(n) \approx 36\%$. If we plot the e^-–D^+ energy density map as shown in Fig. B.1(a), more than 60% of the events are contributed from false coincidences in which the electron and D^+ are coming from different molecules. Therefore, extra effort has to be made to clean up the raw data in order to get reliable coincidence plots.

We use the subtraction of random coincidences method to get rid of the false coincidences. Specifically, the kinetic energy of an electron from the mth laser shot versus the kinetic energy of a D^+ from the $(m+1)th$ laser shot is plotted, thus creating a purely false coincidence map. A second coincidence map (raw coincidence map) is created by plotting the kinetic energy of an electron and a D^+ from the same laser shot, thus including both real and false coincidences. Both maps have the same event numbers by definition. Figure B.1 shows the two different coincidence maps. There is no noticeable difference between them. The real coincidence can be obtained by subtracting the intensity distribution in Fig. B.1(b) from the intensity distribution in Fig. B.1(a). Impressively, a clear energy conservation line corresponding to the absorption of one VUV photon and three IR photons shows up after the subtraction of the random coincidences (see Fig. B.2).

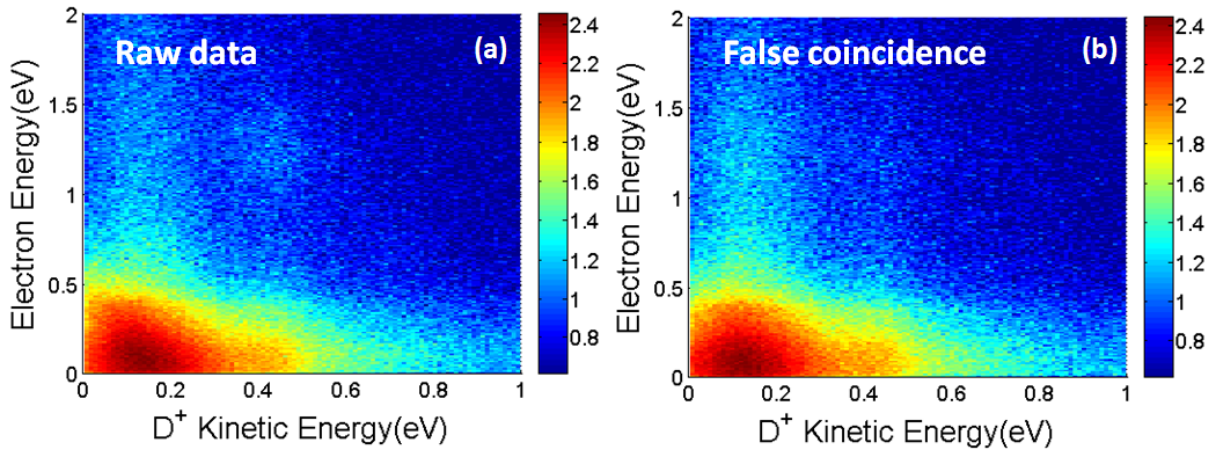

Figure B.1: Electron and D^+ energy correlation map from (a) the same laser shot, and (b) with electron generated by the mth laser shot and D^+ generated by the $(m+1)$th laser shot. Both the 9th harmonic and IR probe pulse are present to induce the dissociative ionization of D_2^+. Logarithmic scale is used.

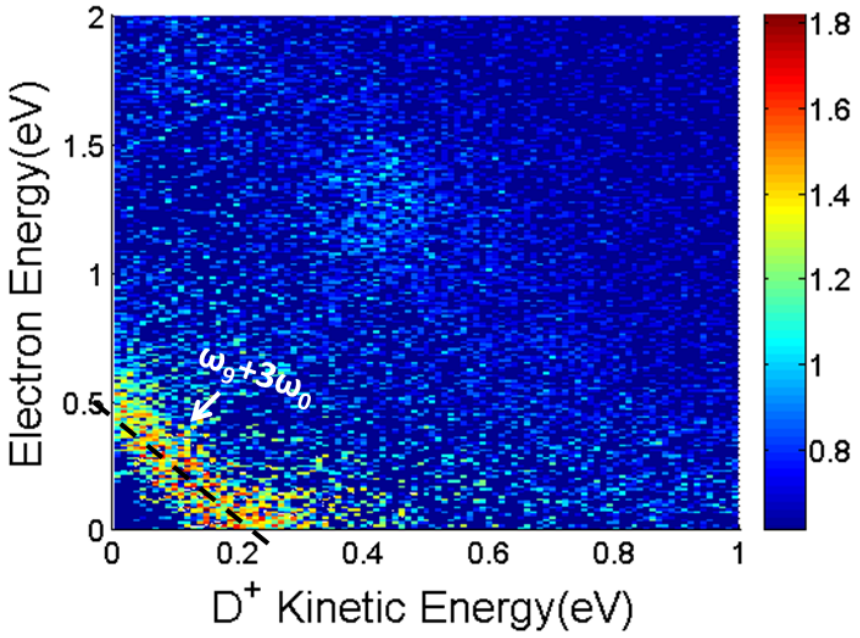

Figure B.2: Electron and D^+ energy correlation map (logarithmic scale) after subtracting the false coincidences (Fig. B.1(b)) from the raw coincidences (Fig. B.1(a)). The black dashed line indicates the energy conservation line after absorbing one 9th harmonic photon and three IR photons.

Appendix C

The grating pair configurations of the VUV monochromator

In the experimental setup described in chapter 6, the properties of the isolated harmonic (the spectral width, temporal width, efficiency) have been discussed in detail. The two major purposes of the grating-based monochromator are (a) effectively isolating a clean high harmonic and (b) maintaining a relatively high transmission efficiency. For the first purpose, sufficient line density is required to separate different harmonics spatially. For the second purpose, a larger incidence angle is preferred to increase the reflectivity of the harmonics in the VUV region.

As shown in Fig.C.1, the optical configuration of the grating pair can be defined by several parameters: the grating line density N, separation distance of the two gratings D, relative displacement of the two gratings Z and incidence angle θ. The criterion for choosing the line density of the gratings is that the separation between the two adjacent harmonics (n and $n+2$) at the slit, Δx, is no less than the beam size. Assuming a 2 mrad diverging beam from the HHG source, the beam size at the slit will be roughly 1.4 mm. The criterion for choosing the incidence angle θ is that θ is as large as possible while satisfying the first criterion. Additionally, the maximal Z value is roughly limited by the size of the chamber

that is housing the grating pair (Z < 800 mm in the current setup).

Although we used a specific grating pair arrangement in chapter 6 of the thesis for D_2 experiments, it is rather straightforward to use different combinations of grating parameters to optimize harmonics of interest for conducting different experiments. The methods to estimate the spectral/temporal width have been depicted in chapter 6. The limiting factors for temporal width are the stretching and dispersion effects. Stretching refers to the pulse duration broadening due to the tilt of the wave-front after diffraction (equation 6.2). Dispersion refers to the optical path difference for different wavelength components (equation 6.4). The spectral width of the harmonics is mainly limited by the IR spot size at the interaction region.

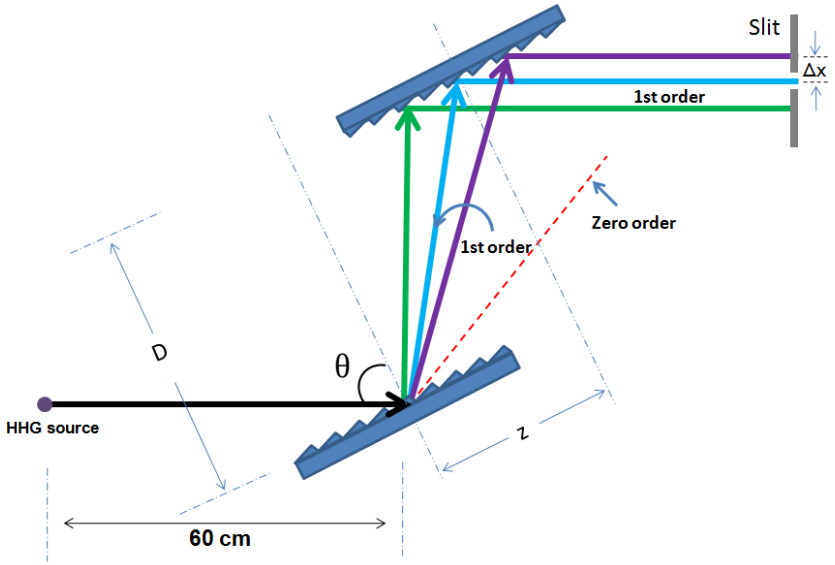

Figure C.1: Optical configuration of the grating pair

Table C.1 summarizes the harmonic properties based on a few different grating pair configurations to give guidance for future experiments. We assume that the HHG source has a divergence of 2 mrad. The effective spectral width of the harmonic pump $\Delta\omega$ is determined by the size of the IR spot. The effective temporal width τ_3 is the convolution of the stretching τ_1 and dispersion τ_2 effects. Notice that the dispersion-induced temporal broadening τ_2 is an upper limit calculated based on a 80 μm IR spot size at the interaction

H	N (lines/mm)	D(mm)	θ(degree)	$\Delta\omega$(meV)	τ_1(fs)	τ_2(fs)	τ_3(fs)
7	3600	40	60	75	123	221	253
9	3600	40	60	102	102	171	199
11	3600	40	60	131	88	139	165
13	3600	40	60	163	77	118	141
7	3600	30	60	99	92	219	237
9	3600	30	60	136	77	170	186
7	1800	40	75	112	72	213	225
9	1800	40	75	140	70	165	179
11	1800	40	75	168	63	135	149
7	1000	40	75	106	58	118	131
9	1000	40	75	134	49	92	104
11	1000	40	75	165	43	75	86

Table C.1: Properties of single harmonic for different grating pair arrangements. H: Harmonic order; $\Delta\omega$: effective spectral width limited by the IR spot size (80 μm); τ_1: stretching-induced temporal broadening; τ_2: dispersion-induced temporal broadening; τ_3: convolution of τ_1 and τ_2.

region. The actual τ_2 in an experiment can be smaller if the IR spot size participating the physical process is smaller.

From the calculated results in table C.1, lower line density gratings are preferred to achieve shorter temporal widths of the harmonics by reducing both the stretching and dispersion effects, while higher line density gratings are required to get clean single harmonics with shorter wavelengths (3600 lines/mm is needed to select the 13th harmonic for the current setup). Both the spectral width and temporal width can be significantly improved by reducing the IR spot size at the interaction region for a pump-probe experiment, this can be implemented by employing a focusing element with shorter focal length for the probe arm.

Appendix D

Spectrometer of COLTRIMS

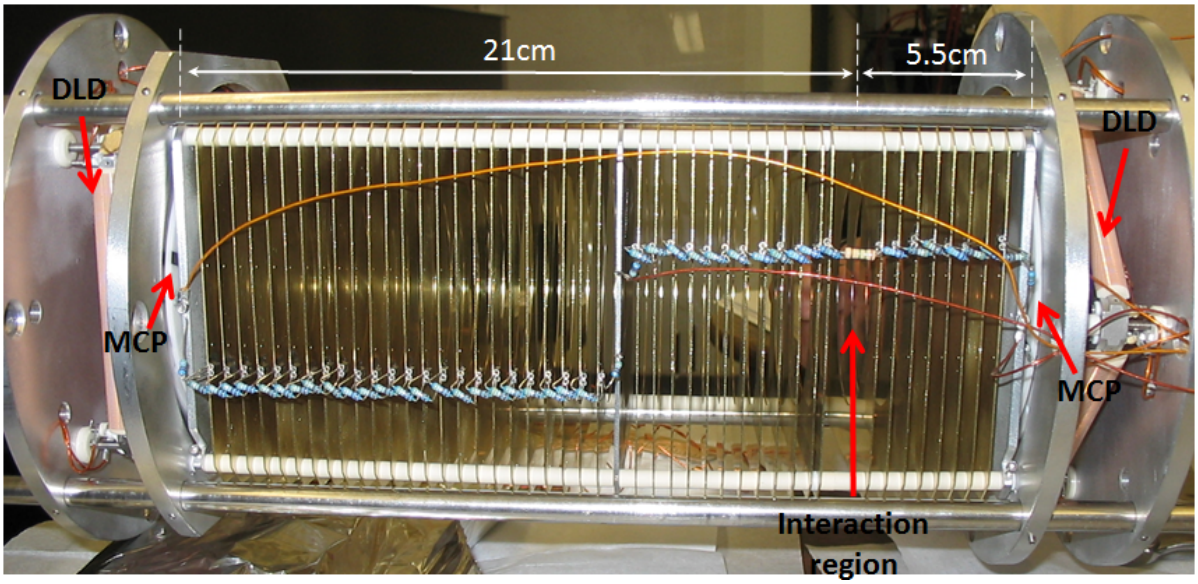

Figure D.1: Spectrometer of COLTRIMS. DLD: delay line detector. MCP: microchannel plate